Transport Spectroscopic Investigation of Anisotropic and Multiband Superconductors

Soumya Datta

A thesis submitted for the partial fulfillment of the degree of Doctor of Philosophy

Department of Physical Sciences,
Indian Institute of Science Education and Research Mohali,
Knowledge city, Sector 81, SAS Nagar, Manauli PO, Mohali
140306, Punjab, India.

January, 2023

To

My brother

who will always stay 'little' to me

My father

who always believed in me

and

My mother

whom I wish I could spend more time with

Declaration

The work presented in this dissertation has been carried out by me under the supervision of Dr. Goutam Sheet at the Indian Institute of Science Education and Research (IISER) Mohali. This work has not been submitted to any other institution or university in part or in full for a degree, a diploma, or a fellowship. Whenever contributions of others are involved, every effort is made to indicate this clearly, with due acknowledgment of collaborative research and discussions. This thesis is a *bonafide* record of original work done by me, and all sources listed within have been detailed in the bibliography.

Soumya Datta
(Candidate)

In my capacity as the supervisor of the candidate's doctoral thesis, I certify that the above statements by the candidate are true to the best of my knowledge.

Dr. Goutam Sheet
(Supervisor)

Acknowledgments

This dissertation is possible because of many people.

First of all, I would like to express my sincere gratitude to Dr. Goutam Sheet for his guidance and support. I am grateful to him that he has given me the opportunity to work with multiple experimental facilities in the lab under his supervision. Despite his commitment to accommodating funds, managing a large workforce, and looking after the facilities to keep the lab running, I appreciate that he always has managed time for me to discuss versatile topics. His knowledge within and beyond academic subjects, passion for research, and most importantly, his never giving up attitude motivated me on multiple occasions. I thank him for patiently directing me towards completing my work and encouraging me throughout.

I would like to express my gratefulness to my doctoral committee members, Dr. Sanjeev Kumar and Dr. Abhishek Chaudhari, for their helpful discussions and constant support.

I am thankful to my collaborators Dr. Yogesh Singh, Dr. Ravi Prakash Singh, Dr. Tanmoy Das, Dr. Rajeswari Roy Chowdhury, Jaskaran Singh, Kapil Motla, Anshu Kataria, Arushi, and Partha Sarathi Rana for providing good quality crystals and theoretical support for my research works.

I appreciate the financial support provided by IISER Mohali (MHRD) through JRF and SRF fellowships.

I am grateful to my fellow past and present lab mates: Leena, Aslam, Shekhar, Anshu, Sirshendu da, Ritesh, Mrityunjay, Balal, Lalit, Soumyadip, Suman, Shilpa di, Rajeswari di, Sandeep, Aastha, Aashi, Mamta, Shivam, Deepti, Monika, Ranjani, Nikhil, Nikhlesh, Mona, Samiran, Monish, Ghulam, Sudeep, and others. I am thankful to Avtar, Ranjana, and Veerpal for taking care of the timely liquid

helium supply and other necessary requirements.

I wish to thank Ranbir, Rohit, Aman, Nishat, Jasleen, Shelender, Shyam, Subhadip da, Arindam da, Tanmay, Vikram, Subhasree, Ramu, Shreyan, Rudranil, Sourav da, Sayanta, Debapriya, Manab da, Mayukh, Kala, Amartya, Esha, Soumitra, Sanjeev, and many others who made this journey memorable for me. I especially thank the members of the Confluence, the CMP discussion group, Amra Bangali group, the IISER Yoga community and the AB-1 badminton group.

Panini, Asi, Suman, Sanchari, Piyush, Sudesna, Emroj, Devanil, Nilanjan, Subhashish, Chandan, Pikesh, Rahul, Kushal, Anjan, Bappa, Priyanka, Subhajit, Iti, Pamela, Sayandeep, Roktim, Subrata, Subha, Mahua, Arnab, Pinaki, Pooja, Debapriya, Traisik, and Sourav, I thank you all for staying by my side. Dida, boro masi, boro meso, Krishna masi, Rathin kaku and mami, I will never forget your love and support. Megha, Baban, Riya, and bhagni, my affection will always be with you. I am grateful to Dr. Dipanjan Chakraborty, Dr. Ritajyoti Bandyopadhyay, Dr. Mukul Kabir, Dr. Dirthya Sanyal, Dr. Satadal Bhattacharyya, Bijan Mukherjee, Udayan Sengupta, Tapan Bain, Bhavesh Banerjee, Amalendu Halder, Dipankar da, Proloy da, Raka di, Romita di and Joy da for motivating and guiding me. What I am today is because of you all.

Without the love, support, and encouragement of my family, I would not have come this far. Baba, thank you for being an honest, resolute, and hard-working single parent. You believed in me even when I could not. Bhai, thank you for being my all-time companion. Thank you for taking care of our small library and the garden in my absence. Maa, wherever you are, I know I always have your blessing. This thesis is dedicated to the three of you.

List of publications

1. *Spectroscopic evidence of multigap superconductivity in noncentrosymmetric AuBe*
   Soumya Datta, Aastha Vasdev, Partha Sarathi Rana, Kapil Motla, Anshu Kataria, Ravi Prakash Singh, Tanmoy Das, and Goutam Sheet, *Physical Review B* **105**, 104505 (2022).

2. *Anisotropic superconductivity in ZrB_{12} near the critical Bogomolnyi point*
   Soumya Datta, Sandeep Howlader, Arushi, Ravi Prakash Singh, and Goutam Sheet, *Physical Review B* **105**, 094504 (2022).

3. *Spectroscopic evidence of mixed angular momentum symmetry in non-centrosymmetric Ru_7B_3*
   Soumya Datta, Aastha Vasdev, Ranjani Ramachandran, Soumyadip Halder, Kapil Motla, Anshu Kataria, Arushi, Rajeswari Roy Chowdhury, Ravi Prakash Singh, and Goutam Sheet, *Scientific Reports* **11**, 21030 (2021).

4. *Spectroscopic signature of two superconducting gaps and their unusual field dependence in RuB_2*
   Soumya Datta, Aastha Vasdev, Soumyadip Halder, Jaskaran Singh, Yogesh Singh, and Goutam Sheet, *Journal of Physics: Condensed Matter* **32**, 315701 (2020).

5. *Inhomogeneous superconductivity in high-density nonmagnetic cobalt in a polycrystalline Co film*
   Nasrin Banu, M. Aslam, Arpita Paul, Sanjib Banik, S. Das, **S. Datta**, A. Roy, I. Das, G. Sheet, U. V. Waghmare, S. Ramakrishnan, and B. N. Dev, *Europhysics Letters* **131**, 47001 (2020).

6. *Large enhancement of superconductivity in Zr point contacts*
   Mohammad Aslam, Chandan K. Singh, Shekhar Das, Ritesh Kumar, **Soumya Datta**, Soumyadip Halder, Sirshendu Gayen, Mukul Kabir, and Goutam Sheet, *Journal of Physics: Condensed Matter* **30**, 255002 (2018).

Abstract

This thesis will describe my studies on four superconducting materials; AuBe, RuB_2, Ru_7B_3, and ZrB_{12} where, for experimental purposes, primarily two transport spectroscopic methods were used; point-contact Andreev reflection spectroscopy (PCARS) and scanning tunneling spectroscopy (STS). We found that the superconductivity in all these four materials, in one way or another, disagrees with a conventional, isotropic, single-gap BCS description. In AuBe and RuB_2, two s-wave gaps are necessary to describe the quasiparticle excitation spectra at ultra-low temperatures. For AuBe, a simple two-gap model incorporating interband tunneling of quasiparticles seems sufficient. On the other hand, RuB_2 warrants a more advanced model with additional factors like interband scattering. In Ru_7B_3, which is a non-centrosymmetric superconducting phase, unlike RuB_2, we found that a small 'p-wave' component is necessary with the otherwise dominant 's-wave' one in the description of the superconducting order parameter. While studying superconducting ZrB_{12}, we observed two exciting features. On the basis of directional PCARS and two-coils mutual inductance measurements, it was found that the superconducting gap and its local critical field are anisotropic in this material. From the same experiments, it was also found that ZrB_{12} behaves like a type-I as well as a type-II superconductor, depending on the direction of the applied magnetic field. These observations match remarkably well with the theoretical expectations for an anisotropic superconductor near the critical Bogomolnyi point, which was proposed recently.

The overall outline of the thesis is given below, where I plan to describe the results of my four projects in four successive chapters starting from the third to the sixth.

Chapter 1: The relevant theoretical concepts related to the thesis will be discussed in this introductory chapter. This will include a brief discussion of conventional and unconventional superconductivity. Apart from that, different contexts of anisotropies in a superconductor and their possible origins, such as

unconventional pairings and multi-gap effects, will also be discussed.

Chapter 2: This chapter will briefly describe the experimental methods used in this thesis. This will primarily include two transport spectroscopic methods; point contact Andreev reflection spectroscopy (PCARS) and scanning tunneling spectroscopy (STS). The advantage of directional PCARS will also be discussed.

Chapter 3: In the third chapter, I will describe the results of our STS investigation on non-centrosymmetric superconductor AuBe. I will describe a comparison between a single-gap and a simple two-gap model for various spectra probed at different points on the sample surface. The analysis will also include the temperature and magnetic field dependence of one such typical spectrum. At the end of this chapter, I will also present the results of some theoretical calculations to support our claim.

Chapter 4: This chapter will describe the results of our detailed STS investigation on another multi-gap superconductor, RuB_2. I will highlight the indications of two gaps in this material from the previous report and I will show the spectral signature of the two gaps from our ULT STS measurements. In the end, I will highlight the shortcomings of a simple two-gap model and suggest some possible modifications in such a model to describe the data more accurately.

Chapter 5: In the fifth chapter, I will describe our STS investigation on another non-centrosymmetric superconductor Ru_7B_3, where we found the signature of a small 'p-wave' component mixed with the dominant conventional 's-wave' one in the superconducting order parameter. The appearance and disappearance of a 'zero-bias conductance peak' in the spectra with increasing temperature, a possible reason of which is the presence of higher-order symmetry in the order parameter, will also be discussed. I will relate our observations with some indications of unconventional pairing from previous reports on Ru_7B_3.

Chapter 6: I will begin this chapter with a discussion about intertype superconductivity in the context of an anisotropic superconductor. Furthermore, I will

justify why we choose ZrB_{12} as a potential material system to explore anisotropic intertype superconductivity. I will point out the contradictions in various previous reports, the limitations of previous PCARS studies in this material, and also highlight how those limitations can be overcome with a fresh direction-dependent PCARS study. Based on our detailed directional PCARS study and two-coil mutual inductance measurements, I will present proves of anisotropy and field direction-dependent type-I/type-II behavior in this system.

Chapter 7: The seventh and last chapter of my thesis will provide a conclusive summary extracted from our investigations mentioned in the last four chapters.

Contents

1 Introduction **1**

1.1 Superconductivity 1

1.2 Conventional Superconductivity 3

1.2.1 BCS Theory 5

1.2.2 Length Scales of a Superconductor 9

1.2.3 Type-I, Type-II and Intertype Superconductors 11

1.3 Unconventional Superconductivity 14

1.3.1 Possible Anisotropies 14

1.3.2 Broken Symmetries and Their Consequences 16

1.3.3 Non-centrosymmetric Superconductors 17

1.3.4 Multiband Superconductors 18

2 Experimental Methods **30**

2.1 Scanning Tunneling Spectroscopy (STS) 30

2.1.1 Working Principle of an STM 30

2.1.2 Different Modes of Operation 34

2.1.3 Our System 36

2.1.4 Preparation of STM Tip 38

2.1.5 Measurement 39

2.2 Point Contact Andreev Reflection Spectroscopy (PCARS) 40

2.2.1 Different Regimes of Electronic Transport 41

2.2.2 Superconductor-Normal Metal Interface 42

2.2.3 BTK Formalism 44

2.2.4 Directional PCARS 45

2.2.5 Our System . . . 47
2.2.6 Measurement . . . 48
2.3 Other Experimental Tools Used . . . 50

3 Multiband Superconductivity in AuBe **57**
3.1 Introduction . . . 57
3.1.1 Outstanding Issues . . . 58
3.2 Experimental Techniques . . . 59
3.3 Results and Discussions . . . 60
3.3.1 STS Spectra . . . 60
3.3.2 Analysis Under Single-gap Model . . . 62
3.3.3 Indications of Multiband Superconductivity . . . 63
3.3.4 Analysis Under Two-gap Model . . . 64
3.3.5 Comparison with MgB_2 . . . 65
3.3.6 Temperature Dependence of Spectra . . . 66
3.3.7 Magnetic Field Dependence of Spectra . . . 67
3.4 Band Structure and Fermi Surface . . . 69
3.5 Summary . . . 71

Appendices **80**
3.A Investigation with Single Anisotropic Gap . . . 80
3.B Discussion about Broadening Parameter . . . 82
3.C Magnetic Field Dependence of DOS . . . 82

4 Multiband Superconductivity in RuB_2 **87**
4.1 Introduction . . . 87
4.2 Experimental Techniques . . . 89
4.3 Results and Discussions . . . 89
4.3.1 Analysis Under Single-gap Model . . . 89
4.3.2 Indications of Multiband Superconductivity . . . 91
4.3.3 Analysis Under Two-gap Model . . . 92
4.3.4 Differences with AuBe . . . 92
4.3.5 Two-step Like Transition . . . 93
4.3.6 Unusually High Spectral $H_{c(l)}$ . . . 94

4.4 Summary 97

Appendices **103**

4.A Unconventional Features in the Spectra 103

4.B Further Modifications in the Multiband Model 104

4.B.1 Introduction of Inter-band Scattering 105

4.B.2 Introduction of a Phase-factor 107

4.C Further Discussion on High $H_{c(l)}$ 109

4.C.1 Possibility of a Mixed State 110

4.C.2 Possibility of Surface Superconductivity 112

4.C.3 Other Possibilities 112

5 Mixed Parity Superconductivity in Ru_7B_3 **119**

5.1 Introduction 119

5.2 Experimental Methods 122

5.3 Two Types of Spectra 123

5.4 Analysis Under s-wave Model 123

5.5 Discussion on Zero Bias Conductance Peak 128

5.6 Previous Indications of Unconventional Pairing 132

5.7 Introduction of p-wave Symmetry 133

5.8 Summary 137

Appendices **143**

5.A Why was the Unconventional Pairing Undetected in Previous Reports? 143

5.B Discussion about Coupling Strength 144

5.C Possibility of Proximity Induced Superconductivity 144

6 Anisotropic Superconductivity in ZrB_{12} **147**

6.1 Introduction 147

6.1.1 Anisotropy and Intertype Domain 147

6.1.2 Why is ZrB_{12} so Widely Studied? 149

6.2 Experimental Methods 151

6.3 Limitations of Previous PCARS Reports 153

6.4 Directional PCARS 153

6.4.1 Anisotropy in Gap . . . 154
6.4.2 Temperature Dependence of Spectra . . . 156
6.4.3 Anisotropy in Critical Field . . . 157
6.4.4 Anomalous Field Dependence of Barrier Potential . . . 158
6.4.5 Vortex Core Model . . . 159
6.5 AC Magnetic Susceptibility Measurements . . . 161
6.5.1 Type-I vs Type-II . . . 162
6.5.2 Further Confirmation of Magnetic anisotropy . . . 164
6.6 Summary . . . 165

Appendices **174**
6.A Possibility of Multiband Superconductivity . . . 174
6.B Discussion about Coupling Strength . . . 175
6.C Discussion about Critical Field . . . 176
6.D Absence of a type-I Like Transition in PCARS . . . 176
6.E Further Discussion on Anisotropy . . . 177

7 Conclusion **184**

Chapter 1

Introduction

All four projects described in this thesis (Chapter 3 to Chapter 6) are related to superconductivity and its different aspects. In this chapter, I will present an overview of this phenomenon, particularly highlighting the subtopics which will be relevant to the experimental investigations described later.

1.1 Superconductivity

A material is called a superconductor if it demonstrates the following two properties simultaneously.

- Zero electrical resistivity like an ideal conductor.
- Expulsion of magnetic flux like an ideal diamagnet.

There are certainly other unique properties that a superconductor does show, but the two referred to above are necessary and sufficient. If a material shows superconductivity, it does so within the following three windows of external parameters.

- The temperature of the material being less than a critical value (T_c).
- The external magnetic field, if applied, being less than a critical value (H_c).
- Any current passing through the material being less than a critical value (I_c).

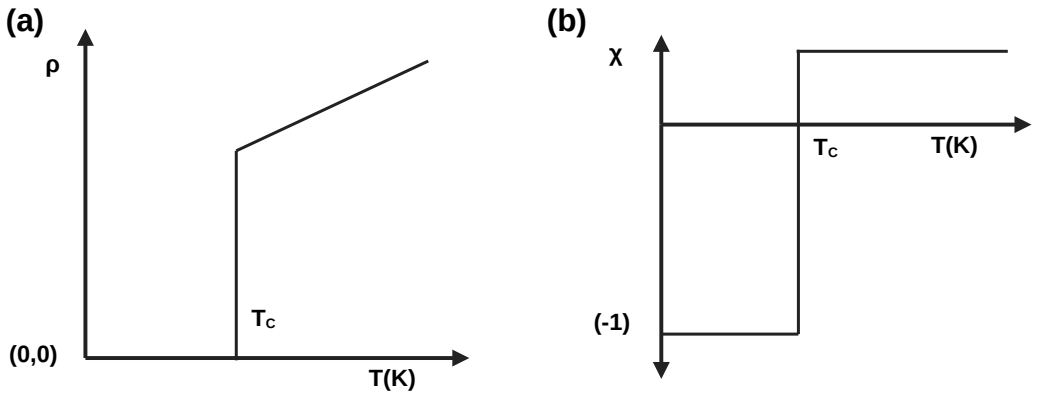

Figure 1.1: The schematic representations of two fundamental properties of a superconductor, **(a)** 'zero' electrical resistivity (ρ) and **(b)** 'negative' magnetic susceptibility (χ) below transition temperature T_c.

The first property of vanishing resistivity (and also the phenomenon of superconductivity as a whole) was discovered in elemental Mercury (Hg) by Heike Kamerlingh Onnes [1] in 1911. He observed a sudden drop in the resistivity to 'zero' at 4.2 K for Hg and initially thought about some experimental error (like contact short circuit). However, reproducibility of the observation from repeated careful experiments convinced him of this milestone discovery, and for that, he was awarded the Nobel Prize in Physics two years after. Subsequently, the vanishing resistivity was discovered in a number of elemental metals (like Tin (Sn) [2] and Lead (Pb) [3]) and alloys (like Niobium-Titanium (Nb-Ti) [4]).

Initially, the term 'superconductivity' was used to refer only to the zero electrical resistivity property of a material. The second property, i.e. the expulsion of magnetic flux, was discovered by Walther Meissner and Robert Ochsenfeld [5] in 1933. It was found that when a material undergoes the superconducting transition ($T < T_c$) in the presence of a weak magnetic field ($H < H_c$), it produces a surface current, which expels all magnetic flux from the inside of the superconductor. This phenomenon, which later became famous as the Meissner effect, seemed to be a unique property of a superconductor which cannot be described by considering a perfect conductor with zero resistivity. The zero electrical resistivity of a

superconductor supports the necessary dissipation-less surface current, and thus the two definitive properties of superconductivity are not independent, rather are interconnected [6].

After these two discoveries, theorists tried to come up with a microscopic theory of superconductivity. The London theory [7] (developed by the two brothers Fritz and Heinz London) in 1935 and the Ginzburg-Landau theory [8] (developed by Vitaly Ginzburg and Lev Landau) in 1950 were two important breakthroughs in that direction. However, it took almost half a decade counting from Onnes' experimental discovery [1], when a complete, self-consistent, microscopic theory of superconductivity (the famous BCS theory) was proposed by John Bardeen, Leon Cooper, and John Robert Schrieffer [9] in 1957. The scientists trio received the Nobel Prize in Physics for this theory in 1972.

1.2 Conventional Superconductivity

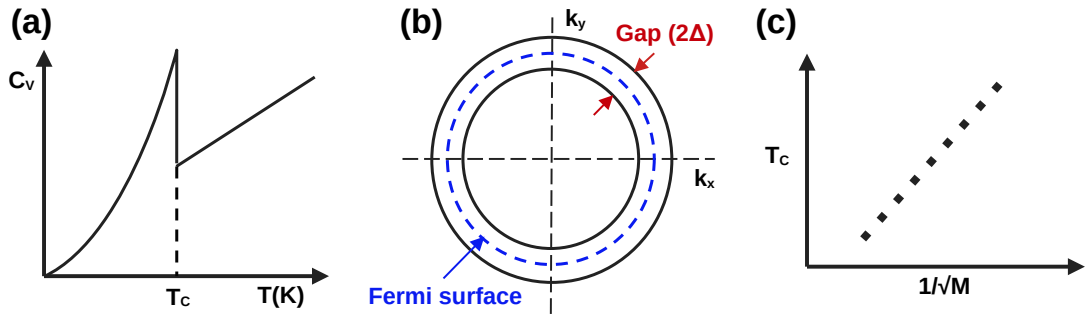

Figure 1.2: The schematic representations of **(a)** the exponential rise in the heat capacity at low temperature below T_c, **(b)** an energy gap (Δ) at the Fermi surface, and **(c)** the isotope effect for a superconductor.

The following experimental findings constructed the background of BCS theory [10].

- The exponential increase in heat capacity at low temperature [11, 12] (as represented in Fig. 1.2(a)), the existence of a critical temperature, and the

existence of a critical magnetic field, all these indicated towards the formation of a 'pairing'. The obvious outcome of such a pairing is a band gap at the Fermi surface (as represented in Fig. 1.2(b)) that was later confirmed by infrared/microwave absorption experiments [13, 14].

- For a mono-atomic lattice, the Debye frequency of phonons is proportional to the inverse square root of the lattice ion mass. Experimentally, it was found [15, 16] that the T_c of a mono-atomic superconducting material also varies as the inverse square root of the lattice ion mass (as represented in Fig. 1.2(c)). This phenomenon, which is called the isotope effect, suggests that the lattice interaction or phonon is involved in superconductivity. For superconductors with more complicated chemical composition, the T_c generally decreases with increasing atomic mass but the isotope effect may have a different form [17].

The key principle behind the BCS theory is the following [10]. Somehow the electrons pair up, and those pairs, which are called 'Cooper pairs', condense into a single coherent ground state. This allows the electrons to traverse through the crystal cooperatively, conserving their momentum. Now the question is, 'What provides the glue for such pairing?' According to BCS theory, the Fermi surface is unstable to infinitesimal attractive forces [18], and phonon coupling offers such an attractive force (glue) [19]. When one electron interacts with the lattice, the other takes advantage of this and adjusts itself to reduce the energy of the system. This causes a correlation between the two electrons and a weak attractive force between them. The pairing process increases the kinetic energy but decreases the potential energy by a greater magnitude. As a result, the pairing state (bosonic) with overall reduced energy compared to the individual electronic state (fermionic) becomes more favorable. The paired electrons, whenever they go through any scattering, scatter together, keeping their momentum equal and opposite. As the momentum remains conserved, the resulting current flow remains dissipationless. Therefore, according to BCS theory, the electron-phonon interaction is the main cause of superconductivity, and the superconductors which follow BCS theory are called 'conventional superconductors'.

1.2.1 BCS Theory

The total Hamiltonian of a superconducting system can be written as follows, where the electron-phonon interaction is represented by a second-order correction with negative energy [20, 21].

$$H = H_{el} + H_{ph} + H_{el-ph} \tag{1.1}$$

Here, the last interaction term can be represented as follows.

$$H_{el-ph} = \sum_{k,q} M_q c^{\dagger}_{k+q} c_k \left(b_q + b^{\dagger}_{-q} \right) \tag{1.2}$$

where M_q is the electron-phonon coupling coefficient, $c^{\dagger}_i$ and c_i are, respectively, the creation and annihilation operators of the electron with momentum i, $b^{\dagger}_i$ and b_i are, respectively, the creation and annihilation operators of the phonon with momentum i. After the second-order correction from perturbation theory, the above Hamiltonian can be rewritten as follows.

$$H_{eff} = H_0 + \sum_{k,q} c^{\dagger}_{k+q} c^{\dagger}_{k'-q} c_{k\prime} c_k V(k', q) \tag{1.3}$$

where the potential energy $V(k', q)$ can be represented by the following equation with phonon-frequency represented by ω_q for a phonon with momentum q and the electronic energy represented by ε_i for an electron with momentum i.

$$V(k', q) = \frac{|M_q|^2 \hbar\omega_q}{\left(\varepsilon_{k'} - \varepsilon_{k'-q}\right)^2 - \left(\hbar\omega_q\right)^2}. \tag{1.4}$$

Now, for the electron-phonon interaction to be attractive, $V(k', q)$ has to be negative. The only way this can be possible is if the following condition is satisfied.

$$\left(\varepsilon_{k'} - \varepsilon_{k'-q}\right) < \left(\hbar\omega_q\right) \tag{1.5}$$

In general, the electronic energy ε_i is $\sim$ eV, while the phononic energy $\hbar\omega_q \sim$ meV. So, to maintain the above inequality, first of all, the electronic energy before and after the phonon absorption or emission ($\varepsilon_{k'}$ and $\varepsilon_{k'-q}$) cannot be energetically separated much. This explains why the superconducting gap is $\sim$ meV. On the

second note, $V(k', q)$ is proportional to the phonon-frequency ω_q, while ω_q is proportional to phonon-momentum q, and q is nothing but the momentum difference between the two electrons (i.e., $q = k - k'$). So, for the attraction to be strongest (i.e., the magnitude of $V(k', q)$ to maximum), q needs to be maximum also. For a particular value of k, the maximum value of q is $2k$ when $k' = -k$. This explains why two electrons with exactly opposite momentum are most favorable to form the Cooper pair and ultimately condense into the minimum energy state. According to BCS theory, the ground-state wave function of such Cooper pairs is represented as follows.

$$|\Psi_{BCS}\rangle = \prod_k \left(u_k + v_k c^\dagger_{k\uparrow} c^\dagger_{-k\downarrow}\right)|0\rangle \tag{1.6}$$

where u_k^2 and v_k^2 are, respectively, the probabilities of the occupancy and vacancy of the Cooper pair and $|0\rangle$ is the vacuum state. The energy required to break the pair, which is equivalent to the binding energy of a Cooper-pair, is known as the superconducting energy gap (because it manifests a gap in the density of states at the Fermi surface). The momentum dependence of the energy gap (at temperature $T = 0$) can be expressed as:

$$\Delta_k = -\frac{1}{N}\sum_{k'} V_{kk'}\langle c^\dagger_{k\uparrow} c^\dagger_{-k\downarrow}\rangle \tag{1.7}$$

where $V_{kk'}$ is the attractive electron-electron interaction energy. The BCS theory assumed that the electron-electron interaction is constant within a shell of width $\hbar\omega_D$ (ω_D is the Debye frequency) around the Fermi level and beyond that it is 'zero', i.e,

$$V_{kk'} = \begin{cases} -V & |\varepsilon_{k'}|\,,\ |\varepsilon_k| \leq \hbar\omega_D \\ 0 & \text{otherwise} \end{cases} \tag{1.8}$$

This means that the electron-phonon interaction and as a consequence the gap Δ is isotropic in the momentum-space under BCS theory. Such a symmetry is called s-wave symmetry, and the superconductors which follow the BCS theory, i.e., the conventional superconductors, are characterized by $L = 0$ and $S = 0$, and often called 's-wave superconductors'.

So far, the creation and annihilation operators ($c_i^\dagger$ and c_i) that we have used are for electrons (or holes). However, as Nikolay Bogolyubov [22] had shown in 1958, the elementary excitations in a superconductor are neither purely an electron nor a hole like in a normal metal. Such quasiparticles are called Bogoliubons, and their creation and annihilation operators are defined as follows [22, 23].

$$\begin{aligned} \gamma_{-k\downarrow}^\dagger &= u_k^* c_{-k\downarrow}^\dagger + v_k^* c_{k\uparrow} \\ \gamma_{k\uparrow} &= u_k c_{k\uparrow} - v_k c_{-k\downarrow}^\dagger \end{aligned} \tag{1.9}$$

where $\gamma_{-k\downarrow}^\dagger$ creates an electron with momentum $-k$, spin $\downarrow$ and destroys one with momentum k, spin $\uparrow$, while $\gamma_{k\uparrow}$ destroys an electron with momentum k, spin $\uparrow$ and creates one with momentum $-k$, spin $\downarrow$. It is important to note that these excitations still follow the Fermi-Dirac distribution like the electronic ones ($c_i^\dagger$ and c_i). If Bogoliubons have an energy dispersion E_k, we can write the following expression.

$$\langle \gamma_{k'\uparrow}^\dagger \gamma_{k'\uparrow} \rangle = \langle \gamma_{-k'\downarrow}^\dagger \gamma_{-k'\downarrow} \rangle = \frac{1}{exp\left(\frac{E_{k'}}{k_B T}\right) + 1} \tag{1.10}$$

In position-space representation, the electron-like and hole-like quasiparticle wave functions can be represented as the following.

$$\psi_e = \begin{bmatrix} u \\ v \end{bmatrix} e^{iqx}, \ \psi_h = \begin{bmatrix} v \\ u \end{bmatrix} e^{-iqx} \tag{1.11}$$

The probabilities of occupancy and vacancy (u_k and v_k) can be represented in terms of the excitation energy of the quasiparticle (ε_k) and the superconducting energy gap (Δ) as follows.

$$
\begin{aligned}
|u_k|^2 &= \frac{1}{2}\left[1 + \frac{\varepsilon_k}{\sqrt{\varepsilon_k^2 + |\Delta_k|^2}}\right] \\
|v_k|^2 &= \frac{1}{2}\left[1 - \frac{\varepsilon_k}{\sqrt{\varepsilon_k^2 + |\Delta_k|^2}}\right]
\end{aligned}
\tag{1.12}
$$

Now, using the Fermi-Dirac statistics from Eqn. 1.10 and the above expressions for u_k and v_k from Eqn. 1.12 in the Bogoliubons transformation equations in Eqn. 1.9, the general expression for the superconducting energy gap Δ_k from Eqn. 1.7 can be rewritten as:

$$
\Delta_k = -\frac{1}{N}\sum_{k'} \frac{V_{kk'}\Delta_{k'}}{2E_{k'}} \tanh\left(\frac{E_{k'}}{2k_BT}\right) \tag{1.13}
$$

There is no way to proceed further without using a particular form of the potential $V_{kk'}$. If we use the BCS approximation of isotropic gap (Eqn. 1.8), we can have a numerical solution of Eqn. 1.13 and that will provide two important results in two limiting conditions [24]. First, at $T \to 0$ the superconducting gap becomes:

$$
\Delta_0 = 2\hbar\omega_D \mathrm{e}^{-\frac{1}{VN(0)}} \tag{1.14}
$$

where $N(0)$ is the electronic density of states at the Fermi level, $\hbar\omega_D >> \Delta_0$, and under the weak coupling approximation, $VN(0) << 1$. Second, the definition of T_c ($\Delta(T \to T_c) = 0$) yields:

$$
T_c = \frac{2\mathrm{e}^{\gamma_E}}{\pi}\frac{\hbar\omega_D}{k_B}\mathrm{e}^{-\frac{1}{VN(0)}} \tag{1.15}
$$

where $\gamma_E \approx 0.577$ is the Euler constant and $\hbar\omega_D >> k_BT_c$. Eqn. 1.14 shows that an arbitrarily small attractive interaction V yields a finite gap Δ_0 at zero temperature. Eqn. 1.15 says the same thing about the transition temperature T_c. This confirms the statement that the Fermi surface is unstable towards the formation of a BCS superconducting state. Eqs. 1.14 and 1.15 can be further

combined to give the following universal ratio:

$$\frac{\Delta_0}{k_B T_c} = 1.76 \tag{1.16}$$

This value of 1.76 is called the BCS limit for conventional superconductors, and that happens to be approximately correct for most conventional superconductors [6], including almost all known superconductors at the time the BCS theory [9] was proposed. For a weak-coupling superconductor, the ratio generally remains within a range between 1.5 to 2.25 [21]. Most low-temperature superconductors such as elemental metals and their alloys fall into this category and generally obey BCS theory. On the other hand, for a strong-coupling superconductor, the ratio can be completely arbitrary. Most of the high-temperature superconductors, such as cuprates and iron pnictides, fall in this category. For the latter group, BCS theory alone cannot completely explain the superconducting properties in those materials, and they are called 'unconventional superconductors'. More details about them will be discussed in the upcoming Section 1.3. Within Chapter 3 to 6 of this thesis, the ratio $\Delta_0/k_B T_c$ based on our experimental data will be frequently discussed to characterize the superconductors under study. The ratio will also be used to distinguish the contributions of the individual gaps in context of multiband superconductivity, wherever applicable.

1.2.2 Length Scales of a Superconductor

At the beginning of this chapter, I mentioned two theories, the London theory [7] and the Ginzburg-Landau theory [8], which were predecessors to the BCS theory [9]. Here, we will discuss two important contributions, one from each one of them [21]. The primary motivation behind the London theory (1935) was to explain the Meissner effect (1933) [5]. For that purpose, London brothers introduced two basic equations for the superconducting current density $\mathbf{J}$ in terms of measurable fields $\mathbf{E}$ and $\mathbf{B}$ [7]:

$$\frac{\partial \mathbf{J}}{\partial t} = \frac{n_s e^2}{m}\mathbf{E} \tag{1.17}$$

$$\nabla \times \mathbf{J} = -\frac{n_s e^2}{m}\mathbf{B} \tag{1.18}$$

where n_s is the number density of superconducting electrons. Combining Eqn. 1.18 with the Maxwell equation $\nabla \times \mathbf{B} = \mu_0 \mathbf{J}$, we get:

$$\nabla^2 \mathbf{B} = \frac{1}{\lambda^2}\mathbf{B} \tag{1.19}$$

Eqn. 1.19 directly explains the Meissner effect [5] saying that the magnetic field $\mathbf{B}$ decays exponentially inside a superconductor with a characteristic length scale λ expressed as:

$$\lambda = \sqrt{\frac{mc^2}{4\pi n_s e^2}} \tag{1.20}$$

This λ, which is called *'the London penetration depth'* of a superconductor is our *first characteristic length scale*. λ can be compared with the 'skin depth' δ of a metal in electrodynamics. Later, experimentally, two important properties were revealed about λ. First, it increases with temperature according to the following empirical model.

$$\lambda(T) = \frac{\lambda(0)}{\sqrt{1-(T/T_c)^4}} \tag{1.21}$$

Second, the zero T extrapolated $\lambda(0)$ from the experimental measurements is always larger than the theoretically calculated one, as mentioned in Eqn. 1.20. To resolve the issue, Alfred Brian Pippard [25] proposed an alternative length scale from a new perspective. He argued that not all the electrons but only those within the $\pm k_B T_c$ energy range around the Fermi level play a significant role in superconductivity. From the uncertainty principle argument, those electrons will then have a momentum range $\Delta p \approx k_B T_c / v_F$, which in turn provides a length scale of $\Delta x \geq \hbar/\Delta p \approx \hbar v_F / k_B T_c$. Based on this nonlocal generalization, Pippard proposed his new characteristic length scale for a superconductor introducing a numerical constant a in the expression:

$$\xi = \frac{a\hbar v_F}{k_B T_c} \tag{1.22}$$

This ξ, which is called *'the Pippard's coherence length'* of a superconductor is our *second characteristic length scale*. ξ can be compared to the mean free path l of a metal in electrodynamics. Later, in 1950, Vitaly Ginzburg and Lev Landau [8] introduced a similar characteristic length scale in their famous 'Ginzburg-Landau theory' considering superconducting electrons rather than the normal excitations.

$$\xi(T) = \sqrt{\frac{\hbar^2}{4m\alpha_0|T - T_c|}} \tag{1.23}$$

This $\xi(T)$ is called *'the GL coherence length'* of a superconductor, where α_0 is a constant parameter. At $T << T_c$, GL coherence length ($\xi(T)$) $\approx$ Pippard's coherence lengt (ξ). Similarly, in Ginzburg-Landau theory [8], the penetration depth can also be rewritten as:

$$\lambda(T) = \sqrt{\frac{m\beta}{4\mu_0 e^2 \alpha_0|T - T_c|}} \tag{1.24}$$

This $\lambda(T)$ is called *'the GL penetration depth'* where β is another parameter. As both $\xi(T)$ and $\lambda(T)$ have equivalent dependences on T, a dimensionless temperature-independent parameter κ is defined as following.

$$\kappa = \frac{\lambda}{\xi} \tag{1.25}$$

This κ is called *'the GL parameter'* and it is frequently used to distinguish superconductors in two categories; type-I and type-II. This parameter κ will be particularly relevant for the discussions in Chapter 3 and especially Chapter 6 of this thesis.

1.2.3 Type-I, Type-II and Intertype Superconductors

For most of the low-temperature superconductors discovered earlier, particularly elemental metals such as Hg, Pb, Al, etc., it was found that $\xi(T) > \lambda(T)$. In such a material, when a weak magnetic field is applied (below T_c) the material shows the Meissner effect [5]. When the strength of the applied field is increased, the moment it crosses a critical value H_c, the superconductivity gets abruptly destroyed

through a first-order phase transition.

In 1957, Alexei Alexeyevich Abrikosov [26] proposed a different superconducting phase for materials that can have $\xi(T) < \lambda(T)$. Abrikosov's idea was based on the concept of quantum vortices in superfluids developed earlier by Lars Onsager [27] in 1949 and modified further by Richard Feynman [28] in 1955. In such a material, the magnetic flux can penetrate through the superconductor in a periodic array of flux tubes, while each flux tube carries a single quantum of flux $\Phi_0 = hc/2e$. The formation of such vortices occurs when the applied magnetic field crosses a critical value H_{c1} but is less than a second critical value H_{c2}. Below H_{c1} the material shows the Meissner effect and above H_{c2} the material completely loses its superconductivity. Only a hand full of elemental metals like Nb, V and most of the metal alloys such as Nb-Sn and Nb-Ti fall into this category. Most of the high-temperature superconductors, such as cuprates and iron pnictides, also fall into this category. Abrikosov [26] calculated the exact boundary between the two phases at $\kappa = 1/\sqrt{2}$ and, based on that, described the two types of superconductors [6] as type-I ($\kappa < 1/\sqrt{2}$) and type-II ($\kappa > 1/\sqrt{2}$). In Fig. 1.3, the comparisons between a type-I and a type-II superconductor are shown in terms of the response to the magnetic field and the $H - T$ phase diagram.

However, if a superconductor has $\kappa \approx 1/\sqrt{2}$ [29–34], this categorization does not work. Also, Abrikosov's classification [26] is based on the Ginzburg-Landau formalism [8], which, on the other hand, is strictly valid near the critical temperature T_c. As a result, only around T_c superconductors can be classified as type-I or type-II. In the hypothetical phase space (κ, T), this critical point $(1/\sqrt{2}, T_c)$ is known as the Bogomolnyi point (B-point) [35, 36]. The vortex-vortex interaction is attractive in type-I superconductors but repellent in type-II superconductors. The interaction between the vortices, however, vanishes precisely at the B-point, and an infinite degeneracy of arbitrary flux configurations exists [35, 36]. When $T < T_c$, the B-point spreads over a finite range of κ values [37–40], and the usual description of type-I and type-II by Abrikosov fails [32–34].

Inter-type (IT) superconductors are the superconductors that fall within this

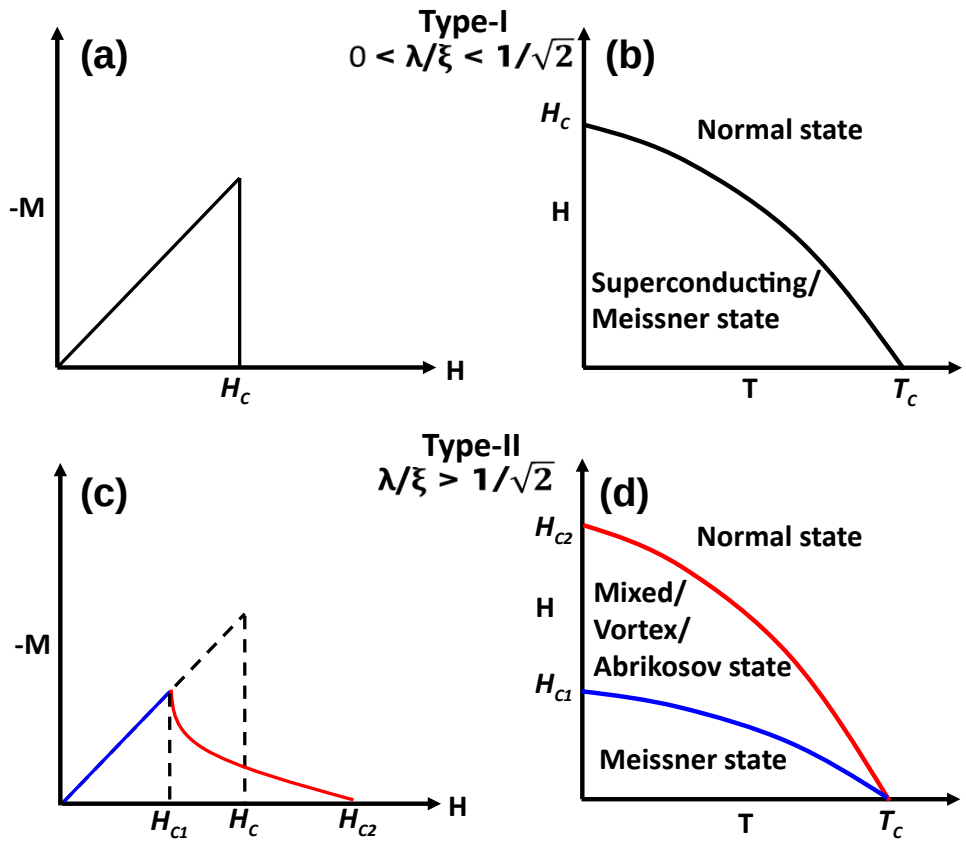

Figure 1.3: The comparisons between a type-I and a type-II superconductor. **(a)** magnetization (M) vs. magnetic field (H) plot and **(b)** the $H-T$ phase diagram for a typical type-I superconductor. **(c)** and **(d)** The same for a typical type-II superconductor.

category. The vortex-vortex interaction becomes non-monotonic at this point. As a result, both attractive long-range interactions and repulsive short-range interactions are feasible at the same time. As the range of κ within which the B-point spreads is temperature-dependent in such systems, a temperature-dependent transition from the conventional type-I to type-II superconducting phase can be observed here. For example, elemental Vanadium (V) behaves like a type-I superconductor with $\kappa = 0.82$ near its transition temperature (5.4 K) but becomes a type-II with κ as high as 1.5 at 0 K (extrapolated) [41]. Similarly, diluted alloy $Pb_{0.99}Ti_{0.01}$ has $\kappa = 0.58$ near its transition temperature (7.2 K), but that

κ increases to 0.71 (boundary value) when the material is cooled to 4.3 K. As a result, $Pb_{0.99}Ti_{0.01}$ behaves like a type-I superconductor above 4.3 K and a type-II superconductor below that crossover temperature [41]. In the third chapter of this thesis, I will discuss another such intertype superconductor, AuBe, which has a reported crossover temperature of 1.2 K [42]. Apart from temperature, since the B-point is infinitely degenerate, the superconductor becomes sensitive to other internal and external parameters such as system geometry, impurities, applied current, and external magnetic field [43–50]. In summary, just by changing these parameters a little, the superconductor can be brought from the type-I phase to the type-II phase and vice versa. In the sixth chapter of this thesis, I will discuss one such transition where we, in an anisotropic superconductor (ZrB_{12}), experimentally report the change in its type (I to II and vice-versa) just by changing the direction of the applied magnetic field.

1.3 Unconventional Superconductivity

According to the BCS theory [9], the pairing potential ($V_{kk'}$ in Eqn. 1.8) originates from the electron-phonon interaction. As phonon scattering is isotropic in the momentum space, the superconducting energy gap Δ also remains isotropic in the momentum space. All conventional superconductors, be it type-I or type-II, show this property and, as mentioned before, they are also termed as 's-wave (L=0) superconductors' [6]. However, for superconductivity, the electron-phonon interaction is not essential; just an attractive potential is. In the next section, I will briefly describe the scenarios where the attractive potential may arise from other interactions apart from the electron-phonon one.

1.3.1 Possible Anisotropies

For some superconductors, the weak attractive potential can originate from interactions other than the electron-phonon one [51]. For example, it was long believed that for superconducting Sr_2RuO_4, the pairing potential originates from ferromagnetic fluctuation. As a result, the superconducting order parameter in such materials have p-wave (L=1) symmetry [52, 53] and the orbital wave function of

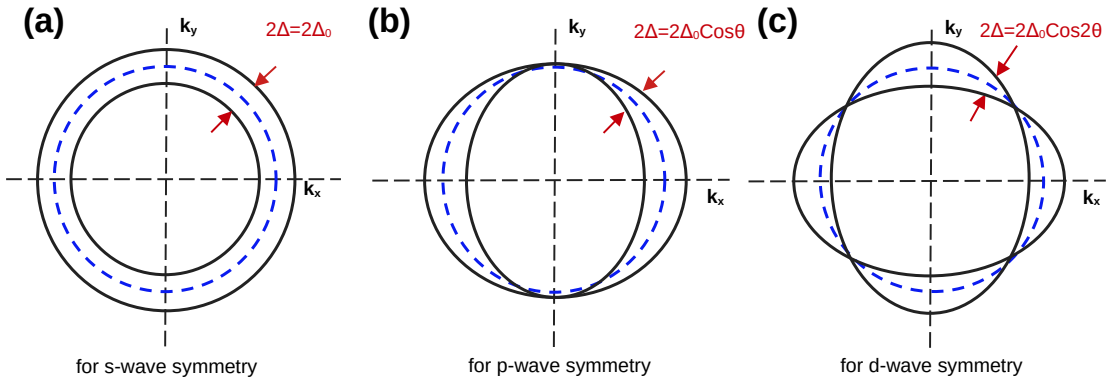

Figure 1.4: The two-dimensional schematic representations of different symmetries in superconducting gap Δ, **(a)** for s-wave symmetry, **(b)** for p-wave symmetry, and **(c)** for d-wave symmetry. The overall gap has a three-dimensional shape in the momentum space unless the superconductor itself is two-dimensional.

the Cooper pair is anti-symmetric upon the exchange of the participating electrons' positions. In Chapter 5 of this thesis, I will discuss about superconducting Ru_7B_3, where multiple experiments reported by independent groups have indicated the signatures of a p-wave component in the gap which we directly probed through our scanning tunneling spectroscopic investigation. On the other hand, for high T_c cuprate superconductors (such as LaBaCuO and $YBa_2Cu_3O_{7-\delta}$), the pairing potential originates from antiferromagnetic fluctuation. As a result, the superconducting order parameter in such materials has d-wave (L=2) symmetry [54, 55]. It was also argued recently that without any strain inhomogeneity, which can occur near edge dislocations of the crystal, the pure Sr_2RuO_4 might be a d-wave superconductor [56]. In Fig. 1.4, three different symmetries in the superconducting gap Δ are presented in two-dimensional momentum space representations. It is important to note that the overall Δ has a three-dimensional shape in the momentum space unless the superconductor itself is a two-dimensional one. Although the symmetry of the gap can be experimentally verified, the origins of pairing in such superconductors are not that easy to determine. Abrikosov and Gor'kov [57] showed that the ferromagnetic order and the superconducting order are antagonistic to each other. Hence, magnetic fluctuations, as the origin of pairing in

these materials, are indeed debatable. There are also experimental evidences that conventional electron-phonon coupling can cause superconductivity in such a material [58].

The description of pairing can be even more complicated. Like in superconducting MgB_2, it was found that the measured superconducting gap is different from different momentum directions [59–63]. However, it was also seen (at least no sufficient proof was found to believe otherwise) that the superconductivity in this material originates from the electron-phonon interaction, as in a conventional, s-wave BCS superconductor. Two different theoretical models were proposed to explain this behavior. According to the first model [64], such anisotropy is explained by a multi-gap effect where more than one electronic band (with different values of the electron-phonon coupling strength) participates in superconductivity. In two superconducting materials AuBe and RuB_2 we have studied (more details about them are given in Chapter 3 and Chapter 4 of this thesis, respectively), this multiband superconductivity model will be relevant, and I will describe this more elaborately in the next Section 1.3.4 of this chapter. According to the second model [65], there is a single gap originating from a single electronic band, but the gap changes its magnitudes with changing momentum direction without changing its phase. The superconductivity based on the last model is called an anisotropic s-wave one. For comparison, in the p and d-wave superconductors mentioned before, the gap changes both magnitude and phase with changing momentum direction.

1.3.2 Broken Symmetries and Their Consequences

Apart from the gauge symmetry, which is spontaneously broken in a superconductor, two other symmetries that play key roles in its behaviors are the inversion symmetry and the time-reversal symmetry. If both of these symmetries are protected, according to the Pauli exclusion principle, the complete set of possible Cooper pairs can be distinguished into either the even-parity states (corresponding to the spin-singlet configuration) or the odd-parity states (corresponding to the spin-triplet configuration) [66]. If any of these two are broken, the Cooper pair's conventional BCS description may not remain valid. If the time-reversal symmetry

is broken, it affects the spin-singlet pairing. If the inversion symmetry is broken, it affects the spin-triplet pairing. Now, from the experimental perspective, it is easy to break the time-reversal symmetry by applying a magnetic field. However, it is not that straightforward to break the inversion symmetry in a system by applying an electric field because, unlike magnetic field, the electric field gets strongly screened in a metal [67]. For that purpose, a promising alternative method can be to look for a superconductor where the inversion symmetry is already broken in its crystal structure.

1.3.3 Non-centrosymmetric Superconductors

If the crystal structure of a superconductor lacks a center of inversion, the antisymmetric spin-orbit coupling (ASOC) can remove the spin degeneracy in the Fermi surface. As a result, orbital angular momentum $\hat{J}$ and spin angular momentum $\hat{S}$ do not remain good quantum numbers, and the parity of the superconductor does not remain conserved too. In such a situation, Pauli's exclusion principle cannot restrict the symmetry of the Cooper pair to be between either the pure even-parity singlet or the odd-parity triplet, and a mixed state becomes possible [68]. Due to this allowed mixing, non-centrosymmetric superconductors (NCS) can exhibit peculiar behavior compared to a conventional one, *e.g.* high Pauli limiting fields [69], helical vortex states [70] and even topologically symmetry protected states [71] if ASOC is high enough. For this reason, with the discovery of the first NCS $CePt_3Si$ [69], this field has gained good attention from scientists [67, 72].

However, in spite of several auspicious theoretical predictions, little experimental progress has been reported so far because of multiple issues associated with such systems. The first obvious reason is the scarcity of high-quality single crystals. In addition, the mere presence of ASOC, as described above, is not a sufficient condition. The coupling, which is determined by the crystallographic structure, must be strong enough to make the effect detectable by any real-life experimental technique, provided that the singlet-triplet mixing is allowed by the pairing mechanism in the first place. To give an explicit example, though Li_2Pt_3B was found to have a

clear spin-triplet order parameter consistent with the line nodes, Li_2Pd_3B, on the other hand, was reported to have predominantly a spin-singlet component from penetration depth [73], nuclear magnetic resonance [74] and specific heat measurements [75]. Another possible cause is the strong electronic correlation, which, in some materials, complicates the detection of the ASOC effect. The heavy fermionic characteristics of $CePt_3Si$ is one of such examples [69]. In such materials, both superconductivity and magnetic order can coexist near the magnetic quantum critical point [76–78]. Transition-metal compounds like T_2Ga_9 (T = Rh or Ir) [79], Li_2T_3B (T = Pd or Pt) [80] as just mentioned *etc.* rather are comparatively better candidates for study, as they lack such complexities. However, it is challenging to synthesize pure single crystals of such materials because of the difference in the vapor pressure between the constituent elements. In this context, boride materials became important for studying unconventional superconducting properties because of their non-heavy fermionic yet non-centrosymmetric nature. In this thesis, I will describe our experimental investigations on two superconducting phases of Ruthenium-Boron (Ru-B) compounds. In one of these materials, RuB_2 (details in Chapter 4), the inversion symmetry is preserved in its crystal structure, but in the other one, Ru_7B_3 (details in Chapter 5), the inversion symmetry is broken. Apart from Ru_7B_3, for comparison, I will also describe our experimental studies on another non-centrosymmetric superconductor, AuBe (details in Chapter 3), where instead of boron, the heavy element gold is present.

1.3.4 Multiband Superconductors

Multiband superconductivity began to receive significant attention within the research community in 2001 when two-band superconductivity was discovered in MgB_2 [59, 81–85]. There were possibly two primary reasons behind that popularity. First of all, the high transition temperature (T_c = 40 K) of MgB_2 permitted numerous groups to study the material independently yet simultaneously. Second, in MgB_2, the two gaps are very distinctly visible and robust from experiments like Andreev reflection spectroscopy, tunneling spectroscopy etc [59–63].

However, it is interesting to note that more than forty years before these dis-

coveries, Harry Suhl, Bernd Theodor Matthias, and L. R. Walker [64] proposed an extension to the BCS theory [9] considering the contribution of more than one band in superconductivity, each crossing the Fermi surface. According to the BCS theory [9], the electronic part of the Hamiltonian for a superconductor can be written as follows.

$$H = \sum_{k\sigma} \epsilon_k c^*_{k\sigma} c_{k\sigma} + \sum_{kk'} V_{kk'} c^*_{k\uparrow} c^*_{-k\downarrow} c_{-k'\downarrow} c_{k'\uparrow} \tag{1.26}$$

where ϵ_k is the kinetic energy, $c^*_{i\sigma}$ ($c_{i\sigma}$) is the creation (annihilation) operator for an electron with momentum i and spin σ, and $V_{kk'}$ is the pairing potential. With analogy to the above expression, 'Suhl-Matthias-Walker' model [64] proposed the electronic part of the Hamiltonian for a multiband superconductor as:

$$\begin{aligned} H = \sum_{k\sigma} \epsilon_{k1} c^*_{k\sigma} c_{k\sigma} + \sum_{k\sigma} \epsilon_{k2} d^*_{k\sigma} d_{k\sigma} - V_{11} \sum_{kk'} c^*_{k\uparrow} c^*_{-k\downarrow} c_{-k'\downarrow} c_{k'\uparrow} \\ -V_{22} \sum_{kk'} d^*_{k\uparrow} d^*_{-k\downarrow} d_{-k'\downarrow} d_{k'\uparrow} - V_{12} \sum_{kk'} (c^*_{k\uparrow} c^*_{-k\downarrow} d_{-k'\downarrow} d_{k'\uparrow} + d^*_{k\uparrow} d^*_{-k\downarrow} c_{-k'\downarrow} c_{k'\uparrow}) \end{aligned} \tag{1.27}$$

where ϵ_{k1} and ϵ_{k2} are the kinetic energies corresponding to the two electronic bands (say band-1 and band-2), c^*_i and c_i are the creation and annihilation operators for band-1, and d^*_i and d_i are the creation and annihilation operators for band-2. V_{11}, V_{22} and V_{12} are the average interaction energies for the phonon emission and absorption process within two electrons both from band-1, two electrons both from band-2, and two electrons from two different bands, respectively. As each band contributes differently in superconductivity, the overall superconducting gap (Δ), unlike pure 's-wave superconductors', becomes anisotropic in the momentum space. According to that model, it is possible to resolve the two distinct gaps in the quasiparticle excitation spectrum of such materials. The amplitudes of the two gaps will depend on two primary parameters, a) the electron-phonon coupling strength of the corresponding band (V_{11} and V_{22}) and b) the interband coupling between the bands (V_{12}). The latter term also describes the tunneling of Cooper pairs between the two bands themselves. In Fig. 1.5, different possibilities [64] of the temperature dependences of the two gaps (Δ_1 and Δ_2) are shown, depending

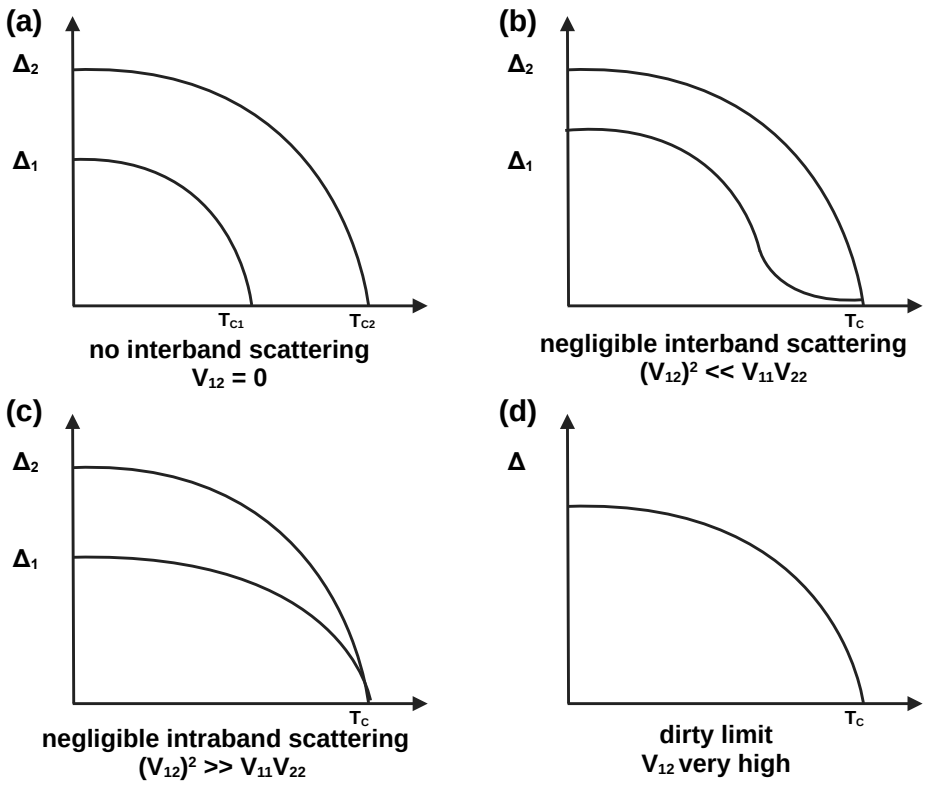

Figure 1.5: The different possibilities of the T dependences of the two gaps Δ_1 and Δ_2 depending on different relative strengths of the coupling parameters V_{11}, V_{22}, and V_{12}. **(a)** when there is no interband scattering, **(b)** when interband scattering is negligible, **(c)** when interband scattering is stronger than the intraband scatterings, and **(a)** when interband scattering is very strong.

on the different relative strengths of the coupling parameters.

Within the next decade, the model was used to explain the anomaly in the heat capacity data of elements such as Nb, Ta, V, etc. [86] and compounds like V_3Si [87], all of which were concluded to be multiband superconductors even in their purest form. In this thesis, I will describe two such superconductors, AuBe (Chapter 3) and RuB_2 (Chapter 4), where, based on our scanning tunneling spectroscopic measurements, we found the signatures of multiband superconductivity.

Bibliography

[1] H Kamerlingh Onnes. The discovery of superconductivity. *Commun. Phys. Lab*, 12:120, 1911.

[2] WD Allen, RH Dawton, Marianne Bär, K Mendelssohn, and JL Olsen. Superconductivity of Tin isotopes. *Nature*, 166(4234):1071–1072, 1950.

[3] HA Boorse, DB Cook, and MW Zemansky. Superconductivity of Lead. *Physical Review*, 78(5):635, 1950.

[4] TG Berlincourt and RR Hake. Superconductivity at high magnetic fields. *Physical Review*, 131(1):140, 1963.

[5] Walther Meissner and Robert Ochsenfeld. Ein neuer effekt bei eintritt der supraleitfähigkeit. *Naturwissenschaften*, 21(44):787–788, 1933.

[6] Michael Tinkham. *Introduction to superconductivity*. Courier Corporation, 2004.

[7] F London. Royal society of london. *Proceedings A149*, 71, 1935.

[8] VL Ginzburg and LD Landau. Zh. Eksp. Teor. Fiz. *SSSR 20*, 1063, 1950.

[9] John Bardeen, Leon N Cooper, and John Robert Schrieffer. Theory of superconductivity. *Physical Review*, 108(5):1175, 1957.

[10] Jennifer Eve Hoffman. *A Search for Alternative Electronic Order in the High Temperature Superconductor $Bi_2Sr_2CaCu_2O_{8+\delta}$ by Scanning Tunneling Microscopy*. PhD thesis, Citeseer, 2003.

[11] WS Corak, BB Goodman, CB Satterthwaite, and A Wexler. Exponential temperature dependence of the electronic specific heat of superconducting Vanadium. *Physical Review*, 96(5):1442, 1954.

[12] WS Corak, BB Goodman, CB Satterthwaite, and A Wexler. Atomic heats of normal and superconducting Vanadium. *Physical Review*, 102(3):656, 1956.

[13] MA Biondi, MP Garfunkel, and AO McCoubrey. Millimeter wave absorption in superconducting Aluminum. *Physical Review*, 101(4):1427, 1956.

[14] RE Glover III and M Tinkham. Transmission of superconducting films at millimeter-microwave and far infrared frequencies. *Physical Review*, 104(3):844, 1956.

[15] CA Reynolds, Bernard Serin, WH Wright, and LB Nesbitt. Superconductivity of isotopes of Mercury. *Physical Review*, 78(4):487, 1950.

[16] Emanuel Maxwell. Isotope effect in the superconductivity of Mercury. *Physical Review*, 78(4):477, 1950.

[17] JP Carbotte. Properties of boson-exchange superconductors. *Reviews of Modern Physics*, 62(4):1027, 1990.

[18] Leon N Cooper. Bound electron pairs in a degenerate Fermi gas. *Physical Review*, 104(4):1189, 1956.

[19] Herbert Fröhlich. Theory of the superconducting state. I. the ground state at the absolute zero of temperature. *Physical Review*, 79(5):845, 1950.

[20] Philip Phillips. *Advanced solid state physics*. Cambridge University Press, 2012.

[21] Sirohi Anshu. *Probing Conventional and Unconventional Superconductivity by Ultra-Low-Temperature Scanning Tunneling Spectroscopy*. PhD thesis, Indian Institute of Science Education and Research, Mohali, 2019.

[22] NN Bogoljubov, Vladimir Veniaminovic Tolmachov, and DV Širkov. A new method in the theory of superconductivity. *Fortschritte der Physik*, 6(11-12):605–682, 1958.

[23] GE Blonder, M Tinkham, and TM Klapwijk. Transition from metallic to tunneling regimes in superconducting microconstrictions: Excess current, charge imbalance, and supercurrent conversion. *Physical Review B*, 25(7):4515, 1982.

[24] Rafael M Fernandes. Lecture notes: BCS theory of superconductivity, 2020.

[25] Alfred Brian Pippard. Trapped flux in superconductors. *Philosophical Transactions of the Royal Society of London. Series A, Mathematical and Physical Sciences*, 248(941):97–129, 1955.

[26] Alexei Alexeyevich Abrikosov. The magnetic properties of superconducting alloys. *Journal of Physics and Chemistry of Solids*, 2(3):199–208, 1957.

[27] Lars Onsager. Statistical hydrodynamics. *II Nuovo Cimento (1943-1954)*, 6(2):279–287, 1949.

[28] Richard P Feynman. Chapter ii application of quantum mechanics to liquid Helium. In *Progress in Low-temperature Physics*, volume 1, pages 17–53. Elsevier, 1955.

[29] U Krägeloh. Flux line lattices in the intermediate state of superconductors with ginzburg landau parameters near $1/\sqrt{2}$. *Physics Letters A*, 28(9):657–658, 1969.

[30] U Essmann. Observation of the mixed state. *Physica*, 55:83–93, 1971.

[31] DR Aston, LW Dubeck, and F Rothwarf. Intermediate mixed state of type-II superconductors. *Physical Review B*, 3(7):2231, 1971.

[32] AE Jacobs. Interaction of vortices in type-II superconductors near $T=T_c$. *Physical Review B*, 4(9):3029, 1971.

[33] J Auer and H Ullmaier. Magnetic behavior of type-II superconductors with small ginzburg-landau parameters. *Physical Review B*, 7(1):136, 1973.

[34] I Luk'yanchuk. Theory of superconductors with κ close to $1/\sqrt{2}$. *Physical Review B*, 63(17):174504, 2001.

[35] EB Bogomol'nyi. The stability of classical solutions. *Sov. J. Nucl. Phys.(Engl. Transl.);(United States)*, 24(4), 1976.

[36] Laurence Jacobs and Claudio Rebbi. Interaction energy of superconducting vortices. *Physical review B*, 19(9):4486, 1979.

[37] Alexei Vagov, AA Shanenko, MV Milošević, Vollrath M Axt, VM Vinokur, J Albino Aguiar, and FM Peeters. Superconductivity between standard types: Multiband versus single-band materials. *Physical Review B*, 93(17):174503, 2016.

[38] WY Córdoba-Camacho, RM da Silva, A Vagov, AA Shanenko, and J Albino Aguiar. Between types I and II: Intertype flux exotic states in thin superconductors. *Physical Review B*, 94(5):054511, 2016.

[39] Sebastian Wolf, Alexei Vagov, AA Shanenko, Vollrath M Axt, A Perali, and J Albino Aguiar. BCS-BEC crossover induced by a shallow band: Pushing standard superconductivity types apart. *Physical Review B*, 95(9):094521, 2017.

[40] Sebastian Wolf, Alexei Vagov, AA Shanenko, Vollrath M Axt, and J Albino Aguiar. Vortex matter stabilized by many-body interactions. *Physical Review B*, 96(14):144515, 2017.

[41] AC Rose Innes and EH Rhoderick. *Introduction to superconductivity*. Pergamon Press, 1980.

[42] Drew Jared Rebar. Exploring superconductivity in chiral structured AuBe. *PhD Thesis*, 1(1):1, 2015.

[43] HW Weber, JF Sporna, and E Seidl. Transition from type-II to type-I superconductivity with magnetic field direction. *Physical Review Letters*, 41(21):1502, 1978.

[44] JF Sporna, E Seidl, and HW Weber. Anisotropy of the superconductive to normal transition in Tantalum-Nitrogen single crystals. *Journal of Low-temperature Physics*, 37(5):639–661, 1979.

[45] Yoji Koike, Sei-ichi Tanuma, Hiroyoshi Suematsu, and Kohei Higuchi. Superconductivity in the graphite-potassium intercalation compound C_8K. *Journal of Physics and Chemistry of Solids*, 41(10):1111–1118, 1980.

[46] E Moser, E Seidl, and HW Weber. Superconductive properties of vanadium and their impurity dependence. *Journal of Low-temperature Physics*, 49(5):585–607, 1982.

[47] Franz M Sauerzopf, E Moser, Harald W Weber, and FA Schmidt. Anisotropy effects in Tantalum, Niobium, and Vanadium down to the millikelvin temperature range. *Journal of Low-temperature Physics*, 66(3):191–208, 1987.

[48] HW Weber, E Seidl, M Botlo, C Laa, E Mayerhofer, FM Sauerzopf, RM Schalk, HP Wiesinger, and J Rammer. Magnetization of low-κ superconductors I the phase transition at H_{c1}. *Physica C: Superconductivity*, 161(3):272–286, 1989.

[49] Isaías G de Oliveira. The threshold temperature where type-I and type-II interchange in mesoscopic superconductors at the Bogomolnyi limit. *Physics Letters A*, 381(14):1248–1254, 2017.

[50] Dongting Zhang, Tian Le, Baijiang Lv, Lichang Yin, Chufan Chen, Zhiyong Nie, Dajun Su, Huiqiu Yuan, Zhu-An Xu, and Xin Lu. Full superconducting gap and type-I to type-II superconductivity transition in single-crystalline $NbGe_2$. *Physical Review B*, 103(21):214508, 2021.

[51] Goutam Sheet. *Point-contact Andreev Reflection Spectroscopy on Superconductors and Ferromagnets*. PhD thesis, Tata Institute of Fundamental Research Mumbai, 2006.

[52] Yoshiteru Maeno, T Maurice Rice, and Manfied Sigrist. The intriguing superconductivity of Strontium Ruthenate. *Physics Today*, 54(1):42–47, 2001.

[53] Takuji Nomura and Kosaku Yamada. Detailed investigation of gap structure and specific heat in the p-wave superconductor Sr_2RuO_4. *Journal of the Physical Society of Japan*, 71(2):404–407, 2002.

[54] DA Wollman, DJ Van Harlingen, WC Lee, DM Ginsberg, and AJ Leggett. Experimental determination of the superconducting pairing state in YBCO from the phase coherence of YBCO-Pb dc SQUIDs. *Physical Review Letters*, 71(13):2134, 1993.

[55] CC Tsuei, John R Kirtley, CC Chi, Lock See Yu-Jahnes, A Gupta, T Shaw, JZ Sun, and MB Ketchen. Pairing symmetry and flux quantization in a tricrystal superconducting ring of $YBa_2Cu_3O_{7-\delta}$. *Physical Review Letters*, 73(4):593, 1994.

[56] Roland Willa, Matthias Hecker, Rafael M Fernandes, and Jörg Schmalian. Inhomogeneous time-reversal symmetry breaking in Sr_2RuO_4. *Physical Review B*, 104(2):024511, 2021.

[57] AA Abrikosov and LP Gor'kov. Contribution to the theory of superconducting alloys with paramagnetic impurities. *Zhur. Eksptl'. i Teoret. Fiz.*, 39, 1960.

[58] A Lanzara, PV Bogdanov, XJ Zhou, SA Kellar, DL Feng, ED Lu, T Yoshida, H Eisaki, Atsushi Fujimori, K Kishio, et al. Evidence for ubiquitous strong electron-phonon coupling in high-temperature superconductors. *Nature*, 412(6846):510–514, 2001.

[59] F Giubileo, Dimitri Roditchev, William Sacks, Ronan Lamy, DX Thanh, Jean Klein, S Miraglia, Daniel Fruchart, J Marcus, and Ph Monod. Two-gap state density in MgB_2: a true bulk property or a proximity effect? *Physical Review Letters*, 87(17):177008, 2001.

[60] H Schmidt, JF Zasadzinski, KE Gray, and DG Hinks. Evidence for two-band superconductivity from break-junction tunneling on MgB_2. *Physical Review Letters*, 88(12):127002, 2002.

[61] Maria Iavarone, G Karapetrov, AE Koshelev, WK Kwok, GW Crabtree, DG Hinks, WN Kang, Eun-Mi Choi, Hyun Jung Kim, Hyeong-Jin Kim, et al. Two-band superconductivity in MgB_2. *Physical Review Letters*, 89(18):187002, 2002.

[62] RS Gonnelli, D Daghero, GA Ummarino, VA Stepanov, J Jun, SM Kazakov, and J Karpinski. Direct evidence for two-band superconductivity in MgB_2 single crystals from directional point-contact spectroscopy in magnetic fields. *Physical Review Letters*, 89(24):247004, 2002.

[63] Jose Angel Silva-Guillén, Y Noat, T Cren, W Sacks, Enric Canadell, and Pablo Ordejon. Tunneling and electronic structure of the two-gap superconductor MgB_2. *Physical Review B*, 92(6):064514, 2015.

[64] H Suhl, BT Matthias, and LR Walker. Bardeen-cooper-schrieffer theory of superconductivity in the case of overlapping bands. *Physical Review Letters*, 3(12):552, 1959.

[65] Stephan Haas and Kazumi Maki. Anisotropic s-wave superconductivity in MgB_2. *Physical Review B*, 65(2):020502, 2001.

[66] Manfred Sigrist and Kazuo Ueda. Phenomenological theory of unconventional superconductivity. *Reviews of Modern physics*, 63(2):239, 1991.

[67] Manfred Sigrist, DF Agterberg, PA Frigeri, N Hayashi, RP Kaur, A Koga, I Milat, K Wakabayashi, and Y Yanase. Superconductivity in noncentrosymmetric materials. *Journal of Magnetism and Magnetic Materials*, 310(2):536–540, 2007.

[68] PA Frigeri, DF Agterberg, A Koga, and M Sigrist. Superconductivity without inversion symmetry: MnSi versus $CePt_3Si$. *Physical Review Letters*, 92(9):097001, 2004.

[69] Ernst Bauer, Gerfried Hilscher, Herwig Michor, Ch Paul, Ernst-Wilhelm Scheidt, A Gribanov, Yu Seropegin, H Noël, M Sigrist, and Peter Rogl. Heavy fermion superconductivity and magnetic order in noncentrosymmetric $CePt_3Si$. *Physical Review Letters*, 92(2):027003, 2004.

[70] RP Kaur, DF Agterberg, and Manfred Sigrist. Helical vortex phase in the noncentrosymmetric $CePt_3Si$. *Physical Review Letters*, 94(13):137002, 2005.

[71] Masatoshi Sato and Satoshi Fujimoto. Topological phases of noncentrosymmetric superconductors: Edge states, majorana fermions, and non-abelian statistics. *Physical Review B*, 79(9):094504, 2009.

[72] Ernst Bauer and Manfred Sigrist. *Non-centrosymmetric superconductors: introduction and overview*, volume 847. Springer Science & Business Media, 2012.

[73] HQ Yuan, DF Agterberg, N Hayashi, P Badica, D Vandervelde, K Togano, M Sigrist, and MB Salamon. s-wave spin-triplet order in superconductors without inversion symmetry: Li_2Pd_3B and Li_2Pt_3B. *Physical Review Letters*, 97(1):017006, 2006.

[74] M Nishiyama, Y Inada, and Guo-qing Zheng. Spin triplet superconducting state due to broken inversion symmetry in Li_2Pt_3B. *Physical Review Letters*, 98(4):047002, 2007.

[75] H Takeya, M ElMassalami, S Kasahara, and K Hirata. Specific-heat studies of the spin-orbit interaction in noncentrosymmetric $Li_2(Pd_{1-x}Pt_x)_3B$ (x = 0, 0.5, 1) superconductors. *Physical Review B*, 76(10):104506, 2007.

[76] M Yogi, Y Kitaoka, S Hashimoto, T Yasuda, R Settai, TD Matsuda, Y Haga, Y Ōnuki, Peter Rogl, and Ernst Bauer. Evidence for a novel state of superconductivity in noncentrosymmetric $CePt_3Si$: A Pt^{195} - NMR study. *Physical Review Letters*, 93(2):027003, 2004.

[77] N Kimura, K Ito, K Saitoh, Y Umeda, H Aoki, and T Terashima. Pressure-induced superconductivity in noncentrosymmetric heavy-fermion $CeRhSi_3$. *Physical Review Letters*, 95(24):247004, 2005.

[78] Ichiro Sugitani, Yusuke Okuda, Hiroaki Shishido, Tsutomu Yamada, Arumugam Thamizhavel, Etsuji Yamamoto, Tatsuma D Matsuda, Yoshinori Haga, Tetsuya Takeuchi, Rikio Settai, et al. Pressure-induced heavy-fermion superconductivity in antiferromagnet $CeIrSi_3$ without inversion symmetry. *Journal of the Physical Society of Japan*, 75(4):043703–043703, 2006.

[79] Takeshi Shibayama, Minoru Nohara, Hiroko Aruga Katori, Yoshihiko Okamoto, Zenji Hiroi, and Hidenori Takagi. Superconductivity in Rh_2Ga_9 and Ir_2Ga_9 without inversion symmetry. *Journal of the Physical Society of Japan*, 76(7):073708–073708, 2007.

[80] K Togano, P Badica, Y Nakamori, S Orimo, H Takeya, and K Hirata. Superconductivity in the metal-rich Li−Pd−B ternary boride. *Physical Review Letters*, 93(24):247004, 2004.

[81] Jun Nagamatsu, Norimasa Nakagawa, Takahiro Muranaka, Yuji Zenitani, and Jun Akimitsu. Superconductivity at 39 K in magnesium diboride. *nature*, 410(6824):63–64, 2001.

[82] G Karapetrov, M Iavarone, WK Kwok, GW Crabtree, and DG Hinks. Scanning tunneling spectroscopy in MgB_2. *Physical Review Letters*, 86(19):4374, 2001.

[83] F Bouquet, RA Fisher, NE Phillips, DG Hinks, and JD Jorgensen. Specific heat of $Mg^{11}B_2$: evidence for a second energy gap. *Physical Review Letters*, 87(4):047001, 2001.

[84] P Szabó, P Samuely, J Kačmarčík, Thierry Klein, J Marcus, Daniel Fruchart, Salvatore Miraglia, C Marcenat, and AGM Jansen. Evidence for two superconducting energy gaps in MgB_2 by point-contact spectroscopy. *Physical Review Letters*, 87(13):137005, 2001.

[85] XK Chen, MJ Konstantinović, JC Irwin, DD Lawrie, and JP Franck. Evidence for two superconducting gaps in MgB_2. *Physical Review Letters*, 87(15):157002, 2001.

[86] Lawrence Yun Lung Shen, NM Senozan, and Norman E Phillips. Evidence for two energy gaps in high-purity superconducting Nb, Ta, and V. *Physical Review Letters*, 14(25):1025, 1965.

[87] JCF Brock. Superconducting and mixed state specific heat of V_3Si. *Solid State Communications*, 7(24):1789–1792, 1969.

Chapter 2

Experimental Methods

The experimental investigations in this thesis are based on primarily two transport spectroscopic techniques, scanning tunneling spectroscopy (STS) and point-contact Andreev reflection spectroscopy (PCARS). The details of these methods and other associated techniques will be discussed in this chapter.

2.1 Scanning Tunneling Spectroscopy (STS)

Gerd Binning and Heinrich Rohrer [1] invented the STM in 1981 at IBM, Zurich. This invention completely revolutionized the arena of experimental condensed matter physics, and the two scientists were awarded the Nobel Prize in Physics five years later. This powerful technique provides topographic information resolvable up to the angstrom length scale. After its discovery, the technique is routinely used [2] to study the physics of low-energy excitations in condensed matter systems.

2.1.1 Working Principle of an STM

The basic scanning mechanism of an STM is represented in Fig. 2.1(a). Classically, a particle of energy E can pass through an energy barrier of height V, only if $E > V$. However, quantum mechanically, there is always some non-zero probability that the particle will cross the barrier even if $E < V$. This process is called quantum mechanical tunneling, and STM works on this principle, exploiting the

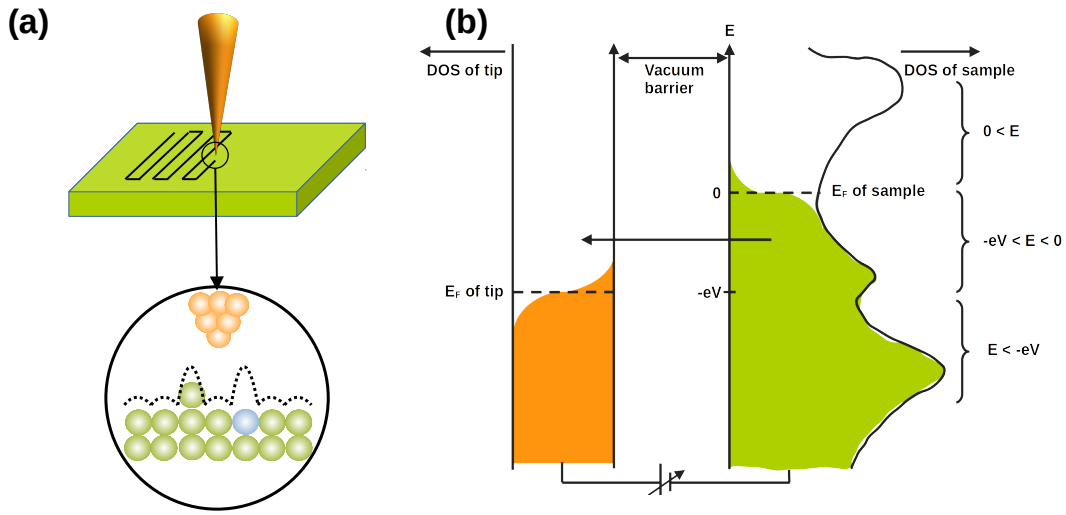

Figure 2.1: **(a)** A schematic representing the scanning mechanism in STM. **(b)** A schematic representing sample (normal metal) to tip (also normal metal) tunneling of charge carrier.

wave nature of electrons. In 1960, Giaever [3] first reported the tunneling between two metals (NIN junction) which was followed by further experimental reports [4]. In Fig. 2.1(b), such tunneling is explained from the perspective of the density of states. Later, Nicol, Shapiro, and Smith [5] reported the tunneling between a metal and a superconductor (NIS junction) and between two superconductors (SIS junctions) as well. The latter group also for the first time directly observed the superconducting gap in the quasiparticle excitation spectrum.

Crudely speaking, the tunneling current decays exponentially with increasing barrier thickness (d) according to the following equation.

$$I \propto \exp^{-2kd} \tag{2.1}$$

Due to this exponential dependence on the distance, the vertical resolution of STM is very high. However, for a real tunneling barrier, the complex geometries of the two terminals will affect the overall tunneling current and the contribution of multiple conduction channels should be taken into account. In 1961, Bardeen [6]

proposed a general formalism to describe electron tunneling between two electrodes considering all these minute details. The model was based on Fermi's golden rule derived from time-dependent perturbation theory. According to that model, the tunneling current for a SIN junction can be described by the following equation.

$$I = -\frac{4\pi e}{\hbar}\int_{-eV}^{0} |M|^2 N_n(E) N_s(E+eV)[f(E) - f(E+eV)]dE \qquad (2.2)$$

Where, $\hbar$ is the reduced Plank's constant, M is the tunneling matrix, $f(E)$ is the Fermi-Dirac distribution function, and $N_n(E)$ and $N_s(E)$ are the density of states of the normal metal and superconductor respectively. Compared to $N_s(E)$ (which varies on the energy scale of $\sim$ meV), $N_n(E)$ (which varies on the energy scale of $\sim$ eV) can be approximated as a constant near Fermi energy (E_F). This approximation will remain valid till the applied voltage V remains sufficiently low. The tunneling matrix M, which is the expectation value of the single particle transition probability across the barrier, can be approximated to be proportional to $\exp^{-2kd}$. Furthermore, at sufficiently low temperature, $f(E)$ can be approximated as a step function that sharply cuts at E_F [7]. Under all these conditions, the tunneling current can be approximated according to the following equation.

$$I = -\frac{4\pi e}{\hbar} e^{-2kd} N_n(\varepsilon)\int_{-eV}^{0} N_s(\varepsilon+eV)d\varepsilon \qquad (2.3)$$

The basic working principle of an STM is presented as a schematic in Fig. 2.2. A metallic wire (made of pure tungsten (W) or Platinum-Iridium (Pt-Ir) alloy) is used as the conducting tip. If the sample is cleavable, then a fresh surface is prepared *in-situ* in the preparation chamber. Alternatively, the surface is reversed sputtered (followed by an occasional annealing as well) to have a pristine surface. Then the tip is positioned close to such a clean sample surface (typically within a distance of a few angstroms) using the feedback loop. In such an arrangement, the vacuum acts as the potential barrier between the sample and the tip, and the tunneling current (typically of the order of picoamperes) can be measured either by applying an appropriate voltage bias to the sample w.r.t. the tip or the opposite. The geometric uniformity of the tip compared to the sample, and particularly in our set up, multiple electrical connections to the tip assembly makes grounding the

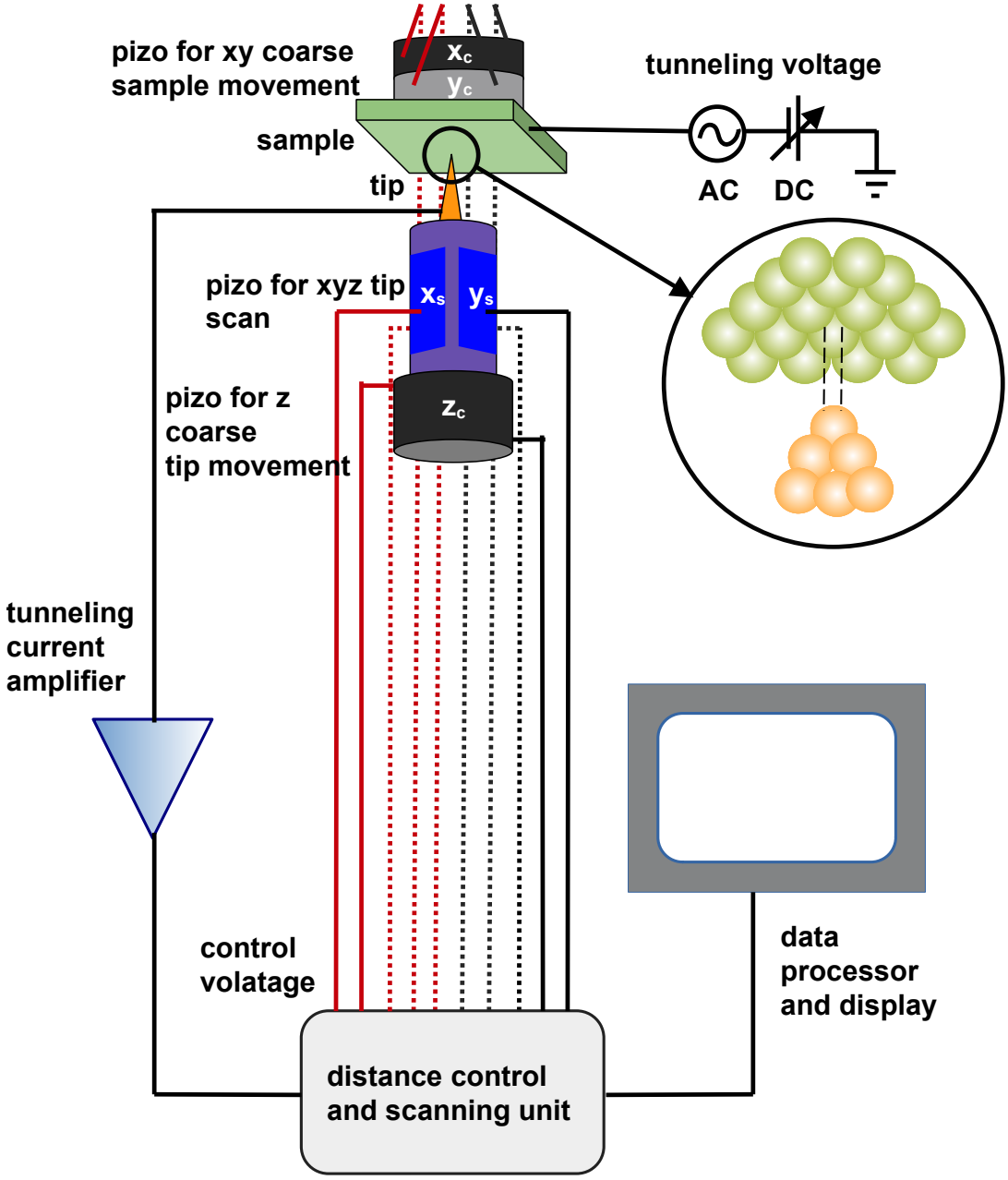

Figure 2.2: A schematic representing the working principle of the STM.

tip a better choice than the opposite. In the next section, I will discuss different modes of operation for an STM.

2.1.2 Different Modes of Operation

Topography

The most widespread use of an STM is the topographic imaging of a sample surface. This can be performed (thanks to the extreme spatial resolving power of this technique) up to the atomic resolution! A delicate feedback mechanism is the backbone of topographic imaging and the whole process can be performed in two different modes. In constant height mode, the tip scans the surface area moving in a fixed horizontal plane above the surface. As a result, the tunneling current varies according to the height profile (or local DOS). This variation of current is finally plotted as a function of position, which reflects the topography (or local electronic features) of the sample below. In constant current mode, the tunneling current is kept constant by the feedback mechanism, and the height of the tip from the sample is continuously adjusted according to the height (or local DOS) profile of the surface. This variation of height is plotted as a function of position, which ultimately reflects the topographic (or local electronic) features.

Local Density of States (LDOS)

Another popular mode of operation of an STM is to probe the local density of states of a material by measuring differential conductance through the tunneling current. This technique is popularly referred to as scanning tunneling spectroscopy (STS). Chapters 3 to 5 of this thesis are based on the analysis of STS data on three different superconductors. During the STS study, the tip is kept fixed at a particular position above the sample surface, and the feedback loop remains turned off. Differentiating the expression of tunneling current (I) in Eqn. 2.3 w.r.t. applied bias (V), we get:

$$\frac{dI}{dV} = \frac{-4\pi e}{\hbar} e^{-2kd} N_n(\varepsilon) \frac{d}{dV} \left(\int_{-eV}^{0} N_s(\varepsilon + eV) d\varepsilon \right) \tag{2.4}$$

where, according to BCS theory, the superconducting density of state is described as

$$N_s(E) = \left(\frac{E}{\sqrt{E^2 - \Delta^2}} \right) \tag{2.5}$$

In the above expression, Δ is the superconducting energy gap. In pure BCS theory, the quasiparticle lifetime is considered infinite. To make this model more practical, the above expression was later modified by Dynes [8] as follows.

$$N_S(E) = \mathrm{Re}\left(\frac{(E - i\Gamma)}{\sqrt{(E - i\Gamma)^2 - \Delta^2}} \right) \tag{2.6}$$

Here, Γ is the effective broadening parameter for the DOS, and the primary (but not exclusive) reason for the broadening is the finite lifetime of the quasiparticle. As can be seen from Eqn. 2.4, by sweeping the biasing voltage V, it is possible to scan the LDOS $N_s(\epsilon)$ of a superconductor. And as can be seen from Eqn. 2.6, measured $N_s(\epsilon)$ can directly provide information about the superconducting gap Δ. Throughout this thesis, the experimental STS data will be analyzed on the basis of the above Dynes' model, unless explicitly mentioned otherwise.

LDOS Mapping

LDOS mapping is a hybrid technique of the two modes mentioned above, in which both imaging and spectroscopy are performed, but one at a time. Feedback is enabled during imaging but disabled during spectroscopy measurements. Rather than measuring the LDOS at a fixed point on the sample surface, the same process can be continued at different points on the surface. Once we have LDOS data at every point (practically some periodic points with separation adjusted) on the surface, we can slice the LDOS (conductivity dI/dV) at a particular energy (bias V) for all such plots. That way we can map the LDOS (corresponding to that particular energy) pixel-wise on the real space. Slicing the dI/dV graphs at a different bias will provide an LDOS map of the same surface for a different energy value.

2.1.3 Our System

The STM system at IISER Mohali was installed in August 2016. The system was built by UNISOKU, Japan with a cryostat manufactured by JANIS, USA. The measurements in this system can be operated at a minimum temperature of 280 mK in an environment of 10^{-10} mbar ultra-high vacuum (UHV) and a maximum 11 T magnetic field along the z-axis. The system consists of four different chambers (a load lock chamber (LLC), a preparation chamber (PC), an exchange chamber (EC), and an STM chamber) separated by gate valves. As STM/S is a highly surface-sensitive technique, it is necessary to avoid oxidation and surface contamination of the material under study. If the material is a cleavable single crystal, then it is cleaved in the UHV environment before starting the experiment. However, for all three materials described in this thesis (which were studied in the STM), that process was not possible. Therefore, as an alternative process, a few layers of the surface were removed by mild reverse sputtering in the argon environment *in-situ* within the UHV PC. The transfer of the sample and tip holder from one chamber to the next is performed by UHV magnetic manipulators. As mentioned before, a typical tip-sample distance is $\sim$ angstrom, and the tunneling current between them is $\sim$ picoampere. To measure and maintain such an extremely small distance and current and also to get an atomic resolution image, all possible sources of noises like vibrational, acoustic, and electromagnetic must be isolated from the scanning space. For that purpose, the STM at IISER Mohali is situated inside a Faraday cage, above a giant cubic concrete pit (of approximately 5 m (l) $\times$ 4.5 m (w) $\times$ 3.5 m (d) dimension), inside a separate dedicated building. The scanning is performed by the single tube-type piezo-driver which is driven by six electrodes. Four outer electrodes are used for lateral (+X, -X, +Y, and -Y) movements, one outer electrode is used for vertical Z scan, and the last inner electrode is used for vertical Z offset. The tube-type piezo is located in the approach stage and is supported by an inertial piezo slider (IPS) device within the approach stage holder. This IPS device works by the combination of friction and inertial movement controlling motion (popularly called slip-stick mechanism [9]). In Fig. 2.3, a schematics [10] of the STM inside the cryostat are represented.

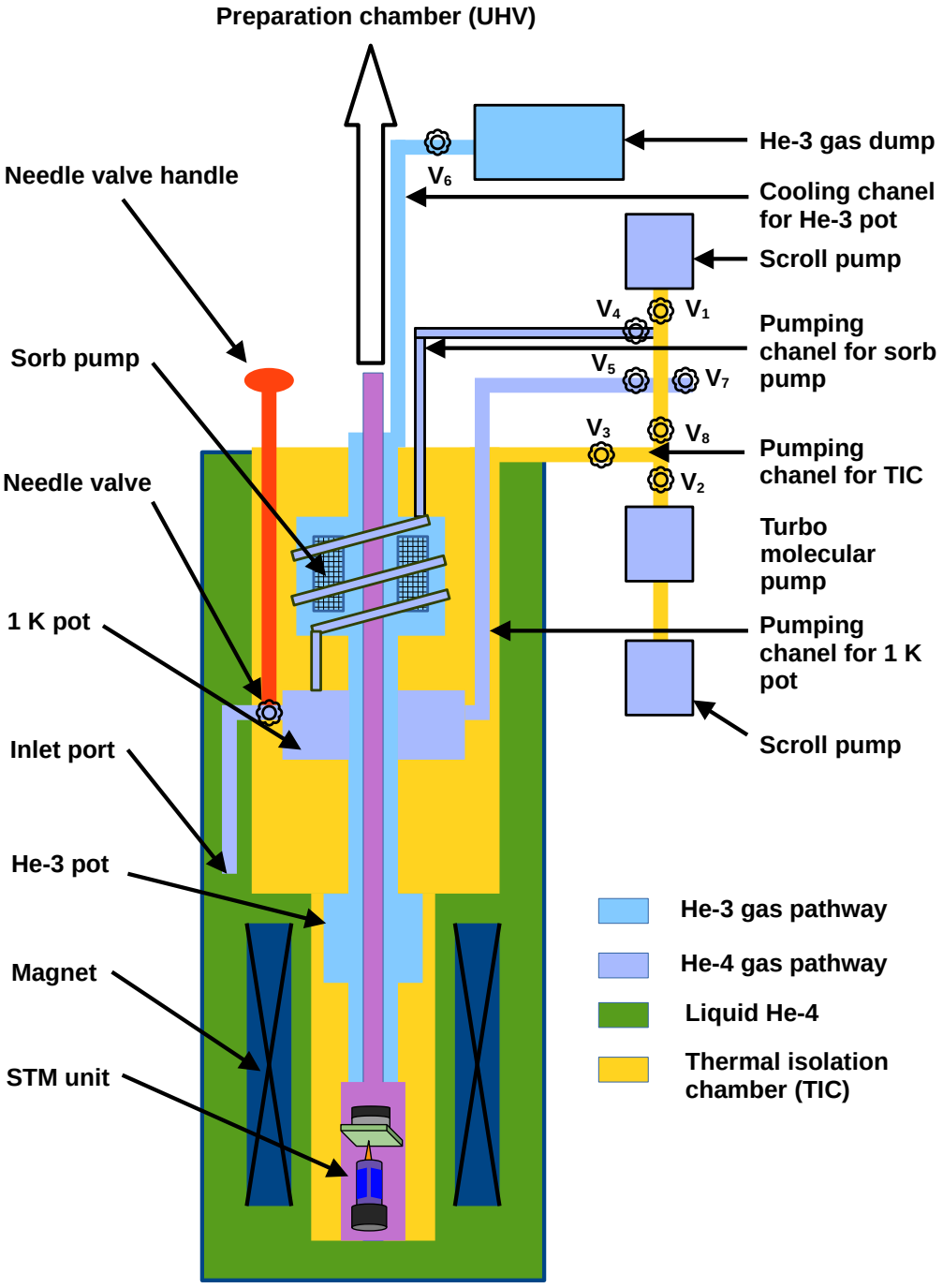

Figure 2.3: The schematic of the cryostat with different chamber components.

2.1.4 Preparation of STM Tip

During STM imaging, the tip is expected to detect the tunneling current from a single atom on the sample surface. This can only be ensured for a tip that has a single atom at the bottom of it. Practically, neither it is possible to confirm nor such a geometry is stable. The best thing we can do is to prepare a tip that has as sharp an apex as possible. All the STM/S data described in the next three chapters were probed by STM tips made from tungsten (W) wire. The reason for choosing W is its nearly flat electronic density of state (DOS) near the Fermi energy (E_F). In addition, an extremely sharp W tip can be prepared [10, 11] very easily by the chemical etching process. The arrangement for electrochemical etching is presented in Fig. 2.4(a). A W wire (generally of 0.5 mm diameter) is cut into a small piece and scratched with a sandpaper (generally P8000 grade) to roughly remove the oxide layers. Then a horizontally arranged Pt ring and the piece of W wire coaxial to that, both are suspended into a Potassium Hydroxide (KOH) solution (generally 1.2 N), and a voltage (generally 10 V) is applied between them. A set current (generally 1 mA) is also fixed to stop the etching process after the lower part falls off. The chemical erosion begins from all sides of the wire, predominantly near the meniscus (where the distance between the wire and the ring is minimum). The wire continues to become thinner at that point, and after a certain time (approximately 20 minutes), the lower part simply falls off. The remaining wire, as a result, gets a very sharp apex at the bottom (see Fig. 2.4(b) for an example) and can be used as a tip for STM measurement. After the process is complete, the tip is immediately dipped in distilled water followed by ethanol to avoid the formation of oxide layers.

Various parameters like strength and amount of the solution, the calmness of its surface during the process, etc., affect the shape and the overall quality of the tip. Two tips, one of good shape and another of uneven shape, are shown in Fig. 2.4. To note, the only thing that practically matters for the tip is its sharp apex (ideally a single atom at the end), not the shape beyond that. If the tip is exposed to air for an extended period of time, it can become oxidized or contaminated. For that reason, like the sample, the tip apex is also cleaned inside the UHV PC with

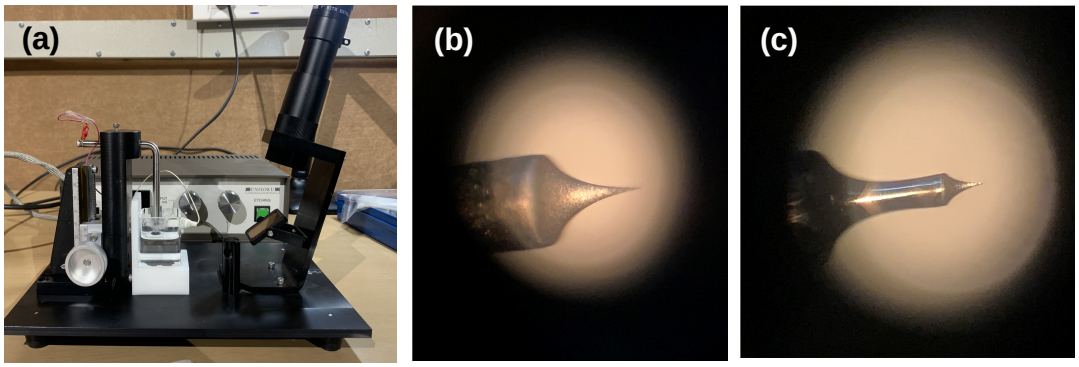

Figure 2.4: **(a)** Arrangement for preparing a tip with electrochemical etching. **(b)** A perfect-looking tip and **(c)** a not-so-perfect one due to mistake during preparation.

electron bombardment before any experimental measurements. A high voltage is used to heat the filament, and an accelerating voltage is used between the tip and the filament to allow electrons to heat the tip apex.

2.1.5 Measurement

The next three chapters of this thesis focus primarily on spectroscopy (STS) rather than microscopy (STM). Theoretically, once we have $I-V$ characteristics measured for a superconductor, $dI/dV vs. V$ is expected to be a straightforward derivative of that. However, as a better method from experimental perspective, the dI/dV is simultaneously measured with a small ac signal (V_{ac}) superimposed on the input dc signal (V_{dc}). Although extremely successful, this strategy invites a specific problem, particularly for STS measurements [11]. Because the tip and the sample do not meet, it acts as a capacitor for any ac signal. Therefore, the phase of the input and output signal must be taken care of, and usually a lock-in amplifier does this job. With a phase-sensitive lock-in amplifier, we can measure the first harmonic without losing any information. From the following Taylor's expansion it can be seen that the coefficient of the first harmonic is proportional to dI/dV:

$$
\begin{aligned}
&I(V = V_{dc} + V_{ac}cos\omega t) \\
&\quad = I(V_{dc}) + \left(\frac{dI}{dV}\right)|_{V_{dc}}\, V_{ac}cos\omega t + \frac{1}{4}\left(\frac{d^2I}{dV^2}\right)|_{V_{dc}}\, (V_{ac})^2(1 + cos2\omega t) + \cdots
\end{aligned}
\tag{2.7}
$$

Therefore, to measure dI/dV, the signal is locked in the first harmonic. For V_{ac}, $< 5\%$ of V_{dc} is generally chosen.

2.2 Point Contact Andreev Reflection Spectroscopy (PCARS)

Apart from STS, another spectroscopic technique used in this thesis is point contact Andreev reflection spectroscopy (PCARS) [12]. A contact is called a 'point-contact' if the diameter of the contact is of the order of characteristic length scales [13] (such as the elastic and inelastic mean free path of electrons) of the materials. This technique is comparable to tunneling spectroscopy, except that here the tip physically touches the sample and scattering occurs at the junction of a regular metal and a superconductor (NS). Compared to STS, PCARS is less surface sensitive. Furthermore, the inelastic scattering of the tunneling electrons between normal metals creates more channels for the electrons to tunnel through the barrier, whereas in PCARS, the inelastic scattering of the electrons contributes negatively to the total current.

Point-contact spectroscopy is widely used [14, 15] to extract energy and momentum resolved information of a material. For a superconductor, the technique provides precise information on the superconducting energy gap and its symmetry [16–19], for a ferromagnet, it provides information on transport spin-polarization [20–22], and for a metal (or any good conductor) it provides the materials' phonon spectra [23, 24]. Fig. 2.5(a) shows a schematic of this technique where two contacts are attached to the tip and two more are attached to the sample. We detect the voltage drop across the point-contact by transmitting a small amount of modulated current ($I_{dc} + I_{ac}sinwt$) using a current source (Keithley

6220) and the lock-in amplifier (Stanford Research Systems SR830) at a specific frequency.

In 1966, Wexler [25] introduced a generalized expression for the resistance of a point contact between two metals, which reads as follows.

$$R_{PC} = \frac{2h/e^2}{(ak_F)^2} + \Gamma(l/a)\frac{\rho(T)}{2a} \tag{2.8}$$

Here, h is the Planck's constant, e is the electronic charge, a is the contact diameter, k_F is the Fermi momentum, l is the mean free path (elastic or inelastic) of an electron, ρ is the bulk resistivity of the material, T is the effective temperature at the point-contact and Γ denotes a slowly varying function of the order of unity [12]. Depending on the contact diameter, the transport of electrons through a point contact is classified into different regimes. In the next section, I will briefly discuss these regimes.

2.2.1 Different Regimes of Electronic Transport

Quantum Regime

If the diameter of point contact is on the order of the de Broglie wave length of the electron ($\sim$ angstrom), the transport is defined as in the quantum regime. Here, conductance gets quantized [26, 27] i.e, $G_0 = N\frac{2e^2}{h}$, where N is the number of conducting channels.

Ballistic Regime

The contact is said to be in the ballistic regime when the diameter of the point-contact is larger than the de-Broglie wave length of electron but less than the electronic elastic mean free path (l_e), i.e. $a < l_e$. Statistically, the electrons do not undergo any inelastic scattering across the interface in this regime, and they pass through the contact with no dissipation. However, due to the large number of conducting channels, there is always some finite resistance at a mesoscopic contact. In 1965, Gantmakher and Sharvin [28] derived the expression for this resistance by solving the problem of a dilute gas passing through a small hole. In Eqn. 2.8 for

Wexler's formula, the first term represents the Sharvin's resistance (R_S). As can be seen, only the geometry of the point-contact determines Sharvin's resistance and not the bulk resistivity of the material. In this contact regime, electrons gain sufficient energy to produce elementary excitations like phonons and magnons, resulting in the non-linearity in the $I - V$ characteristics. That is why energy-resolved spectroscopy is always preferable in the ballistic regime. For the PCARS data presented in this thesis, only the spectra in the pure ballistic regime are considered for analysis.

Thermal Regime

In the thermal regime, the contact diameter is larger than the electronic inelastic mean free path (l_i) i.e. $a > l_i$ and electrons undergo both elastic and inelastic scattering. Maxwell calculated the formula for resistance in this regime by solving the Poisson equation with relevant boundary conditions. In Eqn. 2.8 for Wexler's formula, the second term represents the Maxwell's resistance (R_M). Unlike R_S, R_M depends directly on the bulk resistivity of the materials forming the point-contact. In this regime, electrons dissipate energy within the contact region, which leads to joule heating and consequent increase in the local temperature of the contact (T_{eff}) with respect to the bath temperature (T_{bath}). Any temperature measurement would provide T_{bath} but not T_{eff} which increases with the applied voltage. Thus, energy-resolved information cannot be obtained in the thermal regime [29, 30].

Intermediate Regime

In the intermediate regime, the contact diameter lies in between two extreme regimes, i.e. ballistic and thermal. Consequently, both Sharvin's and Maxwell's resistances contribute in this regime, and Wexler's formula in Eqn. 2.8 perfectly describes the total contact resistance.

2.2.2 Superconductor-Normal Metal Interface

The different regimes and the corresponding expressions for resistance I have discussed in the last section are for point contacts between two normal metals (NN

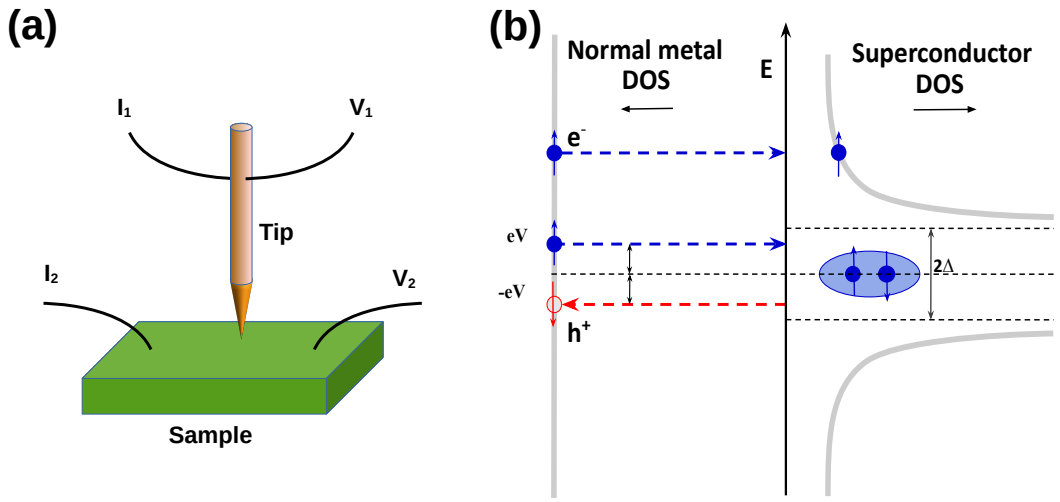

Figure 2.5: **(a)** The schematic representing a point contact formed between a tip and a sample. **(b)** A schematic representing normal transmission and Andreev reflection process for electrons from the interface between a metal and a superconductor.

junction). In this section we will extend that towards a point contact between a superconductor and a normal metal (NS junction) where nonlinearity in resistance comes in picture. Fig. 2.5(b) depicts the electron transport events at the interface between a normal metal and a superconductor. The density of states of a normal metal is illustrated on the left, whereas that of a superconductor is presented on the right. If due to an applied voltage across the junction, the electronic energy (say E_1) is greater than the superconducting energy gap Δ, the electron will transmit through the barrier to a vacant state on the other side. However, such a transmission will not be possible if the electronic energy (say E_2) is less than Δ. In such a situation, the electron will undergo a reflection from the interface, which can occur in two different ways. In the usual way, the electron can reflect back as it is i.e. as an electron with the same spin. This process is called normal reflection. Alternatively, the electron can reflect back as a hole with opposite spin. In this situation, due to the conservation of momentum and spin, there will be the formation of a cooper pair on the superconducting side near E_F. This special type of reflection is called the Andreev reflection [31].

2.2.3 BTK Formalism

The Andreev reflection as described in the previous section can be analyzed within the framework of Blonder-Tinkham-Klapwijk (BTK) theory [32]. This is a one-dimensional model (can also be modified for higher dimensions) that considers all possible processes like transmission, normal reflection, and Andreev reflection, which can occur at an NS junction when electrons move perpendicular to the interface. The analysis requires the data of normalized differential conductance ($\frac{(dI/dV)}{(dI/dV)_N}$) vs. applied voltage ($V$) (where $(dI/dV)_N$ is the normal state differential conductance across the junction). Within this model, the interface of normal metal and superconductor is represented by a delta function potential $H' = V_0\delta(x)$ and the strength of the barrier potential is characterized by a dimensionless parameter $Z = \frac{V_0}{\hbar v_F}$. As the parameter Z depends on the strength of the barrier potential (generally due to the oxide layer between the sample and the tip) and the difference in the Fermi velocity v_F of the two materials, it can never be exactly 'zero', which means that the electrons will always have some finite probability of normal reflection. In BTK theory, the v_F of normal metal and the superconductor are considered to be equal for the sake of simplicity. For a point contact between two materials with a large difference in v_F, the effective Z can be written as $Z_{eff} = Z + \frac{(1-r)^2}{4r}$, where $r = v_{F_N}/v_{F_S}$. According to the BTK theory, the current through the interface of a normal metal and a superconductor can be described as follows:

$$I_{ballistic} \propto N(0)v_F \int_{-\infty}^{\infty} [f(E - eV) - f(E)]\,[1 + A(E) - B(E)]dE \qquad (2.9)$$

where, $N(0)$ is the density of states at E_F and the coefficients $A(E)$ and $B(E)$ are the probabilities of Andreev reflection and normal reflection, respectively, which can be calculated by applying the appropriate boundary conditions of delta function and the Bogoliubov-de Gennes equation. Using this equation, the experimental data can be fitted, and information about the superconducting energy gap can be obtained. The values of $A(E)$ and $B(E)$ are represented in Table 2.1 below for different energy regimes with the following values of intermediate

coefficients u, v, ε and γ.

$$u^2 = \frac{1}{2}[1 + \frac{\sqrt{E^2 - \Delta^2}}{E}], v^2 = 1 - u^2,$$
$$\varepsilon = \frac{E^2 - \Delta^2}{E^2}, \gamma = u^2 + (u^2 - v^2)Z^2, \gamma^2 = \gamma\gamma^* \tag{2.10}$$

Coefficient	$E < \Delta$	$E > \Delta$
A(E)	$\frac{(\Delta/E)^2}{1-\varepsilon(1+2Z^2)^2}$	$\frac{(uv)^2}{\gamma^2}$
B(E)	1 - A(E)	$\frac{(u^2-v^2)^2Z^2(1+Z^2)}{\gamma^2}$

Table 2.1: Probabilities of Andreev and normal reflection at different energy ranges

In BTK theory, only the elastic scattering was considered at the interface. However, in reality, electrons also experience inelastic scattering. To compensate that, another parameter Γ associated with quasiparticle lifetime was introduced in the modified BTK model [33]. Consequently, in the expressions for u, v, ε, γ, $A(E)$ and $B(E)$ mentioned before, 'E' will be replaced by '$(E + i\Gamma)$' according to this model.

2.2.4 Directional PCARS

Generally, when we discuss the Fermi surface (FS), Fermi velocity (v_F) or the superconducting order parameter (Δ) (see Fig. 1.2 (b) in the previous chapter), we intuitively assume that they are isotropic in momentum space. This means that for a metal, the velocity of electrons is constant around an ideal spherical Fermi surface, and if the material becomes a superconductor, a gap of a constant thickness (2Δ) opens up in the density of state around that spherical FS. In reality, none of these are guaranteed to be true. The FS is a constant energy surface in momentum space, and v_F is the gradient of the electron energy with respect to k taken at E_F and is perpendicular to the FS. When a point contact is formed in the ballistic regime, electrons that cross the interface do not lose their momentum information. Using these two properties, PCARS can be used as an angle (or momentum direction) resolved probe to extract information about the shape of

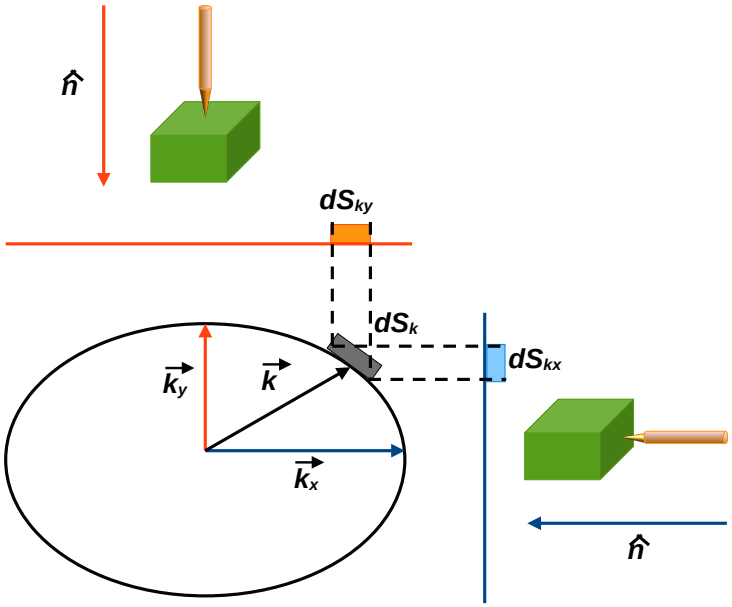

Figure 2.6: A schematic representing directional point contact spectroscopy where current injected from different directions probe different segments of the Fermi surface.

the FS as well as the symmetry of the superconducting gap if it opens up at that FS [34–36].

For a ballistic point contact between two metals, the current injected along $\hat{n}$ due to the net flux of electrons from the i'th band on the FS can be expressed as [30]:

$$I_i \propto \oint_{FS} N_{i\vec{k}} \left(\vec{v}_{ik}.\hat{n}\right) dS_k = \left\langle N_{i\vec{k}} \vec{v}_{ik\hat{n}} \right\rangle_{FS} = S_{i\hat{n}} \tag{2.11}$$

where $\vec{k}$ is the wave vector at the FS, $N_{i\vec{k}}$ is the density of states, $\vec{v}_{ik\hat{n}}$ is the component of the v_F along $\hat{n}$, dS_k is an elemental area on the FS centered at $\vec{k}$, and $S_{i\hat{n}}$ is the area of projection of the i-th band on the interface plane. As the current injected along $\hat{n}$ predominantly probes the FS in the vicinity of $\vec{k}$, the current injected from various directions will effectively probe the entire FS. For a FS with a non-spherical shape, the area of projection is different along different directions. The schematic in Fig. 2.6 can be useful to understand the mechanism. In addition,

the superconducting gap $\Delta_{\vec{k}}$ opened on the FS can have its own anisotropy. In such a case, the average value of $\Delta_{\vec{k}}$ measured for $I \parallel \hat{n}$ can be expressed as [37].

$$\langle \Delta \rangle = \left\langle \Delta_{\vec{k}} N_{\vec{k}} \vec{v}_{k\hat{n}} \right\rangle_{FS} / \left\langle N_{\vec{k}} \vec{v}_{k\hat{n}} \right\rangle_{FS} \tag{2.12}$$

Now, if a magnetic field is applied along a particular direction, $\Delta_{\vec{k}}$ will get suppressed in that direction depending on the anisotropy (if exists) of the upper critical field (H_{c2}) in that material. In addition, the anisotropy of H_{c2} can be a direct consequence of the anisotropy of $\Delta_{\vec{k}}$ itself. In general, the averaged $\langle \Delta \rangle$ measured by the injecting current in directional PCARS can reveal any anisotropy present in the system. In the sixth chapter of this thesis, I will discuss one such superconducting system, ZrB_{12}, where directional PCARS revealed anisotropy in both $\Delta_{\vec{k}}$ and H_{c2}.

2.2.5 Our System

There are several techniques to construct point-contact for spectroscopic measurements like needle-anvil [23, 38], break junction [39, 40], shear [41, 42], and the lithographic method [12, 43, 44]. For the PCARS measurements reported in this thesis, a home-built point contact spectroscopy probe [11, 37, 45] was used, which is based on the needle-anvil method (see the schematic in Fig. 2.7). Here, a metal wire in the form of a thin needle creates a contact on the flat surface of another material. The probe we use for PCARS measurement consists of a brass cylinder, a Teflon block, and a sample stage in its lower part. Within the brass cylinder, there is a differential screw, which can be controlled from outside to change the contact size. The cylindrical Teflon block is used as a tip holder. The lowermost part of the probe is the disc-shaped, copper-made sample stage, where the material under study is mounted along with a heater coil (a 50 Ω Nichrome wire) and a temperature sensor (a calibrated Cernox thermometer). For NS junction point contact, the tips that I used were mechanically cut with a slant angle of a 500 micron silver wire so that they had a sharp edge. The cryostat we use for PCARS measurement (and also two-coil mutual inductance measurements) is made by 'American Magnetics, Inc.'. It is equipped with a 3-axis (6T-1T-1T) bottom-loaded, superconducting magnet system, and it consists of two coaxial variable temperature inserts (VTI)

placed inside a liquid He dewar. The probe mounted with the sample is first inserted inside the static VTI, which is then evacuated and filled with exchange gas (helium) to cool the sample area. The static VTI is surrounded by the dynamic VTI, where the temperature can be brought down to 1.4 K by pumping. Controlling the sample temperature with the heater coil at the sample stage is very unstable and difficult. Therefore, we use another heater at the bottom of the dynamic VTI to increase the temperature locally while the exchange gas takes care of the conduction in between. A temperature controller (Lakeshore 350) is used to monitor and control the sample temperature.

2.2.6 Measurement

A lock-in-based modulation technique is used to obtain spectroscopic data, where a dc sweeping current (say I_{dc}) is coupled with a small ac current (say $I_{ac}cos\omega t$). I_{dc} is drawn from a current source (Keithley 6221) and $I_{ac}cos\omega t$ is converted from the output of a digital lock-in amplifier (SR-830, Stanford Research Systems) by a ballast resistor. As the superconducting gap is typically of the order of a few millivolts, the lock-in response is kept on the order of a few microvolts. Ultimately the modulated current is passed through the point contact, and the dc component of the voltage drop across the point contact is measured by a digital multimeter (Keithley 2000) and the ac component is measured by the same lock-in amplifier. As can be seen from Taylor's expansion below, the first harmonic of the input signal is proportional to dV/dI. Hence, to measure the differential resistance (and thereby to calculate the differential conductance), the signal is kept locked at the first harmonic.

$$\begin{aligned} &V(I = I_{dc} + I_{ac}cos\omega t) \\ &\quad = V(I_{dc}) + \left(\frac{dV}{dI}\right)|_{I_{dc}}\ I_{ac}cos\omega t + \frac{1}{4}\left(\frac{d^2V}{dI^2}\right)|_{I_{dc}}\ (I_{ac})^2(1 + cos2\omega t) + \cdots \end{aligned} \tag{2.13}$$

The whole measurement process is completely automated, where the data acquisition is done through the GPIB connection and LabVIEW programs [11].

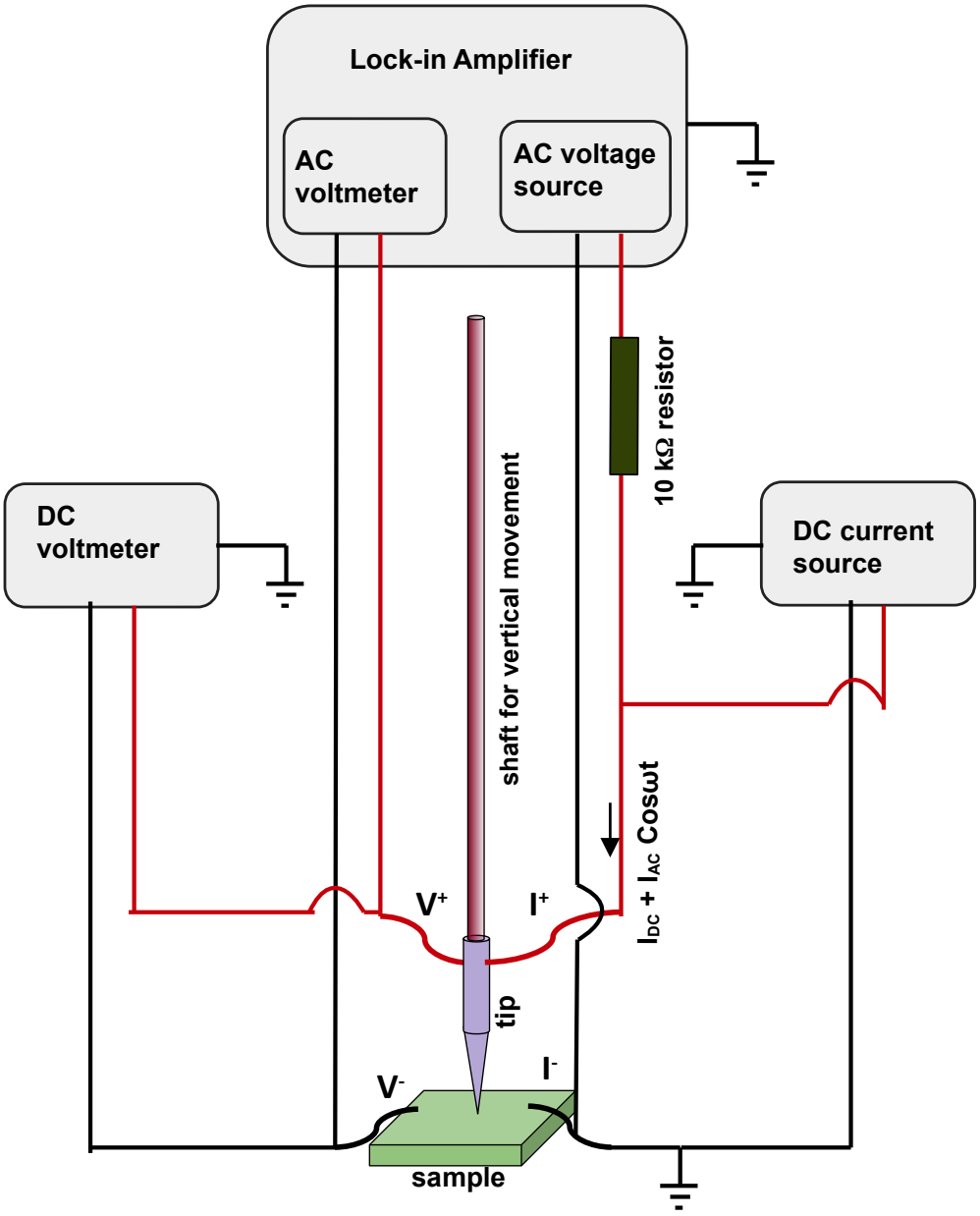

Figure 2.7: A schematic representing the working principle of point contact spectroscopy in our system. The modulation technique of ac and dc current components occasionally varies within different experimental setups.

2.3 Other Experimental Tools Used

The experimental studies in this thesis are primarily based on transport spectroscopic methods such as STS or PCARS. Apart from that, particularly for the project associated with superconducting ZrB_{12} (6th chapter), I have used two-coils mutual inductance measurements to study the temperature and magnetic field (both magnitude and direction) dependence of the ac magnetic susceptibility (χ). Measurements were made using a home-built probe [37] inside the same liquid-helium cryostat used for PCARS measurement. For temperature-dependent experiments, the same static VTI was used where the base temperature we were able to reach (with this particular probe inside) was 1.6 K. The χ measurements are made by sandwiching a sample between two coaxial copper coils (250 micron wire, 300 turns) connected to a lock-in amplifier. One coil is fed with an ac signal (I used 17.33 kHz), and the other one is used as the pick-up coil. For a superconductor, the temperature-dependent χ measured by such a two-coil setup shows a sharp superconducting transition at T_c. It should be noted that the objective of such a measurement is just to identify the transition (and thus to verify the crystal quality at most) and not to characterize the material with the exact value of χ. For such characterization purposes, a more sophisticated measurement technique, such as a vibrating sample magnetometer (VSM), can be useful. In our measurement, neither χ is volume corrected nor the imaginary and real components of χ are separated. The generated emf in the secondary coil provides the necessary information about the χ and it is interpreted with arbitrary units. To investigate the magnetic field dependence, a static magnetic field is applied along the z-axis and increased with a fixed step (I used 50 G). With the increasing magnetic field, a clear shift of the T_c towards lower temperatures is expected. To investigate any magnetic anisotropy, the same experiment can be performed with the field applied along two other directions (x and y axis). To further investigate the anisotropic behavior, thanks to our vector magnet, it is possible to keep the magnitude of the magnetic field fixed but rotate (a complete 2π) the direction of it in a plane ($x-y$, $y-z$, or $z-x$). Using a similar technique, not only the field angle dependence of χ, but also the field angle dependence of ρ is routinely measured (particularly the differential ρ under PCS). In this way, if exists, it is possible to probe the

anisotropy of the Fermi surface of a material.

Acknowledgements

The probe described in this chapter, which is used for PCARS measurements, was designed by former BS-MS project student Jithin B P. The probe which is used for two-coils mutual inductance measurements was designed by former PhD student Mohammad Aslam. The LabVIEW-based programs for data acquisition mentioned were developed by former postdoctoral member of the group, Dr. Sirshendu Gayen. All their contributions are duly acknowledged.

Bibliography

[1] Gerd Binnig, Heinrich Rohrer, Ch. Gerber, and Edmund Weibel. Surface studies by scanning tunneling microscopy. *Physical review letters*, 49(1):57, 1982.

[2] T Hanaguri, S Niitaka, K Kuroki, and H Takagi. Unconventional s-wave superconductivity in Fe(Se,Te). *Science*, 328(5977):474–476, 2010.

[3] Ivar Giaever. Energy gap in superconductors measured by electron tunneling. *Physical Review Letters*, 5(4):147, 1960.

[4] Ivar Giaever. Electron tunneling and superconductivity. *Science*, 183(4131):1253–1258, 1974.

[5] James Nicol, Sidney Shapiro, and Paul H Smith. Direct measurement of the superconducting energy gap. *Physical Review Letters*, 5(10):461, 1960.

[6] John Bardeen. Tunnelling from a many-particle point of view. *Physical Review Letters*, 6(2):57, 1961.

[7] Michael Tinkham. *Introduction to superconductivity*. Courier Corporation, 2004.

[8] RC Dynes, V Narayanamurti, and J Pm Garno. Direct measurement of quasiparticle-lifetime broadening in a strong-coupled superconductor. *Physical Review Letters*, 41(21):1509, 1978.

[9] Matthias Hunstig. Piezoelectric inertia motors-a critical review of history, concepts, design, applications, and perspectives. In *Actuators*, volume 6, page 7. Multidisciplinary Digital Publishing Institute, 2017.

[10] Sirohi Anshu. *Probing Conventional and Unconventional Superconductivity by Ultra-Low-Temperature Scanning Tunneling Spectroscopy.* PhD thesis, Indian Institute of Science Education and Research, Mohali, 2019.

[11] Shekhar Das. *Scanning Tunnelling Microscopy And Transport Spectroscopy On Candidate Topological Systems.* PhD thesis, Indian Institute of Science Education and Research, Mohali, 2019.

[12] Yu G Naidyuk, Jurij G Najdjuk, and IK Yanson. *Point-contact spectroscopy*, volume 145. Springer Science & Business Media, 2005.

[13] Supriyo Datta. *Electronic transport in mesoscopic systems.* Cambridge university press, 1997.

[14] Lucas Janson, Matthew Klein, Heather Lewis, Andrew Lucas, Andrew Marantan, and Katherine Luna. Undergraduate experiment in superconductor point-contact spectroscopy with a Nb/Au junction. *American Journal of Physics*, 80(2):133–140, 2012.

[15] Nickolas Groll, Michael J Pellin, John F Zasadzinksi, and Thomas Proslier. Point contact tunneling spectroscopy apparatus for large scale mapping of surface superconducting properties. *Review of Scientific Instruments*, 86(9):095111, 2015.

[16] F Laube, Gernot Goll, H v Löhneysen, M Fogelström, and F Lichtenberg. Spin-triplet superconductivity in Sr_2RuO_4 probed by andreev reflection. *Physical Review Letters*, 84(7):1595, 2000.

[17] D Daghero and RS Gonnelli. Probing multiband superconductivity by point-contact spectroscopy. *Superconductor Science and Technology*, 23(4):043001, 2010.

[18] Mikael Fogelström, Wan Kyu Park, Laura H Greene, Gernot Goll, and Matthias J Graf. Point-contact spectroscopy in heavy-fermion superconductors. *Physical Review B*, 82(1):014527, 2010.

[19] Dea Daghero, M Tortello, GA Ummarino, J-C Griveau, E Colineau, R Eloirdi, AB Shick, J Kolorenc, AI Lichtenstein, and R Caciuffo. Strong-coupling d-wave superconductivity in $PuCoGa_5$ probed by point-contact spectroscopy. *Nature Communications*, 3(1):1–8, 2012.

[20] RJ Soulen Jr, JM Byers, MS Osofsky, B Nadgorny, T Ambrose, SF Cheng, Pr R Broussard, CT Tanaka, J Nowak, JS Moodera, et al. Measuring the spin polarization of a metal with a superconducting point contact. *Science*, 282(5386):85–88, 1998.

[21] Shashi K Upadhyay, Akilan Palanisami, Richard N Louie, and RA Buhrman. Probing ferromagnets with andreev reflection. *Physical Review Letters*, 81(15):3247, 1998.

[22] II Mazin. How to define and calculate the degree of spin polarization in ferromagnets. *Physical Review Letters*, 83(7):1427, 1999.

[23] AGM Jansen, FM Mueller, and P Wyder. Direct measurement of electron-phonon coupling $\alpha^2F(\omega)$ using point contacts: Noble metals. *Physical Review B*, 16(4):1325, 1977.

[24] Aloysius Gerardus Maria Jansen, AP Van Gelder, and P Wyder. Point-contact spectroscopy in metals. *Journal of Physics C: Solid State Physics*, 13(33):6073, 1980.

[25] G Wexler. The size effect and the non-local boltzmann transport equation in orifice and disk geometry. *Proceedings of the Physical Society (1958-1967)*, 89(4):927, 1966.

[26] BJ Van Wees, H Van Houten, CWJ Beenakker, J Gr Williamson, LP Kouwenhoven, D Van der Marel, and CT Foxon. Quantized conductance of point contacts in a two-dimensional electron gas. *Physical Review Letters*, 60(9):848, 1988.

[27] Jan M van Ruitenbeek. Conductance quantisation in metallic point contacts. In *Metal Clusters at Surfaces*, pages 175–210. Springer, 2000.

[28] VF Gantmakher and Yu V Sharvin. Temperature dependence of the mean free path of electrons in Tin at low temperatures. *Soviet Physics JETP*, 21(4), 1965.

[29] Goutam Sheet, S Mukhopadhyay, and Pratap Raychaudhuri. Role of critical current on the point-contact andreev reflection spectra between a normal metal and a superconductor. *Physical Review B*, 69(13):134507, 2004.

[30] Goutam Sheet. *Point-contact Andreev Reflection Spectroscopy on Superconductors and Ferromagnets*. PhD thesis, Tata Institute of Fundamental Research Mumbai, 2006.

[31] AF Andreev. The thermal conductivity of the intermediate state in superconductors. *Soviet Physics JETP*, 19(5):1228–1231, 1964.

[32] GE Blonder, M Tinkham, and TM Klapwijk. Transition from metallic to tunneling regimes in superconducting micro-constructions: Excess current, charge imbalance, and supercurrent conversion. *Physical Review B*, 25(7):4515, 1982.

[33] A Plecenik, M Grajcar, Š Beňačka, P Seidel, and A Pfuch. Finite-quasiparticle-lifetime effects in the differential conductance of $Bi_2Sr_2CaCu_2O_y$/Au junctions. *Physical Review B*, 49(14):10016, 1994.

[34] RS Gonnelli, D Daghero, GA Ummarino, VA Stepanov, J Jun, SM Kazakov, and J Karpinski. Direct evidence for two-band superconductivity in MgB_2 single crystals from directional point-contact spectroscopy in magnetic fields. *Physical Review Letters*, 89(24):247004, 2002.

[35] P Szabó, Z Pribulová, G Pristáš, SL Bud'ko, PC Canfield, and P Samuely. Evidence for two-gap superconductivity in $Ba_{0\cdot 55}K_{0\cdot 45}Fe_2As_2$ from directional point-contact andreev-reflection spectroscopy. *Physical Review B*, 79(1):012503, 2009.

[36] Dario Daghero, Mauro Tortello, GA Ummarino, and RS Gonnelli. Directional point-contact andreev-reflection spectroscopy of Fe-based superconductors:

Fermi surface topology, gap symmetry, and electron-boson interaction. *Reports on Progress in Physics*, 74(12):124509, 2011.

[37] Mohammad Aslam. *Investigation of Superconductivity and other Competing Orders in BiS_2-Based Systems*. PhD thesis, Indian Institute of Science Education and Research, Mohali, 2018.

[38] P Szabó, P Samuely, J Kačmarčík, Thierry Klein, J Marcus, Daniel Fruchart, Salvatore Miraglia, C Marcenat, and AGM Jansen. Evidence for two superconducting energy gaps in MgB_2 by point-contact spectroscopy. *Physical Review Letters*, 87(13):137005, 2001.

[39] K Flachbart, K Gloos, E Konovalova, Y Paderno, M Reiffers, P Samuely, and P Švec. Energy gap of intermediate-valent SmB_6 studied by point-contact spectroscopy. *Physical Review B*, 64(8):085104, 2001.

[40] Tobias Böhler, Achim Edtbauer, and Elke Scheer. Point-contact spectroscopy on Aluminium atomic-size contacts: longitudinal and transverse vibronic excitations. *New Journal of Physics*, 11(1):013036, 2009.

[41] PN Chubov, IK Yanson, and AI Akimenko. Electron-phonon interaction in Aluminum point contacts. *Fizika Nizkikh Temperatur*, 8(1):64–80, 1982.

[42] IK Yanson, LF Rybal'chenko, NL Bobrov, and VV Fisun. Point-contact spectroscopy of superconductors in the nonequilibrium state. *arXiv preprint arXiv:1512.00684*, 2015.

[43] KS Ralls, RA Buhrman, and RC Tiberio. Fabrication of thin-film metal nanobridges. *Applied Physics Letters*, 55(23):2459–2461, 1989.

[44] MD Jaeger, V Tsoi, and B Golding. Lithographic point contacts for transverse electron focusing in Bismuth. *Applied Physics Letters*, 68(9):1282–1284, 1996.

[45] Suman Kamboj. *Transport spectroscopy on novel quantum materials*. PhD thesis, Indian Institute of Science Education and Research, Mohali, 2020.

Chapter 3

Multiband Superconductivity in AuBe

In this chapter, the superconducting nature of chiral, non-centrosymmetric AuBe is investigated. From the direct measurement of the superconducting gap through tunneling experiments, a clear signature of multiband superconductivity is reported in this material. The work presented in this chapter is already published in Ref. [1].

3.1 Introduction

The characteristics of non-centrosymmetric superconductors (NCSCs) vary greatly from material to material. Several NCSCs have evidence of line nodes in the superconducting gap, including Mo_3Al_2C [2], $CeIrSi_3$ [3], $CePt_3Si$ [4, 5], Li_2Pt_3B [6, 7], and recently Ru_7B_3 [8]. In addition, in some NCSCs, only conventional, isotropic, *s*-wave, fully-gapped superconducting phase was reported. A few examples includes $Nb_{0.18}Re_{0.82}$ [9], BiPd [10, 11], T_2Ga_9 (T = Rh, Ir) [12, 13] and $LaMSi_3$ (M = Rh [14], Ir [15], and Pd, Pt [16]). However, for some, the superconducting phase can be described neither by a fully open gap nor a nodal gap opened in a single band and a multigap model becomes necessary. $LaNiC_2$ [17], $TaRh_2B_2$ [18], Re_6Zr [19], and Ln_2C_3 (Ln = La,Y) [20, 21] are examples of such NCSCs. AuBe with a $T_c \sim 3.25$ K [22–27] is important in this context for a variety of reasons.

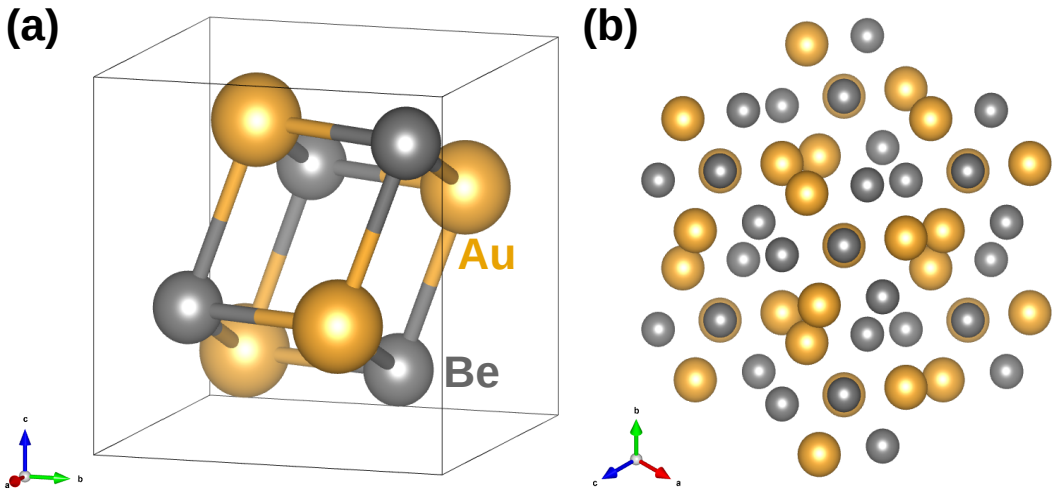

Figure 3.1: The crystal structure of superconducting AuBe. **(a)** One unit cell and **(b)** a view parallel to [111] direction along which both mirror and inversion symmetries are broken.

In Fig. 3.1, the crystal structure of superconducting AuBe is presented [28, 29]. The material comprises the heavy metal Au and has a non-centrosymmetric crystal structure (cubic space group symmetry of $P2_13$) [23, 24]. As a result, AuBe could be a candidate for a mixed pairing state [5, 6, 8]. Furthermore, the crystal structure of AuBe is chiral ($B20$, FeSi type), and chiral fermions are predicted to be present in such a structure [30–32]. It's worth noting that the $B20$ structure is the only known crystal structure with bulk magnetic skyrmions [33–35]. In addition, a recent study found that the superconducting pairing of AuBe comes from multiple energy bands [36, 37]. All of these factors combine to make AuBe an appealing system for searching for unusual superconducting pairings and exotic quasiparticle excitations.

3.1.1 Outstanding Issues

Considering the previous reports on superconducting AuBe, there are two major unresolved issues. The first one is related to the type of superconductivity with respect to the magnetic properties. Based on their independent dc magnetization,

specific heat, and muon-spin rotation/relaxation (μSR) studies, Amon *et al.* [24] reported type-II (with Ginzburg-Landau parameter $k_{GL} = 2.3$) superconductivity, while Singh *et al.* [25] and Beare *et al.* [26] reported type-I ($k_{GL} = 0.4$) behaviour in AuBe. Based on their resistivity, dc magnetization, ac susceptibility, and specific heat studies, Reber *et al.* [23, 27] attempted to resolve the issue, arguing about a crossover from type-II to type-I superconductivity [38, 39] at $\sim$ 1.2 K. This suggests the likelihood that AuBe belongs to the type-II/I superconductor class, whose behaviour has been studied in purposefully disordered elemental superconductors with $k_{GL} \sim 1/\sqrt{2}$ [40, 41] for a long time. Such a crossover has recently been hypothesised in superconductors with non-centrosymmetric crystal structures and/or numerous superconducting bands [42, 43]. Both of these features are, by chance, significant in the current context of AuBe. The second issue is the description of the superconducting order parameter. All findings published up to 2019, including those with mutually contradictory conclusions about the type (type-I vs. type-II) of superconductivity agree that AuBe is a pure, isotropic *s*-wave, spin-singlet superconductor [24–27]. Khasanov *et al.* [36, 37], on the other hand, in their two successive papers in 2020, suggested an entirely new unconventional multi-gap mechanism in AuBe. Based on fresh μSR experiments [36], the authors indicated that the temperature evolution of the thermodynamic critical field B_c of AuBe could not be described without assuming at least two separate gaps. The $2\Delta/k_BT_c$ values were found to be 4.52 and 2.37, respectively, using a self-consistent two-gap model. Furthermore, the superiority of the self-consistent two-gap model over the usual single gap model was determined based on a detailed comparative analysis [37]. As a result, measuring the superconducting gap(s) spectroscopically in AuBe remains an important challenge in order to obtain conclusive proof of multiband superconductivity or to rule out such a possibility. To investigate the nature of the gaps, thorough measurements of the temperature and magnetic field evolution of the superconducting order parameter are also required.

3.2 Experimental Techniques

The polycrystalline sample of AuBe was prepared by arc melting method from a stoichiometric mixture of elemental Au and Be. The preparation and charac-

terization details were reported in Ref. [25]. To directly probe the superconducting gap(s) in AuBe, we employed low-temperature scanning tunneling microscopy (STM) and spectroscopy (STS) in our *Unisoku* system with *RHK R9* controller, inside the ultra-high vacuum (UHV) cryostat kept at $\sim 10^{-10}$ mbar. The lowest temperature down to which the measurements were performed was 310 mK. As such experiments are extremely sensitive to the surface cleanliness, a few layers from the surface were first removed by mild reverse sputtering in an argon environment *in-situ*, inside the UHV preparation chamber that is connected to the main STM/S chamber. Then the sample with its pristine surface was transferred to the scanning stage at low temperature for experiments. The Tungsten (W) tip, which was prepared outside by electrochemical etching, was also cleaned by high-energy electron-beam bombardment inside the same UHV preparation chamber. Spectra were further recorded at random points on the surface, and at each point on the sample surface, we found a clean spectrum with a fully opened gap. The differential conductance dI/dV was measured using a lock-in based ac modulation technique (amplitude 40 μV, frequency 3 kHz).

3.3 Results and Discussions

3.3.1 STS Spectra

All the spectra we probed show two clear peaks symmetric about $V = 0$. The position of these coherence peaks provides a direct measure of the superconducting energy gap (Δ). However, depending on the different points on the sample surface probed, the positions of the coherence peaks vary from ± 250 μV to ± 375 μV, approximately. In Fig. 3.2, we show six representative tunneling spectra captured at different points on the surface of AuBe, all at the lowest temperature. The spectra presented in Fig. 3.2(a)-(c) visually have a wider spectral gap compared to the spectra presented in Fig. 3.2(d)-(f). Intrinsic disorders on the surface of the sample can exhibit such variation, and that was indeed our primary guess. Nevertheless, to extract the exact value of the order parameter Δ for each spectrum, we proceeded further with the analysis.

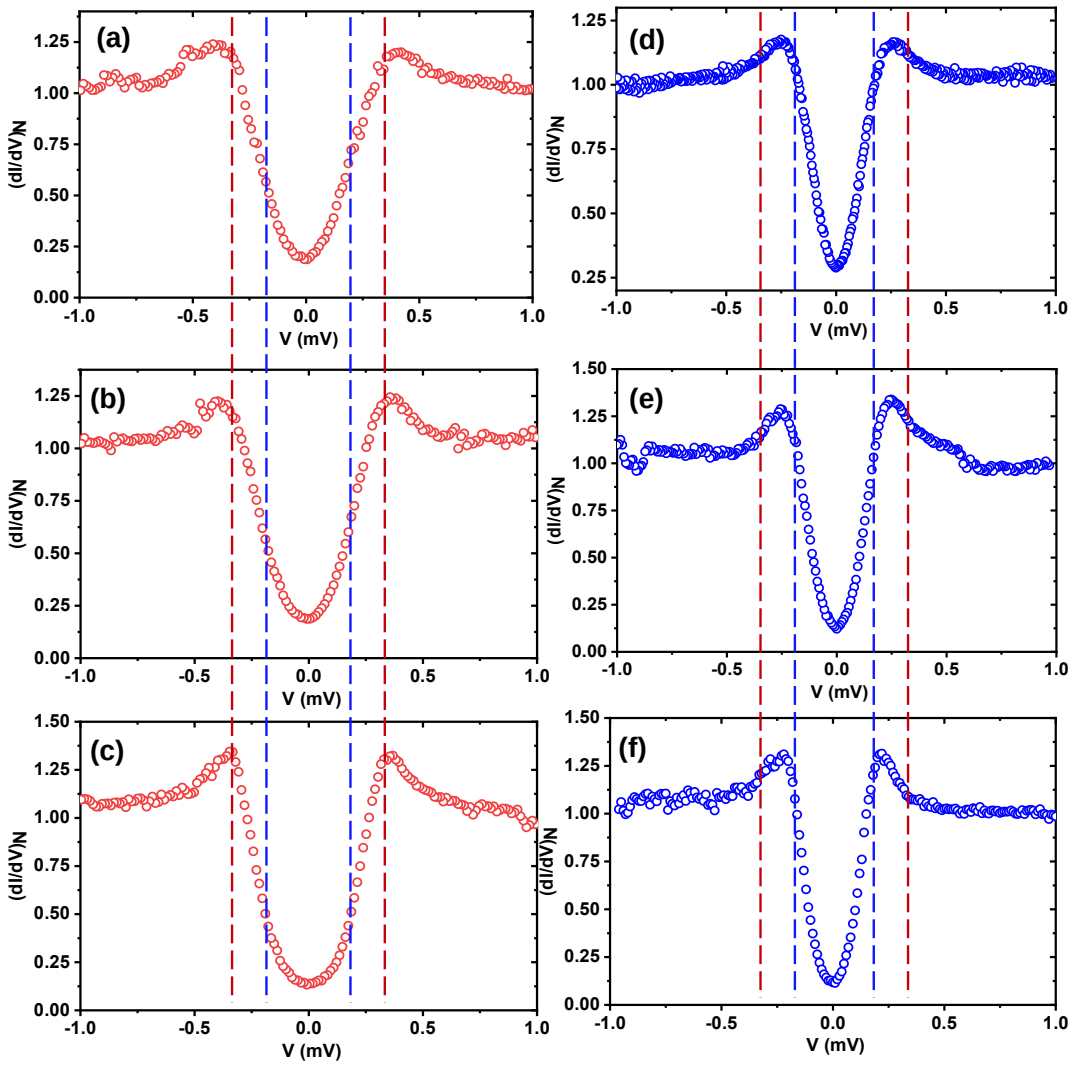

Figure 3.2: Six representative tunneling spectra probed at different points on the surface of AuBe, all recorded at $T \sim 310$ mK. The spectra (red circles) represented in **(a)-(c)** have visually larger gap, and those represented in **(d)-(f)** have visually smaller gap. The verticle lines are guide to the eye and correspond to the biasing of ± 320 μV (red) and ± 180 μV (blue), respectively.

3.3.2 Analysis Under Single-gap Model

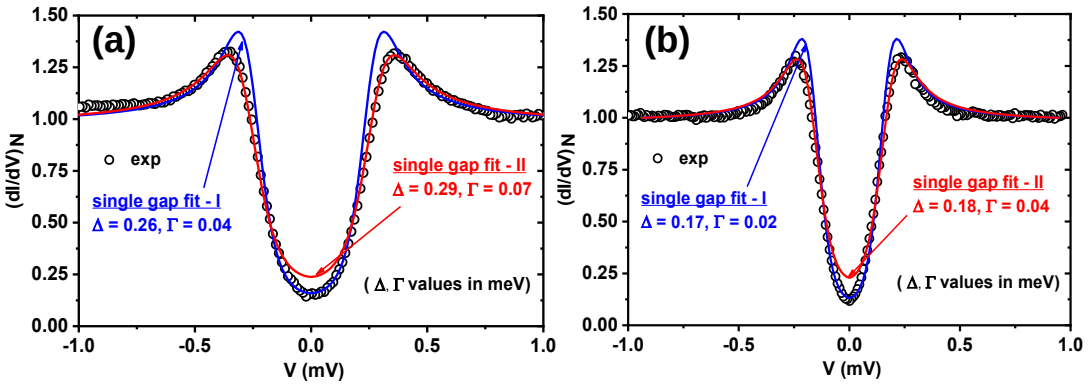

Figure 3.3: Inefficiency of the single-gap s-wave model to fit typical AuBe spectra of both types. Red lines match the upper part only while the blue lines match the lower part.

All spectra were first normalized $w.r.t$ conductance at 1.5 mV, where they are almost flat. Then these experimental spectra were compared with numerically generated spectra using the expression for the tunneling current within a single-gap model given by the following equation.

$$I(V) \propto \int_{-\infty}^{+\infty} N_s(E) N_n(E - eV)[f(E) - f(E - eV)]dE \tag{3.1}$$

Here, $N_s(E)$ and $N_n(E)$ are, respectively, the normalized density of states (DOS) of the superconducting sample and the normal metallic tip, and $f(E)$ is the Fermi-Dirac distribution function [44]. Within this single-band model, N_s is given by the following expression of the Dynes formula [45].

$$N_s(E) \propto Re\left(\frac{(E - i\Gamma)}{\sqrt{(E - i\Gamma)^2 - \Delta^2}}\right) \tag{3.2}$$

In our analysis, Γ takes care of all possible reasons for spectral broadening, including that due to finite quasiparticle lifetime and other possible interband and intraband scattering effects. Although this model is routinely used and highly successful to analyze the tunneling spectroscopic data of a conventional supercon-

ductor, it fails to match any experimental spectrum of AuBe, regardless of whether the spectrum was visibly wider (like in Fig. 3.2(a)-(c)) or narrower (like in Fig. 3.2(d)-(f)). To explain the issue, two such theoretical plots (red and blue curves) are shown over each experimental spectrum (black circles) presented in Fig. 3.3(a) and (b). The red line represents the closest match for the upper portions of each spectrum, especially at the coherence peaks. However, that fails to match the lower portion near $V = 0$, underestimating the actual depth of the spectrum. Since Γ is fixed arbitrarily without a complete knowledge about the microscopic origin of the same, we first tried to fit the spectra by brute force making Γ free. In order to match the lower part, if we tune the parameter Γ down and adjust the Δ as needed too, we face a situation (blue line) where the lower part of the theoretical plot matches perfectly with the experimental spectrum, but now deviates significantly above and overestimates the actual height of the coherence peaks. Hence, it becomes clear that although the quasiparticle excitation spectrum of AuBe looks like a standard one with a pair of clear coherence peaks, it cannot be explained within the framework of a single-gap s-wave model. Considering the higher order symmetry in Δ also does not rescue us from this situation (see Appendix 3.A for details). Hence, we considered the simplest two-gap model for our spectra, which was further motivated by the facts about AuBe reported in the past. The following is a description of such facts.

3.3.3 Indications of Multiband Superconductivity

First, based on the de Haas–van Alphen experiments performed on AuBe, the presence of multiple bands crossing the Fermi level was reported by Rebar *et al*. [23, 27]. Second, based on density functional theory (DFT) and band structure calculations performed independently by Rebar *et al*. [23, 27] and Amon *et al*. [24] such band crossing was confirmed for at least three conductive bands. However, although this special type of band structure creates a possibility of multiband superconductivity in AuBe, it can not be taken as an evidence of the same. We also noted the reports by Khasanov *et al*. [36, 37], where the authors extracted the thermodynamic critical field B_c from their μSR experiment on AuBe and explained its temperature dependence based on a self-consistent two-gap model.

3.3.4 Analysis Under Two-gap Model

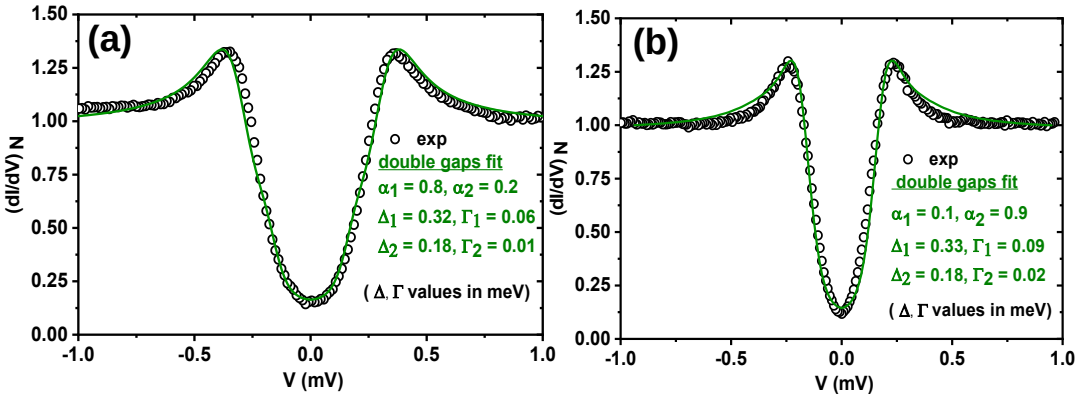

Figure 3.4: Success of a simple two-gap s-wave model to fit the both spectra presented in Fig. 3.3.

In such a scenario, the quasiparticle excitation spectrum for a two-band superconductor can be determined simply by adding the two single-gap BCS spectra for the two respective bands [46]. Considering such a picture, the quasiparticle DOS of the j-th band can be written as follows.

$$N_{s,j}(E) = N_j(E_F) Re\left(\frac{(E - i\Gamma_j)}{\sqrt{(E - i\Gamma_j)^2 - \Delta_{0j}^2}}\right), j = 1, 2 \tag{3.3}$$

Here j is the band index, $N_j(E_F)$ is the normal state DOS at the Fermi level corresponding to the jth band, and Δ_{0j} is the amplitude of the superconducting energy gap formed in the jth band. The tunneling current, which has contributions from both bands, will now take the following form.

$$I(V) \propto \sum_{j=1,2} \alpha_j \int_{-\infty}^{+\infty} N_{sj}(E) N_n(E - eV)[f(E) - f(E - eV)]dE \tag{3.4}$$

Here, α_j is the relative contribution of the j-th band to the tunneling current. When we tried to fit the spectra using this model, it became extremely successful over the entire energy range. We have presented such theoretical plots with green

lines in Fig. 3.4(a) and (b). It is clear that such a plot matches both the upper and lower part of each spectrum, this time very well. The extracted values of two superconducting gaps (Δ_1 and Δ_2) and the corresponding two broadening parameters (Γ_1 and Γ_2) are also mentioned for each spectrum. To note, the pair of superconducting gap values did not vary noticeably from $\Delta_1 \simeq 320\pm10$ μeV, and $\Delta_2 \simeq 180\pm10$ μeV across the spectra. The parameters which actually do vary are the relative contributions of each band to the total tunneling current, i.e, α_1 and α_2. For the spectra represented in Fig. 3.2(a)-(c), we found $\alpha_1 > \alpha_2$, and for the spectra represented in Fig. 3.2(d)-(f), the opposite.

3.3.5 Comparison with MgB_2

In MgB_2, the two gaps are distinctly visible from experiments like Andreev reflection spectroscopy, tunneling spectroscopy, etc. [47–52]. In such experiments, two pairs of coherence peaks corresponding to the two gaps appear in the quasiparticle DOS. In contrast, the spectra that we recorded on AuBe do not have distinct multigap features, and visually they look like a single-gap BCS spectrum. However, from our detailed analysis, we found that a usual single-band model cannot explain such spectra, while a simple two-gap model can. Visually, the spectra of AuBe appear different from those of MgB_2, primarily because the amplitudes of the two gaps in AuBe are close. Schopohl *et al.* [53] and Noat *et al.* [54] explained such situations with interband scattering and tunneling of quasiparticles. They described multiple characteristic features of the multiband spectra, like damped quasiparticle peaks, kinks near the peaks, dips beyond the peaks, etc., that may appear as a consequence of such interband physics. From a close visual inspection of our spectra, when we compare the experimental data (black circles) with the best single gap fits (blue lines) in Fig. 3.3(a) and (b), we actually can notice the first two features mentioned above. However, it is important to note that a simple multigap model proposed by Suhl *et al.* [46] is successful in fitting (green lines) our experimental data with very high fidelity, and in this model, more complicated factors like interband scattering, k-selective tunneling, etc. were not taken into account. To note, when Iavarone *et al.* [50] reported distinct two-gap superconductivity in MgB_2 by tunneling spectroscopy, at the same time Eskildsen

et al. [55] also reported tunneling spectroscopy on that material. Interestingly, when the latter group attempted to explain their spectra using the usual single gap Dynes equation, their theoretical fit overestimated the coherence peak. This can be compared with our fittings (blue lines) in Fig. 3.3(a) and (b) using the single gap Dynes model. Now, we also note that the existence of two gaps cannot be proved simply based on the analysis of certain spectra. If two different bands participate in the superconductivity of AuBe, they are expected to evolve with temperature and external magnetic field independently and differently unless the interband scattering is too strong.

3.3.6 Temperature Dependence of Spectra

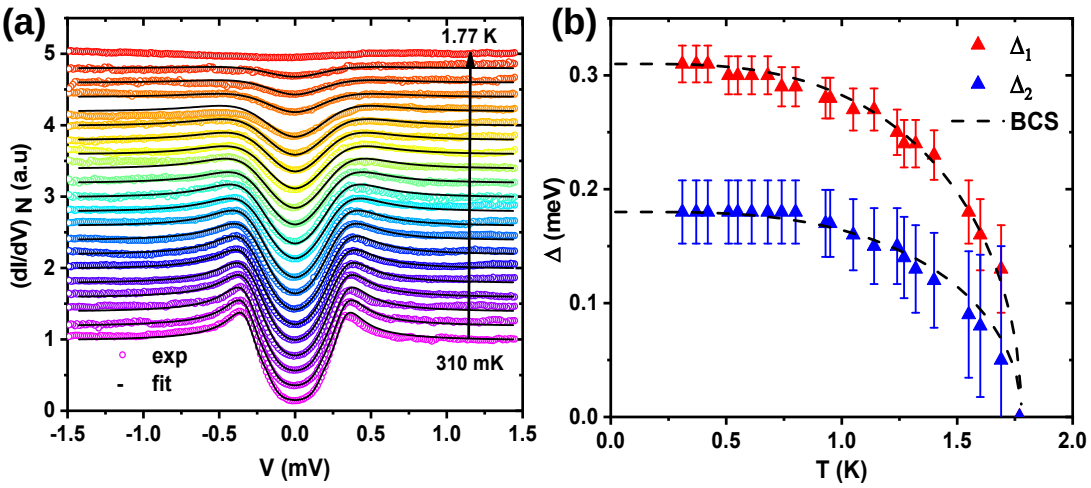

Figure 3.5: **(a)** The temperature dependence of typical tunneling conductance spectra of AuBe with the theoretical fits. At the lowest T, Δ_1=310 μeV, Δ_2=180 μeV, Γ_1=50 μeV, Γ_2=15 μeV for the spectrum. The relative contributions α_1=0.8 and α_2=0.2 remain constant throughout the T range. **(b)** Evolution of the two gaps (Δ_1 and Δ_2) with T, extracted from plot (a) along with their individual BCS fits.

The temperature (T) dependence of a typical spectrum is presented in Fig. 3.5(a), where the coloured circles represent the experimentally obtained spectra. With increasing T, the coherence peaks gradually decrease, and all the gap features disappear at 1.77 K. The corresponding theoretical fits within the two-band model

[46] are shown on top of each experimental spectrum as black lines where the values of $\alpha_1(0.8)$ and $\alpha_2(0.2)$ were kept unchanged over the entire T range. The two gaps extracted from the fits are plotted with T in Fig. 3.5(b) with red (Δ_1) and blue (Δ_2) triangles. Each gap independently follows a BCS-like dependence [44] up to 1.77 K, where they merge and disappear. The smaller gap (Δ_2) slightly deviates from the BCS-line at higher T, which is typical in the presence of a small but non-zero inter-band scattering [46]. Such a situation, where two gaps independently evolve with temperature until they disappear at the same T_c, is valid for a multi-gap superconductor where interband scattering is negligible. This further validates the model we have used for our analysis. From our two-gap analysis of the tunneling spectra, we found that $2\Delta_1/k_BT_c = 4.37$ and $2\Delta_2/k_BT_c = 2.46$, respectively. The former one is slightly underestimated, while the latter one is slightly overestimated compared to the values 4.52 and 2.37, respectively, as was reported by Khasanov *et al.* based on μSR experiments [36]. In the presence of a very small yet finite interband scattering, these differences are in accordance with the two-gap model [46].

3.3.7 Magnetic Field Dependence of Spectra

To gain further information about the pairing mechanism, we now focus on the magnetic-field dependence of the spectra. The colored circles in Fig. 3.6(a) show the experimentally obtained spectra, all measured at 310 mK, and the black lines represent the corresponding two-band fits. All superconducting features, including the coherence peaks, disappear at 17 kG. The evolution of the extracted two gaps (larger Δ_1 and smaller Δ_2) with magnetic field are shown in Fig. 3.6(b). Up to 10 kG, both gaps tend to decrease slowly in a linear fashion, and beyond that, they decrease faster until becoming zero at 17 kG. Two important conclusions can be drawn from this observation. First, the gradual transition supports the type-II behaviour in AuBe as reported by Amon *et al.* [24] but contradicts the type-I behaviour reported by Singh *et al.* [25] and Beare *et al.* [26]. However, this contradiction can be easily resolved considering the proposed type-II/I superconductivity by Reber *et al.* [27]. As our magnetic measurements are performed at $\sim$ 310 mK, which is far below the reported crossover point 1.2 K [23, 27], the

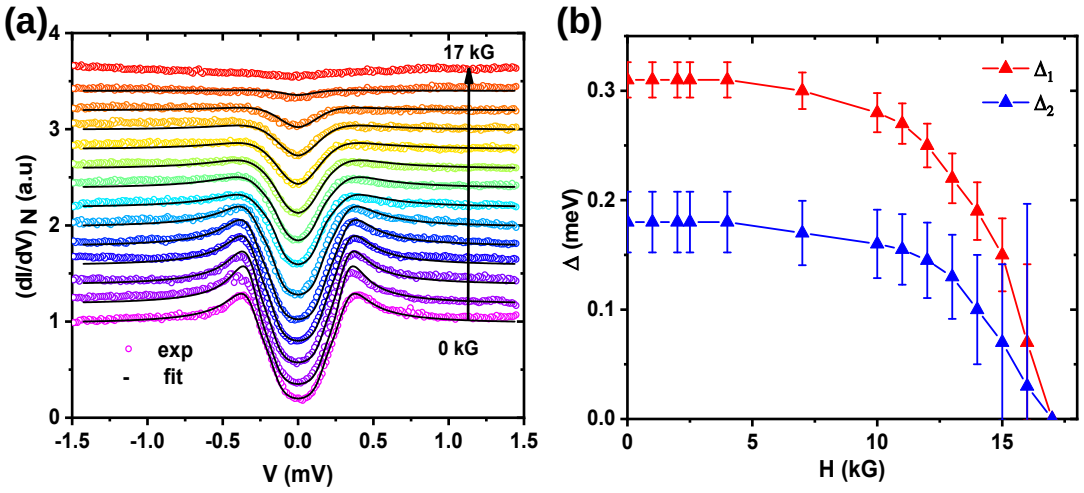

Figure 3.6: **(a)** Magnetic field dependence of tunneling conductance spectra of AuBe, recorded and kept throughout at $T = 310$ mK, and corresponding theoretical fits. **(b)** Evolution of Δ_1 and Δ_2 with the magnetic field extracted from the plot (a). The same spectrum is used for T and H dependence keeping the position of the tip unchanged on the sample surface.

type-II behavior is normal and visible. On the second note, the reported critical field H_c of AuBe from various bulk measurements varies between 259 G to 335 G [24–27, 36], but from our magnetic field dependence, we found the local critical field $H_{c(l)}$ as high as 17 kG. It is interesting to note that Reber *et al.* [27] also reported a considerably higher resistive upper critical field $H_{c(\rho)}$ compared to the thermodynamic upper critical field H_c found from heat capacity and magnetization measurements. To explain this enhancement, the authors have eliminated the possibility of defects or impurity phases at the surface and concluded it to be an intrinsic surface behavior with a possible topological protection. However, based on our data, such a possibility can be neither confirmed nor ruled out. As we will see in the next chapter, such high $H_{c(l)}$ compared to H_c is not unusual for a superconductor. Particularly for multi-band superconductors, such observation can have an interesting explanation (see Section 4.C in the appendix of the next chapter for more details).

3.4 Band Structure and Fermi Surface

The band dispersion relation and the Fermi surface topology of AuBe were reported independently twice before [23, 24]. Band crossings were confirmed both by DFT calculations and de Haas-van Alphen studies on this material. However, as the multiband mechanism in AuBe was not known at that time, we decided to perform some fresh first-principles electronic structure calculations in light of our experimental findings. Ab-initio electronic structure of AuBe was calculated using the Density Functional Theory (DFT) [56] implemented in Quantum Espresso [57]. The calculated band structure and the topology of the Fermi surfaces are consistent with the previous reports [24, 27]. In our calculations, the experimental crystal structure was used with a relaxed cell parameter of 0.4709 nm. A full-relativistic pseudo-potential with Perdew-Burke-Ernzerof (PBE) [58] exchange-correlation potential was used in the projected augmented wave (PAW) [59] method, both with and without spin-orbit coupling (SOC). Self-consistent charge-density convergence was achieved on a $10 \times 10 \times 10$ Monkhorst-Pack [60] k-grid. The energy cut-off for the calculation is 60 Ry and the Fermi-surfaces and Fermi-velocities reported here were obtained on a k-grid of $20 \times 20 \times 20$ without the SOC.

In Fig. 3.7(a) and (b), the two major Fermi surface pockets of AuBe are plotted, where the corresponding Fermi velocity is shown with colour gradients. For visual clarity, SOC is not considered in these plots, which would otherwise slightly double the surfaces due to band splitting. The band dispersion along the high symmetry directions and the orbital projected DOS are plotted in Fig. 3.7(c) and (d), respectively. The corresponding high symmetry points within the first Brillouin zone are represented in the inset of Fig. 3.7(d). From the DOS, it is evident that there are significant contributions from Be p-orbitals, followed by Au p-orbital and so on. Be atoms are significantly light in weight compared to Au atoms. As Be p-orbital has a dominant contribution to the Fermi surface, it is logical to assume that the superconductivity in AuBe is associated with the phonon modes of these light atoms. It can be also verified from Fig. 3.7(c) that the band splittings due to SOC are negligibly small for the bands crossing near Γ and M-point. All these indicate relatively weak interaction effects and consequently a

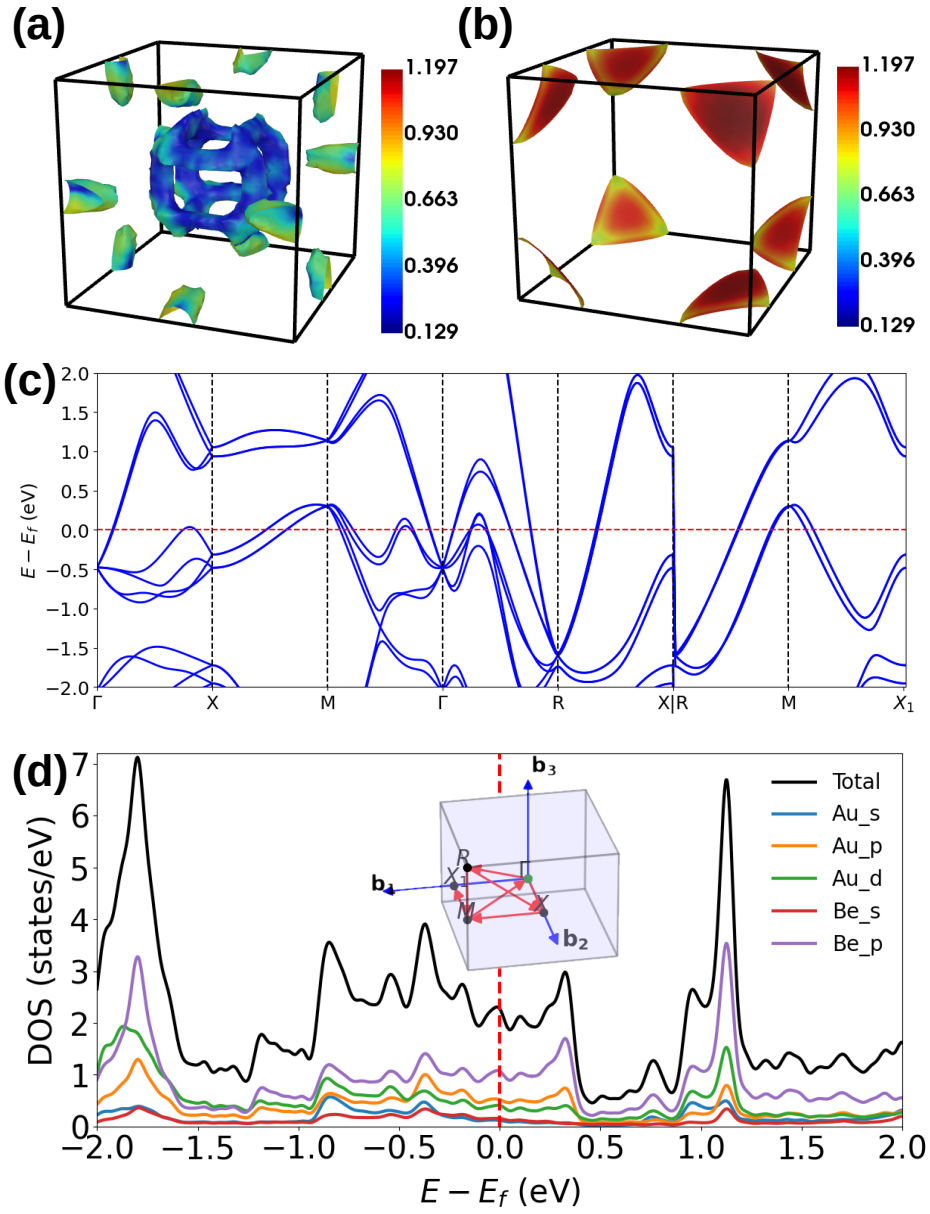

Figure 3.7: **(a)** and **(b)** Two representative Fermi surface pockets of AuBe with the Fermi velocities represented with colour gradients in arbitrary unit. **(c)** The band dispersion along the high symmetry directions, where band split is visible due to moderate spin-orbit coupling. **(d)** total and orbital-resolved DOS considering the spin-orbit coupling. *Inset*: the high symmetry paths joining the high symmetry points within the first Brillouin zone of simple-cubic shape.

phonon-mediated BCS type superconductivity in AuBe. This may also explain why even being a non-centrosymmetric superconductor, AuBe does not reveal a mixed pairing state. The large electron pocket at the Γ-point represented in Fig. 3.7(a) has significantly less Fermi velocity and large DOS. On the other hand, the DOS of the hole pocket at the M-point represented in Fig. 3.7(b) is significantly less, while the Fermi velocity is relatively larger. Therefore, it is rational to conclude that the pocket at the Γ-point leads to the larger superconducting gap ($\Delta_1 \simeq 320\pm10$ μeV) while that at the M-point causes the smaller one ($\Delta_2 \simeq 180\pm10$ μeV).

3.5 Summary

In conclusion, I have given a comprehensive scanning tunneling spectroscopic study of non-centrosymmetric AuBe. We found that a single-band model fails to explain the quasiparticle excitation data, but a simple two-band model can. Our two-gap analysis of tunneling spectra revealed that $2\Delta_1/k_BT_c = 4.37$ and $2\Delta_2/k_BT_c = 2.46$ for the two bands, respectively. These values match with prior reports [36, 37]. At sub-Kelvin temperatures, our magnetic field-dependent data support type-II behavior and indicate the persistence of a finite local spectral gap much above the bulk critical field of AuBe. Our electronic band structure calculations, which also agree with previous reports [24, 27], suggest that this material has phonon-mediated BCS type superconductivity. We hypothesize based on our Fermi surface study that the electron pocket at the Γ-point causes the larger superconducting gap, while the hole pocket at the M-point causes the smaller one.

Acknowledgements

The STM spectroscopic data acquisition was done by Aastha Vasdev with my active participation in the process. Kapil Motla, Anshu Kataria, and Dr. Ravi Prakash Singh from IISER Bhopal synthesized the polycrystaline sample. The first principles calculations mentioned in this chapter were performed by Partha Sarathi Rana and Dr. Tanmoy Das from IISc, Bangalore. The contributions from all these people are duly acknowledged for this project.

Bibliography

[1] Soumya Datta, Aastha Vasdev, Partha Sarathi Rana, Kapil Motla, Anshu Kataria, Ravi Prakash Singh, Tanmoy Das, and Goutam Sheet. Spectroscopic evidence of multigap superconductivity in noncentrosymmetric AuBe. *Physical Review B*, 105(10):104505, 2022.

[2] E Bauer, G Rogl, Xing-Qiu Chen, RT Khan, H Michor, G Hilscher, E Royanian, K Kumagai, DZ Li, YY Li, et al. Unconventional superconducting phase in the weakly correlated noncentrosymmetric Mo_3Al_2C compound. *Physical Review B*, 82(6):064511, 2010.

[3] H Mukuda, T Fujii, T Ohara, A Harada, M Yashima, Y Kitaoka, Y Okuda, R Settai, and Y Onuki. Enhancement of superconducting transition temperature due to the strong antiferromagnetic spin fluctuations in the noncentrosymmetric heavy-fermion superconductor $CeIrSi_3$: A Si 29 NMR study under pressure. *Physical Review Letters*, 100(10):107003, 2008.

[4] Ismardo Bonalde, Werner Brämer-Escamilla, and Ernst Bauer. Evidence for line nodes in the superconducting energy gap of noncentrosymmetric $CePt_3Si$ from magnetic penetration depth measurements. *Physical Review Letters*, 94(20):207002, 2005.

[5] PA Frigeri, DF Agterberg, A Koga, and M Sigrist. Superconductivity without inversion symmetry: MnSi versus $CePt_3Si$. *Physical Review Letters*, 92(9):097001, 2004.

[6] HQ Yuan, DF Agterberg, N Hayashi, P Badica, D Vandervelde, K Togano, M Sigrist, and MB Salamon. s-wave spin-triplet order in superconductors

without inversion symmetry: Li_2Pd_3B and Li_2Pt_3B. *Physical Review Letters*, 97(1):017006, 2006.

[7] M Nishiyama, Y Inada, and Guo-qing Zheng. Spin triplet superconducting state due to broken inversion symmetry in Li_2Pt_3B. *Physical Review Letters*, 98(4):047002, 2007.

[8] Soumya Datta, Aastha Vasdev, Ranjani Ramachandran, Soumyadip Halder, Kapil Motla, Anshu Kataria, Rajeswari Roy Chowdhury, Ravi Prakash Singh, Goutam Sheet, et al. Spectroscopic evidence of mixed angular momentum symmetry in non-centrosymmetric Ru_7B_3. *Scientific Reports*, 11(1):1–7, 2021.

[9] Amar B Karki, Yimin M Xiong, Neel Haldolaarachchige, Shane Stadler, Ilya Vekhter, Philip W Adams, DP Young, WA Phelan, and Julia Y Chan. Physical properties of the noncentrosymmetric superconductor $Nb_{0\cdot 18}Re_{0\cdot 82}$. *Physical Review B*, 83(14):144525, 2011.

[10] Zhixiang Sun, Mostafa Enayat, Ana Maldonado, Calum Lithgow, Ed Yelland, Darren C Peets, Alexander Yaresko, Andreas P Schnyder, and Peter Wahl. Dirac surface states and nature of superconductivity in noncentrosymmetric BiPd. *Nature Communications*, 6(1):1–6, 2015.

[11] XB Yan, Yang Xu, LP He, JK Dong, Hwanbeom Cho, Darren C Peets, Je-Geun Park, and SY Li. Nodeless superconductivity in the noncentrosymmetric superconductor BiPd. *Superconductor Science and Technology*, 29(6):065001, 2016.

[12] Takeshi Shibayama, Minoru Nohara, Hiroko Aruga Katori, Yoshihiko Okamoto, Zenji Hiroi, and Hidenori Takagi. Superconductivity in Rh_2Ga_9 and Ir_2Ga_9 without inversion symmetry. *Journal of the Physical Society of Japan*, 76(7):073708–073708, 2007.

[13] Kouhei Wakui, Satoshi Akutagawa, Naoki Kase, Kenji Kawashima, Takahiro Muranaka, Yasufumi Iwahori, Jiro Abe, and Jun Akimitsu. Thermodynamic properties of the non-centrosymmetric type-I superconductor Rh_2Ga_9 and Ir_2Ga_9. *Journal of the Physical Society of Japan*, 78(3):034710–034710, 2009.

[14] VK Anand, AD Hillier, DT Adroja, AM Strydom, H Michor, KA McEwen, and BD Rainford. Specific heat and μSR study on the noncentrosymmetric superconductor $LaRhSi_3$. *Physical Review B*, 83(6):064522, 2011.

[15] V Kn Anand, D Britz, A Bhattacharyya, DT Adroja, AD Hillier, AM Strydom, W Kockelmann, BD Rainford, and Kn A McEwen. Physical properties of noncentrosymmetric superconductor $LaIrSi_3$: A μ sr study. *Physical Review B*, 90(1):014513, 2014.

[16] M Smidman, AD Hillier, DT Adroja, MR Lees, V Kn Anand, Ravi P Singh, RI Smith, DM Paul, and G Balakrishnan. Investigations of the superconducting states of noncentrosymmetric $LaPdSi_3$ and $LaPtSi_3$. *Physical Review B*, 89(9):094509, 2014.

[17] J Chen, L Jiao, JL Zhang, Y Chen, L Yang, M Nicklas, F Steglich, and HQ Yuan. Evidence for two-gap superconductivity in the noncentrosymmetric compound $LaNiC_2$. *New Journal of Physics*, 15(5):053005, 2013.

[18] DA Mayoh, AD Hillier, K Götze, D McK Paul, G Balakrishnan, and MR Lees. Multigap superconductivity in chiral noncentrosymmetric $TaRh_2B_2$. *Physical Review B*, 98(1):014502, 2018.

[19] Pradnya Parab, Deepak Singh, Santosh Haram, RP Singh, and Sangita Bose. Point contact andreev reflection studies of a non-centro symmetric superconductor Re_6Zr. *Scientific Reports*, 9(1):1–9, 2019.

[20] K Sugawara, T Sato, S Souma, T Takahashi, and A Ochiai. Anomalous superconducting-gap symmetry of noncentrosymmetric La_2C_3 observed by ultrahigh-resolution photoemission spectroscopy. *Physical Review B*, 76(13):132512, 2007.

[21] S Kuroiwa, Y Saura, J Akimitsu, M Hiraishi, M Miyazaki, KH Satoh, S Takeshita, and R Kadono. Multigap superconductivity in sesquicarbides La_2C_3 and Y_2C_3. *Physical Review Letters*, 100(9):097002, 2008.

[22] B Matthias. Superconductivity of AuBe. *Journal of Physics and Chemistry of Solids*, 10(4):342–343, 1959.

[23] Drew Jared Rebar. Exploring superconductivity in chiral structured AuBe. *PhD Thesis*, 1(1):1, 2015.

[24] Alfred Amon, Eteri Svanidze, R Cardoso-Gil, MN Wilson, H Rosner, Matej Bobnar, Walter Schnelle, Jeffrey W Lynn, R Gumeniuk, C Hennig, et al. Noncentrosymmetric superconductor BeAu. *Physical Review B*, 97(1):014501, 2018.

[25] D Singh, AD Hillier, and RP Singh. Type-I superconductivity in the noncentrosymmetric superconductor BeAu. *Physical Review B*, 99(13):134509, 2019.

[26] James Beare, Matthew Nugent, MN Wilson, Yipeng Cai, TJS Munsie, Alfred Amon, Andreas Leithe-Jasper, Zizhou Gong, SL Guo, Zurab Guguchia, et al. μSR and magnetometry study of the type-I superconductor BeAu. *Physical Review B*, 99(13):134510, 2019.

[27] Drew J Rebar, Serena M Birnbaum, John Singleton, Mojammel Khan, JC Ball, PW Adams, Julia Y Chan, DP Young, Dana A Browne, and John F DiTusa. Fermi surface, possible unconventional fermions, and unusually robust resistive critical fields in the chiral-structured superconductor AuBe. *Physical Review B*, 99(9):094517, 2019.

[28] B.D Cullity. The crystal structure of AuBe. *Transactions of the American Institute of Mining, Metallurgical and Petroleum Engineers*, 171.

[29] Koichi Momma and Fujio Izumi. VESTA 3 for three-dimensional visualization of crystal, volumetric and morphology data. *Journal of applied crystallography*, 44(6):1272–1276, 2011.

[30] Barry Bradlyn, Jennifer Cano, Zhijun Wang, MG Vergniory, C Felser, Robert Joseph Cava, and B Andrei Bernevig. Beyond dirac and Weyl fermions: Unconventional quasiparticles in conventional crystals. *Science*, 353(6299), 2016.

[31] Peizhe Tang, Quan Zhou, and Shou-Cheng Zhang. Multiple types of topological fermions in transition metal silicides. *Physical Review Letters*, 119(20):206402, 2017.

[32] Guoqing Chang, Su-Yang Xu, Benjamin J Wieder, Daniel S Sanchez, Shin-Ming Huang, Ilya Belopolski, Tay-Rong Chang, Songtian Zhang, Arun Bansil, Hsin Lin, et al. Unconventional chiral fermions and large topological fermi arcs in RhSi. *Physical Review Letters*, 119(20):206401, 2017.

[33] XZ Yu, Naoya Kanazawa, Yoshinori Onose, K Kimoto, WZ Zhang, Shintaro Ishiwata, Yoshio Matsui, and Yoshinori Tokura. Near room-temperature formation of a skyrmion crystal in thin-films of the helimagnet FeGe. *Nature Materials*, 10(2):106–109, 2011.

[34] Akira Tonomura, Xiuzhen Yu, Keiichi Yanagisawa, Tsuyoshi Matsuda, Yoshinori Onose, Naoya Kanazawa, Hyun Soon Park, and Yoshinori Tokura. Real-space observation of skyrmion lattice in helimagnet MnSi thin samples. *Nano letters*, 12(3):1673–1677, 2012.

[35] N Kanazawa, J-H Kim, DS Inosov, JS White, N Egetenmeyer, JL Gavilano, S Ishiwata, Y Onose, T Arima, B Keimer, et al. Possible skyrmion-lattice ground state in the B_{20} chiral-lattice magnet MnGe as seen via small-angle neutron scattering. *Physical Review B*, 86(13):134425, 2012.

[36] Rustem Khasanov, Ritu Gupta, Debarchan Das, Alfred Amon, Andreas Leithe-Jasper, and Eteri Svanidze. Multiple-gap response of type-I noncentrosymmetric BeAu superconductor. *Physical Review Research*, 2(2):023142, 2020.

[37] Rustem Khasanov, Ritu Gupta, Debarchan Das, Andreas Leithe-Jasper, and Eteri Svanidze. Single-gap versus two-gap scenario: Specific heat and thermodynamic critical field of the noncentrosymmetric superconductor BeAu. *Physical Review B*, 102(1):014514, 2020.

[38] Michael Tinkham. *Introduction to superconductivity*. Courier Corporation, 2004.

[39] James F Annett et al. *Superconductivity, superfluids and condensates*, volume 5. Oxford University Press, 2004.

[40] U Krägeloh. Flux line lattices in the intermediate state of superconductors with ginzburg landau parameters near $1/\sqrt{2}$. *Physics Letters A*, 28(9):657–658, 1969.

[41] J Auer and H Ullmaier. Magnetic behavior of type-II superconductors with small ginzburg-landau parameters. *Physical Review B*, 7(1):136, 1973.

[42] Egor Babaev, J Carlström, Mihail Silaev, and JM Speight. Type-1.5 superconductivity in multicomponent systems. *Physica C: Superconductivity and its Applications*, 533:20–35, 2017.

[43] Albert Samoilenka and Egor Babaev. Spiral magnetic field and bound states of vortices in noncentrosymmetric superconductors. *Physical Review B*, 102(18):184517, 2020.

[44] John Bardeen, Leon N Cooper, and John Robert Schrieffer. Theory of superconductivity. *Physical Review*, 108(5):1175, 1957.

[45] RC Dynes, V Narayanamurti, and J Pm Garno. Direct measurement of quasiparticle-lifetime broadening in a strong-coupled superconductor. *Physical Review Letters*, 41(21):1509, 1978.

[46] H Suhl, BT Matthias, and LR Walker. Bardeen-cooper-schrieffer theory of superconductivity in the case of overlapping bands. *Physical Review Letters*, 3(12):552, 1959.

[47] P Szabó, P Samuely, J Kačmarčík, Thierry Klein, J Marcus, Daniel Fruchart, Salvatore Miraglia, C Marcenat, and AGM Jansen. Evidence for two superconducting energy gaps in MgB_2 by point-contact spectroscopy. *Physical Review Letters*, 87(13):137005, 2001.

[48] F Giubileo, Dimitri Roditchev, William Sacks, Ronan Lamy, DX Thanh, Jean Klein, S Miraglia, Daniel Fruchart, J Marcus, and Ph Monod. Two-gap state density in MgB_2: a true bulk property or a proximity effect? *Physical Review Letters*, 87(17):177008, 2001.

[49] H Schmidt, JF Zasadzinski, KE Gray, and DG Hinks. Evidence for two-band superconductivity from break-junction tunneling on MgB_2. *Physical Review Letters*, 88(12):127002, 2002.

[50] Maria Iavarone, G Karapetrov, AE Koshelev, WK Kwok, GW Crabtree, DG Hinks, WN Kang, Eun-Mi Choi, Hyun Jung Kim, Hyeong-Jin Kim, et al. Two-band superconductivity in MgB_2. *Physical Review Letters*, 89(18):187002, 2002.

[51] RS Gonnelli, D Daghero, GA Ummarino, VA Stepanov, J Jun, SM Kazakov, and J Karpinski. Direct evidence for two-band superconductivity in MgB_2 single crystals from directional point-contact spectroscopy in magnetic fields. *Physical Review Letters*, 89(24):247004, 2002.

[52] JA Silva-Guillén, Y Noat, T Cren, W Sacks, Enric Canadell, and Pablo Ordejón. Tunneling and electronic structure of the two-gap superconductor MgB_2. *Physical Review B*, 92(6):064514, 2015.

[53] N Schopohl and K Scharnberg. Tunneling density of states for the two-band model of superconductivity. *Solid State Communications*, 22(6):371–374, 1977.

[54] Yves Noat, Tristan Cren, François Debontridder, Dimitri Roditchev, W Sacks, Pierre Toulemonde, and Alfonso San Miguel. Signatures of multigap superconductivity in tunneling spectroscopy. *Physical Review B*, 82(1):014531, 2010.

[55] MR Eskildsen, M Kugler, S Tanaka, J Jun, SM Kazakov, J Karpinski, and Ø Fischer. Vortex imaging in the π band of magnesium diboride. *Physical Review Letters*, 89(18):187003, 2002.

[56] Walter Kohn and Lu Jeu Sham. Self-consistent equations including exchange and correlation effects. *Physical Review*, 140(4A):A1133, 1965.

[57] Paolo Giannozzi, Stefano Baroni, Nicola Bonini, Matteo Calandra, Roberto Car, Carlo Cavazzoni, Davide Ceresoli, Guido L Chiarotti, Matteo Cococcioni, Ismaila Dabo, et al. Quantum espresso: a modular and open-source software

project for quantum simulations of materials. *Journal of Physics: Condensed Matter*, 21(39):395502, 2009.

[58] John P Perdew, Kieron Burke, and Matthias Ernzerhof. Generalized gradient approximation made simple. *Physical Review Letters*, 77(18):3865, 1996.

[59] Peter E Blöchl. Projector augmented-wave method. *Physical Review B*, 50(24):17953, 1994.

[60] Hendrik J Monkhorst and James D Pack. Special points for brillouin-zone integrations. *Physical review B*, 13(12):5188, 1976.

Appendix

3.A Investigation with Single Anisotropic Gap

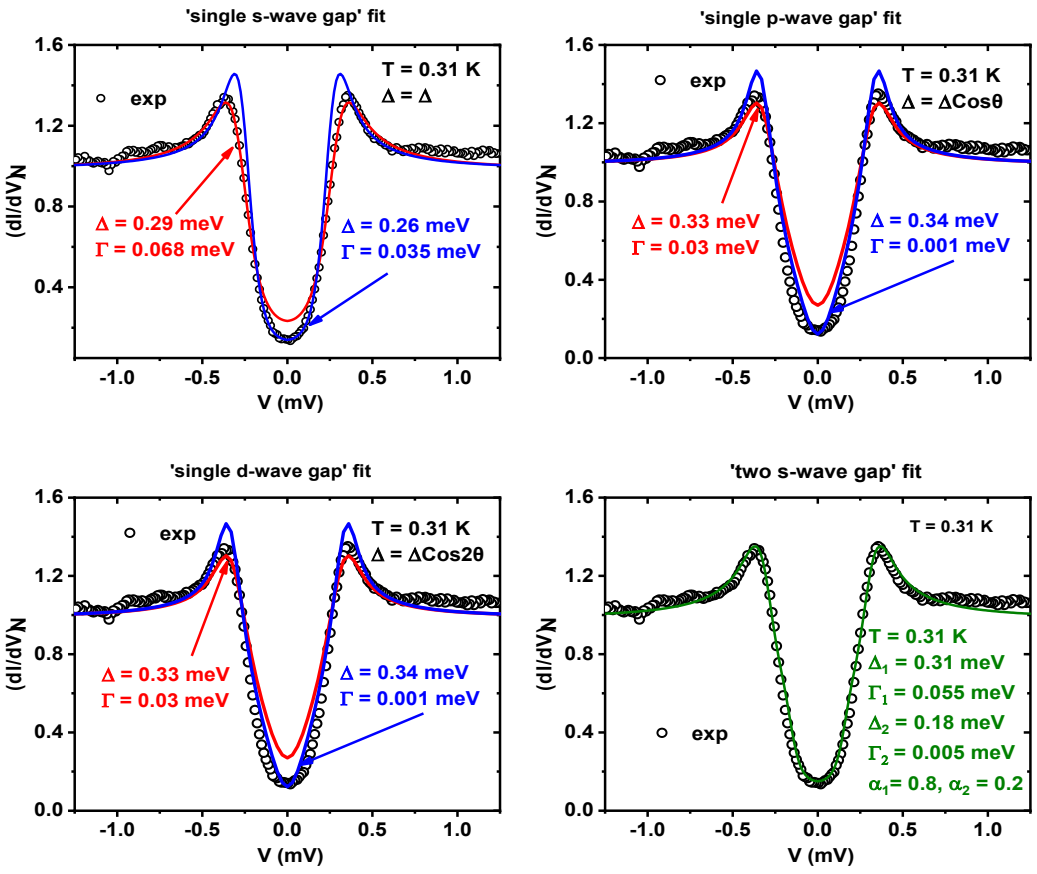

Figure 3.A.1: Inefficiency of the single-gap s, p or d-wave models to fit a typical spectrum of AuBe and the efficiency of a simple two-gap s-wave model for the same purpose

As the fitting with a single s-wave gap could not explain the experimental spectra recorded on AuBe, we did not immediately jump to a two-gap model. We also tried to fit the spectra with a single anisotropic gap like $\Delta Cos\theta$ (p-wave symmetry) or $\Delta Cos2\theta$ (d-wave symmetry) in place of an isotropic gap Δ (s-wave symmetry) according to 'Tanaka-Kashiwaya model' [1]. But such fittings with nodal/line gap could not resolve the issue. Rather, for such an anisotropic gap, the simulated spectrum generally becomes more 'V'-shaped and does not match at the bottom half of the experimental 'U'-shaped spectrum for any value of Δ or Γ at all. Or, if it somehow matches the bottom half, for the same parameter values, it fails (like before with s-wave symmetry) to match the upper half. Two gaps are necessary. and s-wave symmetry seems sufficient for fitting purpose. The issue is demonstrated in Fig. 3.A.1, comparatively. It is interesting to note that the anisotropic gaps overestimate the DOS at the lower bias region of the spectrum even with Γ as small as 0.001.

Two arguments, one from an experimental perspective and the other from a theoretical one, can be given why such a model with higher-order symmetry in the gap does not work in AuBe. Primarily, a signature feature of anisotropic gap is 'zero biased conductance peak' in the differential conductance. We did not find any such spectra anywhere on the sample surface. Moreover, for the nodal/line gap, the depth of the gap varies widely depending on the angle between the tip and the crystallite under the tip. At some point, when the tunneling direction is across any of the the nodes in the Fermi surface, a gapless flat spectrum is expected. On the contrary, all the spectra we probed had almost comparable depth. The only thing which varies from spectrum to spectrum is the position of the coherence peaks. Also, we did not find any flat spectrum anywhere on the sample surface.

From the theoretical perspective, we can also have qualitative arguments supporting the s-wave order parameter symmetry in AuBe. From the results of first-principles electronic structure calculations, we found the dominant contribution of the Be at Fermi level. The states close to the Fermi energy are the most relevant for superconductivity. Hence, the superconductivity is expected to be related to the phonon modes of the light Be atoms. As the SOC is not strong enough,

only conventional phonon-mediated BCS superconductivity exists in this material. This is already discussed briefly in Section 3.4 of the main chapter regarding band structure calculations.

3.B Discussion about Broadening Parameter

The extracted values of the two broadening parameters (Γ_1 and Γ_2) throughout the T range are presented in Fig. 3.B.1(a) in the same scale of the two gaps (Δ_1 and Δ_2). A general assumption about Γ is that it should increase with increasing temperature as scattering also does. Interestingly, in the case of AuBe, they remain almost constant (actually decrease slightly) with increasing T. At a first glance it might seem irregular but it is not. In the pioneering paper by Dynes *et al.* [2], the authors pointed out that such behaviour is a describing feature of a weakly coupled superconductor (like Al) *vis-a-vis* a strongly coupled one (like PbBi). Our observation is consistent with the previous reports [3–5] that AuBe is a weakly coupled superconductor with a specific heat jump near T_c, $\Delta C/\gamma_n T_c \approx 1.26$, and coupling strength $\lambda_{e-p} \approx 0.5$. Moreover, as can be seen in Fig. 3.B.1(c), the ratios of Γ/Δ actually increase with T for both bands. The field dependence of Γ_1 and Γ_2 are presented in the inset of Fig. 3.B.1(b). With increasing magnetic field, Γ_1 increases almost linearly where, Γ_2 increases slowly up to $\sim$10 kG and then increases faster.

3.C Magnetic Field Dependence of DOS

In order to explain a detailed tunneling spectroscopic study on the vortex lattice of MgB_2 reported by Eskildsen et al. [6], Koshelev and Golubov [7] developed a general theory for a two-band superconductor under weak interband scattering. In such a superconductor, the two bands develop two different field scales, which can be revealed by the distributions of the order parameters and the local DOS. Consequently, the two bands attain their normal state DOS at two different rates with respect to increasing magnetic field strength. Considering a negligible difference in the coupling constants, the ratio of the diffusion constants of the two bands is the

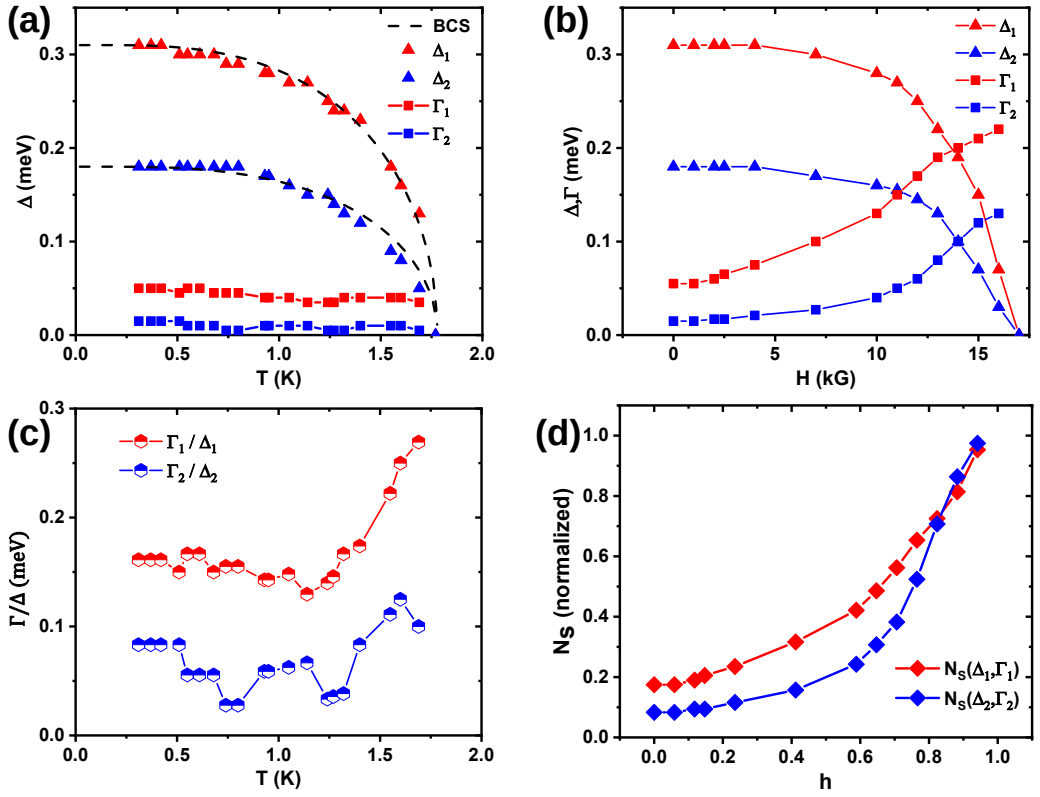

Figure 3.B.1: **(a)** The temperature (T) evolution of the two broadening parameters (Γ_1 and Γ_2) associated with (and in the same scale of) the two gaps (Δ_1 and Δ_2) extracted from the fittings presented in Fig. 3.5(a). **(b)** The magnetic field evolution of the same, extracted from Fig. 3.6(a). **(c)** The T dependence of the two Γ/Δ ratios for both bands. **(d)** Normalised zero-bias DOS corresponding to two different bands as a function of the reduced magnetic field $h = H/H_{c(l)}$.

only parameter to determine this relative rate. For MgB_2 as an example, the ratio 0.2 best explains the experimental results of Eskildsen *et al.* [6]. To understand this effect in our present context for AuBe, we calculated the magnetic field dependence of the DOS for the respective bands using the formula for $N_{sj}(E)$ described earlier (Eqn. 3.3 in the main chapter) and the fitting parameters used in Fig. 3.B.1(b). The x-axis is normalised by $H_{c(l)}$=17 kG (spectroscopically measured local critical field) and y-axis is normalised by dividing the $[dI/dV]_{V=0\ meV}$ with $[dI/dV]_{V=1.5\ meV}$. As it can be seen in Fig. 3.B.1(d), the larger DOS N_{s1} (corresponding to the electron pocket at the Γ-point and the larger gap Δ_1) initially rises faster with increasing field to attain the normal state DOS (i.e. N_s=1) compared to the smaller DOS N_{s2} (corresponding to the hole pocket at the M-point and the smaller gap Δ_2). However, though N_{s2} initially starts with a slower rate, latter it increases faster and attains the normal state DOS almost at the same field value N_{s1} does. From the visual interpretation, this result can be compared with the situation where the ratio of the diffusion constants is 1 in the proposed model. This suggests that, unlike in MgB_2, the two bands responsible for the superconductivity in AuBe have comparable transport characteristics. Possibly for the same reason, unlike in MgB_2, the two gaps are not distinctly resolved in the tunneling spectra of AuBe. To note, the model developed by Koshelev and Golubov [7] had its own limitations as it assumed a large Ginzburg Landau parameter (κ). It serves the purpose for MgB_2 as $\kappa \geq 10$ for that material [7]. However, in our present case for AuBe, reported κ mostly varies between 0.4 [5] to 0.75 [4] depending on the clean to dirty limit (except a widely different value 2.34 initially reported in Ref. [3]). Some recent theoretical works [8, 9] based on an intertype domain between type-I and type-II can be interesting in this context and relevant for multiband superconductors with low κ like AuBe.

Bibliography

[1] Yukio Tanaka and Satoshi Kashiwaya. Theory of tunneling spectroscopy of d-wave superconductors. *Physical Review Letters*, 74(17):3451, 1995.

[2] RC Dynes, V Narayanamurti, and J Pm Garno. Direct measurement of quasiparticle-lifetime broadening in a strong-coupled superconductor. *Physical Review Letters*, 41(21):1509, 1978.

[3] Alfred Amon, Eteri Svanidze, R Cardoso-Gil, MN Wilson, H Rosner, Matej Bobnar, Walter Schnelle, Jeffrey W Lynn, R Gumeniuk, C Hennig, et al. Noncentrosymmetric superconductor BeAu. *Physical Review B*, 97(1):014501, 2018.

[4] Drew J Rebar, Serena M Birnbaum, John Singleton, Mojammel Khan, JC Ball, PW Adams, Julia Y Chan, DP Young, Dana A Browne, and John F DiTusa. Fermi surface, possible unconventional fermions, and unusually robust resistive critical fields in the chiral-structured superconductor AuBe. *Physical Review B*, 99(9):094517, 2019.

[5] D Singh, AD Hillier, and RP Singh. Type-I superconductivity in the noncentrosymmetric superconductor BeAu. *Physical Review B*, 99(13):134509, 2019.

[6] MR Eskildsen, M Kugler, S Tanaka, J Jun, SM Kazakov, J Karpinski, and Ø Fischer. Vortex imaging in the π band of magnesium diboride. *Physical Review Letters*, 89(18):187003, 2002.

[7] AE Koshelev and Alexandre Avraamovitch Golubov. Mixed state of a dirty two-band superconductor: Application to MgB_2. *Physical Review Letters*, 90(17):177002, 2003.

[8] Mihail Silaev and Egor Babaev. Microscopic theory of type-1.5 superconductivity in multiband systems. *Physical Review B*, 84(9):094515, 2011.

[9] Alexei Vagov, AA Shanenko, MV Milošević, MA Vollrath, VM Vinokur, J Albino Aguiar, and FM Peeters. Superconductivity between standard types: Multiband versus single-band materials. *Physical Review B*, 93(17):174503, 2016.

Chapter 4

Multiband Superconductivity in RuB_2

In this chapter, I will report our tunneling spectroscopic investigation on another multiband superconductor, RuB_2. The multiband mechanism in RuB_2, as we found out, is not as straight forward as in AuBe, and that requires a more extensive analysis. The work presented in this chapter is already partially published in Ref. [1].

4.1 Introduction

The discovery of two-band superconductivity in MgB_2 [2–7] with an unusually high T_c of 40 K sparked interest in multiband superconductivity research. The two-band nature of MgB_2 drew that attention because the signature of the two gaps could be clearly established in this case using a variety of techniques, including tunneling spectroscopy, where the quasiparticle excitation spectrum directly reflected the two gaps [7–11]. The experimental results on MgB_2 was well characterised by theoretical models that included two BCS gaps and moderate interband scattering [12–16]. This discovery sparked interest in the superconducting characteristics of a wide range of binary diborides [17, 18]. OsB_2 and RuB_2 drew the most attention in this context because of their differences with MgB_2 in terms of crystal and band structure [19–21], but potentially feasible multiband super-

conductivity [22–24] like MgB_2. Based on heat capacity and penetration depth measurements on single crystals [23], OsB_2 ($T_c \sim 2.1$ K) was proposed as a two-gap superconductor. Furthermore, experiments of field dependent heat capacity and magnetisation indicated that OsB_2 is a Type-II superconductor [22, 23].

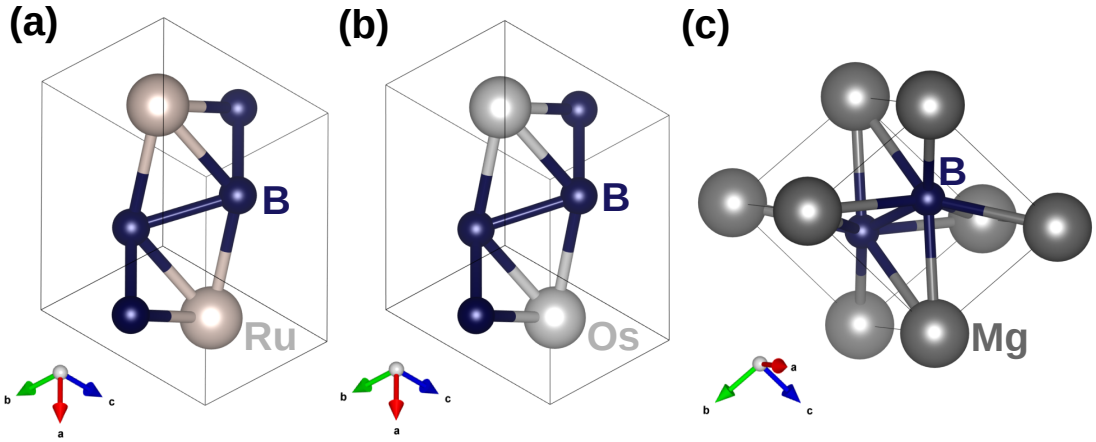

Figure 4.1.1: The crystal structures of **(a)** RuB_2, **(b)** OsB_2, and **(c)** MgB_2, with one unit cell each.

RuB_2 has an orthorhombic crystal structure (space group *Pmmn*) isostructural to OsB_2 (see Fig. 4.1.1 for comparison) [25–27]. It superconducts below 1.5 K [17], and the bulk superconducting phase exhibits unexpected type-I like magnetic characteristics [28]. The bulk critical field was found to be very low (~ 120 Oe), the electron-phonon coupling was found to be weak ($\lambda_{ep} \sim 0.4$), and the temperature dependence of specific heat showed an anomaly that could be well fitted within a two-gap model [28, 29] with the gap values $\Delta_1 \sim 0.15$ meV and $\Delta_2 \sim 0.3$ meV. RuB_2 is unique since it has multigap superconductivity and a type-I character. However, in order to gain conclusive evidence of multiband superconductivity and to comprehend the nature of the gaps, it is critical to spectroscopically quantify the gaps and directly assess their temperature dependence.

4.2 Experimental Techniques

We have attempted to probe the multiple gaps in RuB_2 and their response to temperature and magnetic field by low-temperature scanning tunneling microscopy/spectroscopy (STM/S). The preparation and characterization of the polycrystalline samples used for the measurements are already reported in Ref. [28]. The STS experiments were carried out in the ultra-high vacuum (UHV) cryostat working down to 300 mK (Unisoku system with RHK R9 controller). Since STM experiments are extremely sensitive to the surface cleanliness of a material, in order to ensure a pristine surface of RuB_2, a few layers of the surface was first removed by mild reverse sputtering in an argon environment *in-situ* inside an UHV preparation chamber, prior to the STS experiments. All STS experiments were performed with sharp metallic tips of tungsten (W) which were fabricated by electrochemical etching and were cleaned by electron beam bombardment under UHV in the preparation chamber.

4.3 Results and Discussions

4.3.1 Analysis Under Single-gap Model

The STS experiments were done by bringing the STM tip on the central parts of different grains on the surface and subsequently recording the dI/dV vs V spectra for every such point. In Fig. 4.3.1, six such spectra are represented. The spectra were first normalized to the conductance at 1.5 mV (where they become nearly flat) and then analyzed within the single-band model in the same way as in the last chapter (using Eqn. 3.1 and 3.2). However, it turned out that such fitting works for only a group of spectra. In Fig. 4.3.1(a)-(c), three such experimentally probed spectra are represented with black circles and the corresponding theoretical plots with red lines. Here, the theoretical curves fall almost completely on the experimental data points, except a little discrepancy just above the coherence peaks. This discrepancy, where the experimental plots show a pair of 'dip-like feature' just above the coherence peaks, will be discussed more elaborately in the appendix of this chapter. Considering all the spectra (which were probed at different points on the sample surface) that could be fitted using a single-gap

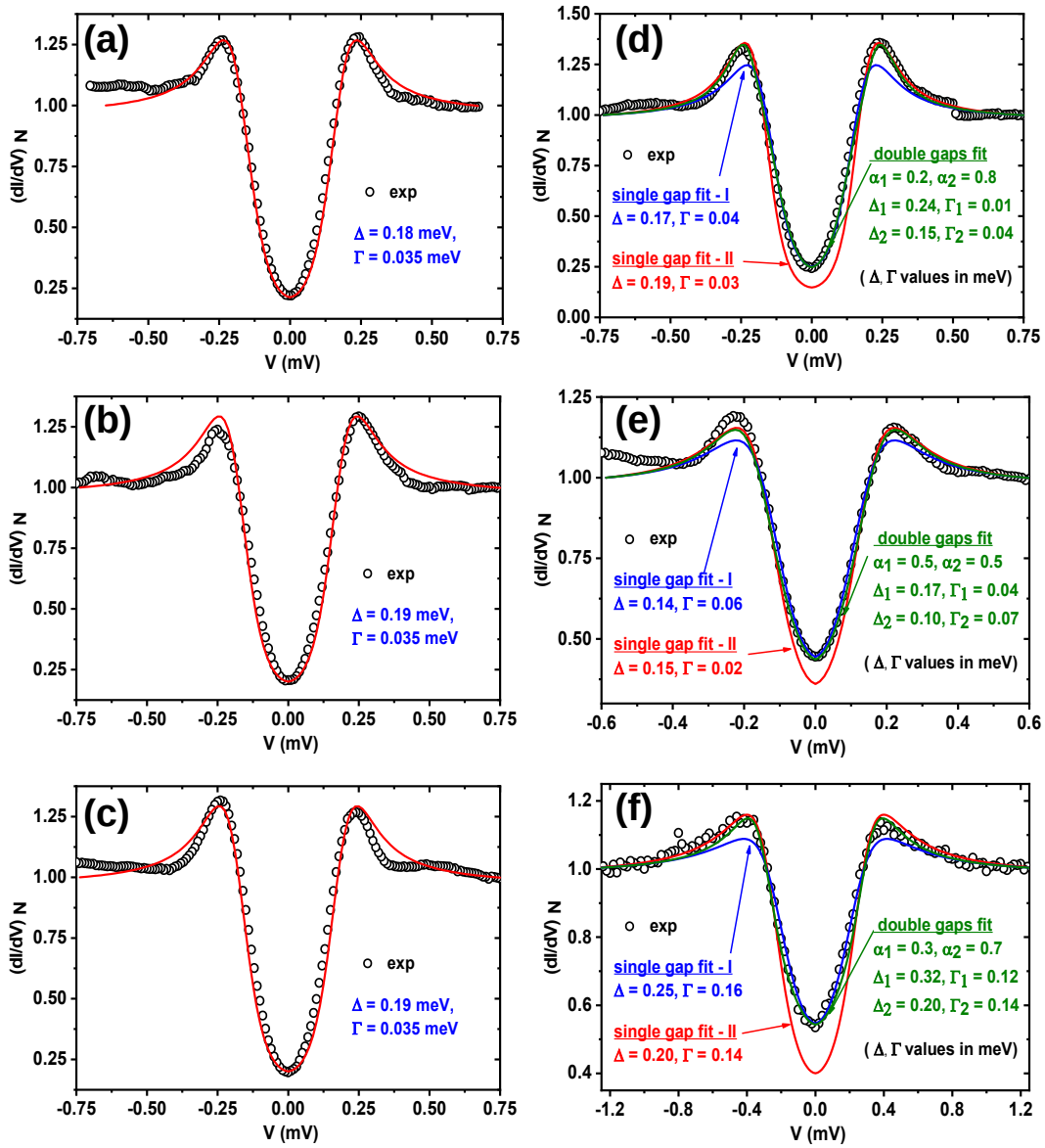

Figure 4.3.1: Two types of tunneling spectra probed on the surface of RuB_2 with corresponding theoretical fits. Spectra **(a), (b), (c)** show agreement with a single-gap *s*-wave model (red line), but spectra **(d), (e), (f)** need a two-gap model (green line). For comparison, best possible single-gap fits are also shown (red and blue line) in (d), (e) and (f).

model, the average value of $\Delta \sim 200$ μeV. The other group of spectra, however, show a significant deviation from the fittings based on such a single-gap model. Three such spectra are represented in Fig. 4.3.1(d)-(f), where the single-gap fit either matches the upper part (red line) or the lower part (blue lines) but never the whole spectrum.

4.3.2 Indications of Multiband Superconductivity

Before jumping towards a two-gap spectral analysis next, let us look for the signature of multiband superconductivity in RuB_2 from previous reports. As it can be seen in the reported DOS [28, 29] for RuB_2, only two bands, Ru $4d$ orbital and B $2p$ orbital, contribute to the Fermi surface. This gives the first indication towards the possibility of two-band superconductivity in RuB_2. However, a closer inspection would reveal that there is a very small difference between the DOS near E_F for the two bands. In fact, slightly above E_F, the DOS of the two bands become almost identical. Intrinsic defects and electronic disorders may cause a shift in E_F making the DOS in the two bands nearly equal. In such a situation, there are two possibilities. First, even though the material is indeed a two-gap superconductor, it would behave like a single-gap one experimentally. Second, it could still show two-gap behavior experimentally, and in that case the mechanism that would lead to the difference in the two gaps is the difference in the Eliashberg electron-phonon coupling terms (λ_{11} and λ_{22}) in the respective bands [12, 30, 31]. Qualitatively, a comparison of the Fermi velocities (v_F) in the two bands based on the calculation presented in Ref. [28] revealed that one band has smaller $v_F \sim 1.1$ x 10^6 m/s than the other band ($v_F \sim 1.6$ x 10^6 m/s). The band with smaller v_F is expected to have larger $e-p$ coupling causing the larger gap. However, all these arguments are speculative statements. The only major signature of two-gap superconductivity in RuB_2 is that the temperature dependence of specific heat showed an anomaly and that anomaly could be resolved [28] within a 'two-gap model' with the gap values $\Delta_1 \sim 0.15$ meV and $\Delta_2 \sim 0.3$ meV. To note, such a measurement is not an energy-resolved technique and hence provides only an indirect proof of two-gap superconductivity. Still, that observation at least gives us a direction to proceed further when we have some spectra (Fig. 4.3.1(d)-(f)) where single-gap model does

not work.

4.3.3 Analysis Under Two-gap Model

The issue can be immediately resolved if a simple two-gap model [32] is considered as used in the last chapter to analyse STS data of AuBe (Eqn. 3.3 and 3.4). According to this model, the quasiparticle excitation spectrum for a two-band model can be calculated simply by adding two single-gap BCS spectra for the two respective bands (say, band 1 and band 2). Using this model, the spectra as in Fig. 4.3.1(d)-(f) could be fitted nicely over the entire energy range (see the green line on the black circles) and the relative contributions of the two bands to the total tunneling current, i.e. α_1 and α_2 varies from spectrum to spectrum.

4.3.4 Differences with AuBe

At this point, we note two important differences in the results of our two-gap analysis between our previous investigation on AuBe and the present investigation on RuB_2. First of all, in AuBe, all the spectra we probed needed two gaps to explain them. Whatever the spectra visually looked like, the single-gap model never worked. Here, in RuB_2, although we did probe some spectra where two gaps are needed, we also probed a number of spectra where a single-gap model is sufficient. On the second note, in AuBe, we found the extracted values of the two gaps (Δ_1 and Δ_2) are very consistent for spectra probed at different locations on the sample surface. However, in the case of RuB_2, the same two-gap analysis provides different pairs of values for the two gaps from one spectrum to another. In the appendix of this chapter, I will discuss about some further modifications in the two-gap model where the above two observations can be considered as direct consequences. The average values of the two gaps we found to be $\Delta_1 \sim 300$ μeV and $\Delta_2 \sim 150$ μeV which match well with the prediction based on previous bulk measurements [28].

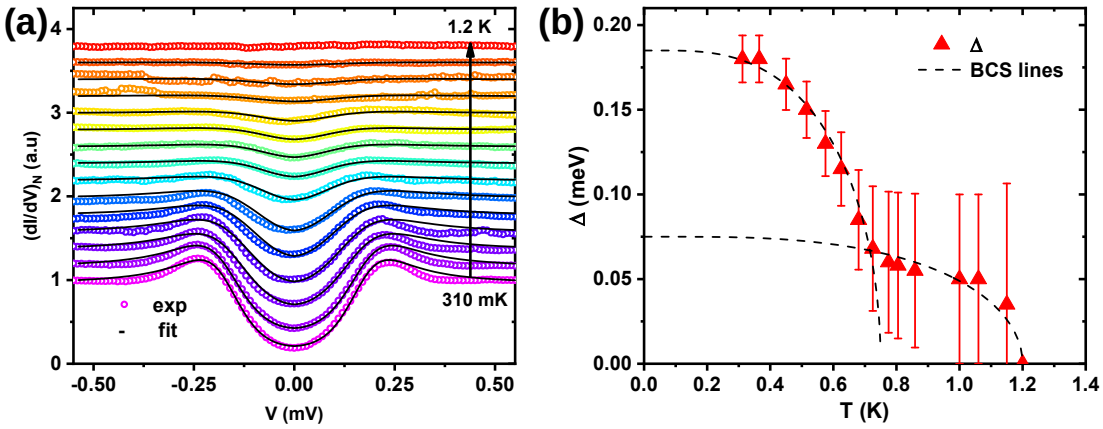

Figure 4.3.2: **(a)** Temperature dependence of tunneling conductance spectra of RuB_2 with best theoretical fits considering single-gap model.**(b)** Evolution of the gap (Δ) with temperature, extracted from the plot (a) and two different BCS lines for comparison.

4.3.5 Two-step Like Transition

In AuBe, we had a very robust two-gap signature from spectral data. In comparison to that, here in RuB_2, the result of our spectral analysis at the lowest temperature is not that conclusive. Therefore, in order to gain more information about the superconducting gap (or gaps), we decided to look at the temperature and magnetic field dependence of the spectra. For that purpose, we chose such a spectrum that satisfied all three following conditions,

- The single-gap model should be able to fit the spectrum with a small but noticeable discrepancy.
- The spectrum should have the unconventional 'dip-like feature' above the coherence peaks.
- The two-gap model discussed before would improve the fitting quality.

Then we observed the temperature (T) dependence of that spectrum, gradually increasing the sample temperature. The results are presented in Fig. 4.3.2(a) with colour circles. All spectral features including coherence peaks disappear at 1.2

K. As a beginning point of our analysis, each spectrum is fitted with the single-gap model (black lines in Fig. 4.3.2(a)), and the extracted Δ are plotted with T in Fig. 4.3.2(b). Initially, Δ varies very smoothly with T as expected for a BCS superconductor. The black dashed lines represent two such pure BCS T dependences [33]. However, around 0.75 K the variation of Δ unexpectedly changes the slope and finally vanishes at 1.2 K. This 'kink' at 0.75 K seemingly breaks the transition in two parts where each part follows their independent BCS prediction lines. One possible explanation of such a 'tail' like feature could be 'pseudo-gap'. But it is interesting to note that 0.75 K is far below the bulk T_c (=1.5 K) above which one would expect such a 'pseudo-gap' feature. Even though we restricted our analysis within a single band model, such unusual behaviour gives us a strong indication of a multiband mechanism in superconducting RuB_2. To verify the same, we will analyse the same data with the 'two-gap' model. Before that, let us go through the magnetic field dependence of the same spectrum and look for any further useful insights.

4.3.6 Unusually High Spectral $H_{c(l)}$

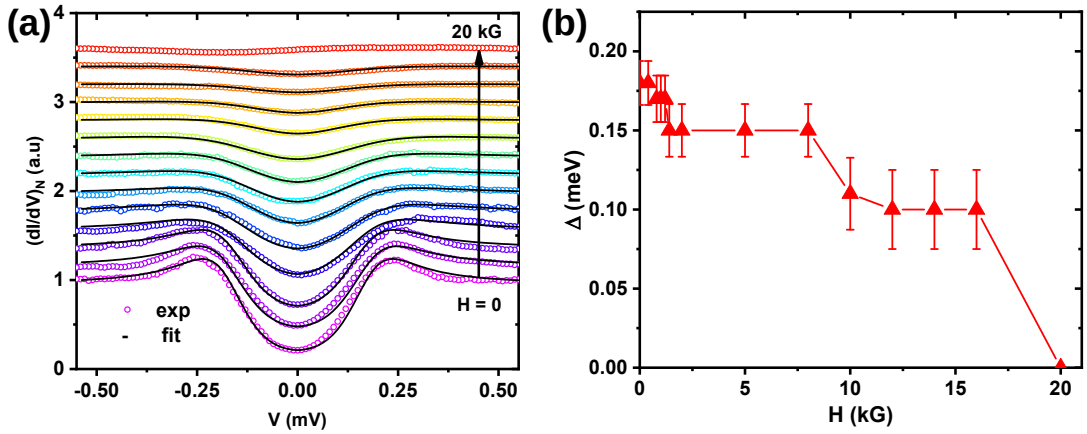

Figure 4.3.3: **(a)** Magnetic field dependence of the spectra of RuB_2 with best theoretical fits considering single-gap model.**(b)** Evolution of Δ with increasing field strength, extracted from the plot (a).

The experimentally obtained magnetic field (H) dependent STS spectra are shown by colored circles in Fig. 4.3.3(a). The corresponding single-gap fits are

also shown for each spectrum. The evolution of the extracted Δ with magnetic field are shown in Fig. 4.3.3(b). Δ decreases monotonically with increasing H but survives up to ~ 20 kG! This is surprising because the bulk critical field H_c of RuB_2 is reported [28] to be just above 100 G. There must be some reason why superconductivity is surviving at such a large field at the surface although it is already destroyed in the bulk. Furthermore, while the bulk measurements [28] revealed a first-order disappearance of superconductivity at H_c as in a type-I superconductor, the spectroscopic measurements clearly show a gradual disappearance of gap. As the multiple sets of the magnetic field dependence of spectra probed at different positions on the sample surface indicate the same result of high local critical field ($H_{c(l)}$), the possibility of any artefact can be eliminated. This high $H_{c(l)}$ in RuB_2 immediately reminds us of the high $H_{c(l)}$ in superconducting AuBe we have discussed in the last chapter (though the evolution of both gaps with the increasing field was different in the latter case). The survival of superconductivity far above bulk H_c is not something new. It is reported in multiple scenarios for as simple a superconductor as lead (Pb). Either probed under surface sensitive measurements like point contact spectroscopy or in nano-structured form, Pb is reported to sustain superconductivity in a magnetic field 10 to 100 times higher than bulk H_c [34–37]. However, as we will see later (details in the appendix of this chapter), particularly in the context of a multiband superconductor, the observation of such high $H_{c(l)}$ can have a more interesting explanation. That discussion will be relevant for our observation on AuBe as well as RuB_2. At this stage, we can surmise that, between the bulk H_c and the local $H_{c(l)}$, the system may be in its mixed state.

In the next step, we will analyse the same set of spectra (presented in Fig. 4.3.2(a) and 4.3.3(a)) under two-gap model. The results of such fittings are depicted in Fig. 4.3.4. The two gaps extracted from the fits are plotted with temperature in Fig. 4.3.4(a) with red (Δ_1) and blue (Δ_2) triangles. The two gaps follow different temperature dependencies. As can be seen, at $T \sim 0.7$ K, the two gaps merge with each other and at higher T they deviate from their initial individual BCS trend line [33]. Above 1 K, the two gaps are completely un-resolvable and a two-gap fitting does not make any practical sense. Such temperature dependence of the two gaps is unique and way too different from what we observed in

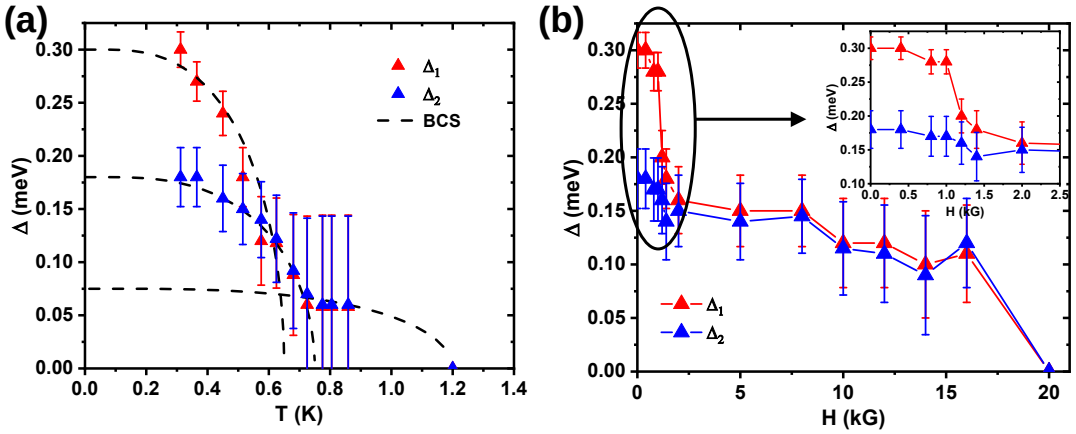

Figure 4.3.4: Results of the two-gap analysis for the same spectra presented at Fig. 4.3.2 and 4.3.3.**(a)** Evolution of the two gaps (Δ_1 and Δ_2) with temperature and **(b)** evolution of the same with magnetic field.

AuBe (see Fig. 3.5(b) in the last chapter). Merging of the two gaps indicates high inter-band scattering. In the appendix of this chapter, we will discuss a modified two-gap model incorporating such inter-band scattering. This kind of deviation from BCS-like behavior is not uncommon for multiband superconductors. Rather, the unconventional nature of Δ and anisotropy in its temperature and magnetic field dependence actually leads to the discovery of multiband superconductivity in YNi_2B_2C with small interband scattering [38]. What seems to be unique for RuB_2 is that, the inter-band scattering itself is evolving with T causing the merging of the gaps at one point.

Now we will concentrate on the magnetic field dependence of the spectra presented in Fig. 4.3.3(a) under the lens of the two-gap model. The results of such fittings are depicted in Fig. 4.3.4(b), where the evolutions of the two gaps with H are depicted. At a first look, the dependence seems very peculiar and unusual. Up to $\sim$ 1.6 kG, Δ_1 falls rapidly but Δ_2 shows a relatively small change. Beyond this field, the difference between the two gaps becomes very small and the spectra almost behave like a single-gap one. If we look at the T and H dependences of the experimental spectra (Fig. 4.3.2(a) and Fig. 4.3.3(a)), they are extremely clean and the superconducting features in them are smoothly varying. Therefore,

any possibility of experimental artefact can be ignored. The fact that the fittings (both based on a single-gap model and a simple two-gap model we have used so far) are providing unusual results warrants exploration of further modifications in the fitting model itself. I will discuss two such modifications in the two-gap fitting model in the appendix of this chapter. Possible explanations behind such a high local critical field $H_{c(l)}$, including surface superconductivity and mixed state (particularly in the context of a multiband superconductor) will also be discussed in the appendix.

4.4 Summary

In conclusion, I have given a comprehensive scanning tunneling spectroscopic investigation of two-band superconductivity in RuB_2 . We report that whereas a single-gap *s*-wave model can explain a group of spectra investigated on the surface of this material, at least two gaps are required for the rest. Our findings are consistent with previous reports based on bulk indirect measurements [28]. Our findings also reveal an unique magnetic field dependence of the spectral gap(s), which remain finite much above the thermodynamic H_c where bulk superconductivity already destroyed. We also see a 'dip-like' spectral pattern at the higher bias, which could be due to the order parameter's unusual higher-order symmetry.

Acknowledgements

The ULT STM/S data were acquired by Aastha Vasdev, Soumyadip Halder and Shekhar Das with my active participation in the process. Jaskaran Singh and Dr. Yogesh Singh synthesized the polycrystaline sample. We thank Dr. Divya Srivastava for providing us the information on Fermi velocity of the bands.

Bibliography

[1] Soumya Datta, Aastha Vasdev, Soumyadip Halder, Jaskaran Singh, Yogesh Singh, and Goutam Sheet. Spectroscopic signature of two superconducting gaps and their unusual field dependence in RuB_2. *Journal of Physics: Condensed Matter*, 32(31):315701, 2020.

[2] Jun Nagamatsu, Norimasa Nakagawa, Takahiro Muranaka, Yuji Zenitani, and Jun Akimitsu. Superconductivity at 39 K in Magnesium Diboride. *Nature*, 410(6824):63–64, 2001.

[3] G Karapetrov, M Iavarone, WK Kwok, GW Crabtree, and DG Hinks. Scanning tunneling spectroscopy in MgB_2. *Physical Review Letters*, 86(19):4374, 2001.

[4] F Bouquet, RA Fisher, NE Phillips, DG Hinks, and JD Jorgensen. Specific heat of $Mg^{11}B_2$: evidence for a second energy gap. *Physical Review Letters*, 87(4):047001, 2001.

[5] P Szabó, P Samuely, J Kačmarčík, Thierry Klein, J Marcus, Daniel Fruchart, Salvatore Miraglia, C Marcenat, and AGM Jansen. Evidence for two superconducting energy gaps in MgB_2 by point-contact spectroscopy. *Physical Review Letters*, 87(13):137005, 2001.

[6] XK Chen, MJ Konstantinović, JC Irwin, DD Lawrie, and JP Franck. Evidence for two superconducting gaps in MgB_2. *Physical Review Letters*, 87(15):157002, 2001.

[7] F Giubileo, Dimitri Roditchev, William Sacks, Ronan Lamy, DX Thanh, Jean Klein, S Miraglia, Daniel Fruchart, J Marcus, and Ph Monod. Two-gap state

density in MgB_2: a true bulk property or a proximity effect? *Physical Review Letters*, 87(17):177008, 2001.

[8] H Schmidt, JF Zasadzinski, KE Gray, and DG Hinks. Evidence for two-band superconductivity from break-junction tunneling on MgB_2. *Physical Review Letters*, 88(12):127002, 2002.

[9] Maria Iavarone, G Karapetrov, AE Koshelev, WK Kwok, GW Crabtree, DG Hinks, WN Kang, Eun-Mi Choi, Hyun Jung Kim, Hyeong-Jin Kim, et al. Two-band superconductivity in MgB_2. *Physical Review Letters*, 89(18):187002, 2002.

[10] RS Gonnelli, D Daghero, GA Ummarino, VA Stepanov, J Jun, SM Kazakov, and J Karpinski. Direct evidence for two-band superconductivity in MgB_2 single crystals from directional point-contact spectroscopy in magnetic fields. *Physical Review Letters*, 89(24):247004, 2002.

[11] Jose Angel Silva-Guillén, Y Noat, T Cren, W Sacks, Enric Canadell, and Pablo Ordejon. Tunneling and electronic structure of the two-gap superconductor MgB_2. *Physical Review B*, 92(6):064514, 2015.

[12] Amy Y Liu, II Mazin, and Jens Kortus. Beyond eliashberg superconductivity in MgB_2: anharmonicity, two-phonon scattering, and multiple gaps. *Physical Review Letters*, 87(8):087005, 2001.

[13] F Bouquet, Y Wang, RA Fisher, DG Hinks, JD Jorgensen, A Junod, and NE Phillips. Phenomenological two-gap model for the specific heat of MgB_2. *Europhysics Letters*, 56(6):856, 2001.

[14] Alexandre Avraamovitch Golubov, J Kortus, OV Dolgov, O Jepsen, Y Kong, OK Andersen, BJ Gibson, K Ahn, and RK Kremer. Specific heat of MgB_2 in a one and a two-band model from first-principles calculations. *Journal of Physics: Condensed Matter*, 14(6):1353, 2002.

[15] Hyoung Joon Choi, David Roundy, Hong Sun, Marvin L Cohen, and Steven G Louie. The origin of the anomalous superconducting properties of MgB_2. *Nature*, 418(6899):758–760, 2002.

[16] AE Koshelev and Alexandre Avraamovitch Golubov. Mixed state of a dirty two-band superconductor: Application to MgB_2. *Physical Review Letters*, 90(17):177002, 2003.

[17] JM Vandenberg, BT Matthias, E Corenzwit, and H Barz. Superconductivity of some binary and ternary transition-metal Borides. *Materials Research Bulletin*, 10(9):889–894, 1975.

[18] Nadezhda I Medvedeva, Alexander L Ivanovskii, Julia E Medvedeva, and Arthur J Freeman. Electronic structure of superconducting MgB_2 and related binary and ternary Borides. *Physical Review B*, 64(2):020502, 2001.

[19] S Chiodo, HJ Gotsis, N Russo, and E Sicilia. OsB_2 and RuB_2, ultra-incompressible, hard materials: First-principles electronic structure calculations. *Chemical Physics Letters*, 425(4-6):311–314, 2006.

[20] Xianfeng Hao, Yuanhui Xu, Zhijian Wu, Defeng Zhou, Xiaojuan Liu, and Jian Meng. Elastic anisotropy of OsB_2 and RuB_2 from first-principles study. *Journal of Alloys and Compounds*, 453(1-2):413–417, 2008.

[21] Michael Frotscher, Markus Hoelzel, and Barbara Albert. Crystal structures of the metal diborides ReB_2, RuB_2, and OsB_2 from neutron powder diffraction, 2010.

[22] Yogesh Singh, A Niazi, MD Vannette, R Prozorov, and DC Johnston. Superconducting and normal-state properties of the layered boride OsB_2. *Physical Review B*, 76(21):214510, 2007.

[23] Yogesh Singh, C Martin, SL Bud'Ko, A Ellern, R Prozorov, and DC Johnston. Multigap superconductivity and Shubnikov de Haas oscillations in single crystals of the layered Boride OsB_2. *Physical Review B*, 82(14):144532, 2010.

[24] Jonas Bekaert, Stephan Vercauteren, Alexandros Aperis, Lucia Komendova, Ruslan Prozorov, Bart Partoens, and MV Milošević. Anisotropic type-I superconductivity and anomalous superfluid density in OsB_2. *Physical Review B*, 94(14):144506, 2016.

[25] B Aronsson, E Stenberg, and J Åselius. Borides of Ruthenium, Osmium and Iridium. *Nature*, 195(4839):377–378, 1962.

[26] B Aronsson et al. The crystal structure of RuB_2, OsB_2 and $IrB_{1\cdot 35}$ and some general comments on the crystal chemistry of borides in the composition range MeB−MeB_3. *Acta Chem. Scand.*, 17(17):2036, 1963.

[27] Koichi Momma and Fujio Izumi. VESTA 3 for three-dimensional visualization of crystal, volumetric and morphology data. *Journal of Applied Crystallography*, 44(6):1272–1276, 2011.

[28] Jaskaran Singh, Anooja Jayaraj, D Srivastava, S Gayen, A Thamizhavel, and Yogesh Singh. Possible multigap type-I superconductivity in the layered boride RuB_2. *Physical Review B*, 97(5):054506, 2018.

[29] Wang Yue-Qin, Yuan Lan-Feng, and Yang Jin-Long. Lattice dynamics and superconductivity of RuB_2: A first-principles study. *Chinese Physics Letters*, 25(8):3036, 2008.

[30] Hyoung Joon Choi, David Roundy, Hong Sun, Marvin L Cohen, and Steven G Louie. First-principles calculation of the superconducting transition in MgB_2 within the anisotropic eliashberg formalism. *Physical Review B*, 66(2):020513, 2002.

[31] EJ Nicol and JP Carbotte. Properties of the superconducting state in a two-band model. *Physical Review B*, 71(5):054501, 2005.

[32] H Suhl, BT Matthias, and LR Walker. Bardeen-cooper-schrieffer theory of superconductivity in the case of overlapping bands. *Physical Review Letters*, 3(12):552, 1959.

[33] John Bardeen, Leon N Cooper, and John Robert Schrieffer. Theory of superconductivity. *Physical Review*, 108(5):1175, 1957.

[34] CC Yang, FC Tsao, SY Wu, W-H Li, and KC Lee. Enhanced critical magnetic field in superconducting Pb nanoparticles. *Journal of Low Temperature Physics*, 131(3):349–352, 2003.

[35] José Gabriel Rodrigo, V Crespo, H Suderow, S Vieira, and F Guinea. Topological superconducting state of Lead nanowires in an external magnetic field. *Physical Review Letters*, 109(23):237003, 2012.

[36] Mingquan He, Chi Ho Wong, Pok Lam Tse, Yuan Zheng, Haijing Zhang, Frank LY Lam, Ping Sheng, Xijun Hu, and Rolf Lortz. Giant enhancement of the upper critical field and fluctuations above the bulk T_C in superconducting ultrathin Lead nanowire arrays. *ACS Nano*, 7(5):4187–4193, 2013.

[37] Anshu Sirohi, Preetha Saha, Sirshendu Gayen, Avtar Singh, and Goutam Sheet. Transport spectroscopy on trapped superconducting nano-islands of Pb: signature of unconventional pairing. *Nanotechnology*, 27(28):285701, 2016.

[38] Sourin Mukhopadhyay, Goutam Sheet, P Raychaudhuri, and H Takeya. Magnetic-field dependence of superconducting energy gaps in YNi_2B_2C: Evidence of multiband superconductivity. *Physical Review B*, 72(1):014545, 2005.

Appendix

4.A Unconventional Features in the Spectra

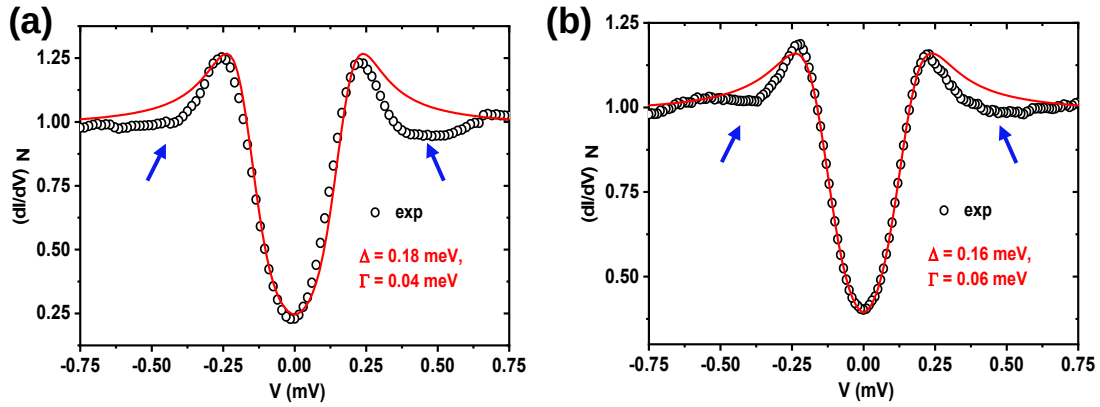

Figure 4.A.1: Two spectra of RuB_2 recorded at $T = 0.3$ K showing prominent dip like features (blue arrows) just above the coherence peaks. The best single gap fittings are also shown for comparison.

One of the unique features of the spectra probed on the surface of RuB_2 is a pair of dips at slightly higher bias than the position of the coherence peaks. For some spectra (like the ones previously presented in Fig. 4.3.1(b) and (c) in the main chapter), these dips were shallow and can only be noticed if the experimental spectra were carefully compared with the best single gap s-wave fit. For some spectra, however, such dips were much prominent. In Fig. 4.A.1 two such spectra are presented. In such cases, the spectra show a significant deviation from their best conventional s-wave fittings. Such dip-like features in quasiparticle DOS are not something new. Depending on the different material

systems, different physics have been associated with that in past. Particularly for the high T_c cuprates, a 'peak-dip-hump' like feature at the higher bias in the tunneling spectra were reported by multiple groups [1–3]. Such features are generally associated with strong coupling effect and higher order symmetry in the superconducting order parameter as a consequence of bosonic excitation [1, 4]. However, counter arguments were also proposed explaining such dips as a mere consequence of the superposition of peaks and humps in the DOS [3]. Such non-BCS features are reported [5] in low T_c superconductors also where chiral pairing is predicted in the order parameter [6, 7]. We also notice that some spectra (like Fig. 4.3.1(f) in the main chapter) we probed on the surface of RuB_2 indeed resemble a partially open nodal gap. However, most of the spectra we probed on different points on the sample surface have a very clean 'U'-shaped, fully open gap. Within the limitation of our tunneling spectroscopic data (and also the already reported superconducting properties of this material), we could not confirm and specify a higher order symmetry in RuB_2. Nevertheless, as our analysis is primarily focused on the multiband mechanism, I would explain in the next section one situation where such dip-like feature can be theoretically reproduced considering two gaps (both s-wave).

4.B Further Modifications in the Multiband Model

From our spectral analysis so far, we observed the following three features for RuB_2 which warrant further discussion.

- For RuB_2, we also found some spectra which could be well explained by the single gap model. In comparison, for AuBe, we found that two gaps were necessary to explain almost each and every spectrum.
- Here, the extracted values of Δ_1 and Δ_2 vary from one spectrum to another under two-gap analysis. In comparison, for AuBe, Δ_1 and Δ_2 were very consistent (and only their relative contributions varied) throughout all the spectra probed.
- There is a dip-like spectral feature at higher bias which is prominent for some

spectra but not for others.

Next, I will briefly describe two possible modifications to our previously used 'two-gap model', one from a theoretical perspective and another completely from the empirical ground, both addressing the above-mentioned issues.

4.B.1 Introduction of Inter-band Scattering

The two-gap model (in spirit of the theory proposed by Suhl, Matthias, and Walker [8]) we have used so far to analyse our data, only considers the inter-band tunneling of quasiparticles. Though this model was independently proposed and later became popular within the physics community, a similar theoretical framework was also proposed by Moskalenko [9] at the same time. More complicated effects like intraband or interband scattering of quasiparticles, k-selective interband tunneling of Cooper pairs, etc. were not taken into account in both of these initial models. The 'Suhl-Matthias-Walker model' was extensively used afterwards and modified in occasions where it could not explain the experimental data. The interband scattering of quasiparticles by impurities was introduced in the tunneling DOS by Schopohl and Scharnberg [10] in the context of Niobium. Bussmann-Holder *et al.* [11] extended the model introducing order parameters with different symmetries and strong electron-phonon coupling to explain the enhancement in T_c. Nicol and Carbotte [12] used Eliashberg theory and discussed a series of thermodynamic quantities (including energy gap) in the light of a two-band model. Compared to the previous empirical model proposed by Bussmann-Holder *et al.* [11], Kogan et al. [13] proposed a self-consistent two-band model based on Eilenberger weak-coupling formalism. Particularly relevant for us, in the context of SIS and SIN junction tunneling, Noat *et al.* [14] used the basic model proposed by Schopohl and Scharnberg [10], and also discussed a k-selection mechanism. They introduced a correction term in each gap, which originates from the other band via interband scattering. However, there are two major issues with such models. First, the theoretical works were done in the context of almost always MgB_2 (rarely on Nb or $NbSe_2$ as well) where the gap was already reported multiple times in the past based on different spectroscopic methods. Second, such models are generally coupled equations and deal with a large number of parameters. In light of Ref. [14],

here I will discuss a basic two-gap model incorporating interband scattering. If the two interband scattering frequencies corresponding to the two bands are Γ_{12} and Γ_{21} respectively, the gaps in the two respective bands are modified as:

$$\begin{aligned}\Delta_1(E) &= \frac{\Delta_{01} + \Gamma_{12}\Delta_{02}/\sqrt{\Delta_{02}^2 - (E - i\Gamma_{21})^2}}{1 + \Gamma_{12}/\sqrt{\Delta_{02}^2 - (E - i\Gamma_{21})^2}} \\ \Delta_2(E) &= \frac{\Delta_{02} + \Gamma_{21}\Delta_{01}/\sqrt{\Delta_{01}^2 - (E - i\Gamma_{12})^2}}{1 + \Gamma_{21}/\sqrt{\Delta_{01}^2 - (E - i\Gamma_{12})^2}}\end{aligned} \tag{4.1}$$

These are two coupled equations reflecting that the gap of one band is expected to be affected by that in the other band as if through a "proximity effect" in the momentum space. With such modification due to interband scattering, the modified quasiparticle excitation spectrum corresponding to the jth band can be written as:

$$N_{sj}^{mod}(E) = N_j(E_F) Re\left(\frac{|E - i\Gamma_j|}{\sqrt{(E - i\Gamma_j)^2 - \Delta_j^2}}\right) \tag{4.2}$$

and consequently the total density of states will be $N_s^{mod}(E) = \sum_{j=1,2} N_{sj}$.

Some immediate consequences of this model are following. When both Γ_{12} and Γ_{21} are large for a given k-direction, the two gaps may seem to merge, thereby displaying a single-band like spectrum. This may explain why we found some spectra on RuB_2 which could be satisfactorily fitted with a single-gap model. On the second note, as it can be seen from the above expressions, the magnitude of the gaps Δ_1 and Δ_2 at a constant energy are not constant (i.e. Δ_{01} and Δ_{02}), rather they can vary depending on different combinations of the values of the four parameters Δ_{01}, Δ_{02}, Γ_{12} and Γ_{21}. This can explain why using two-gap analysis we found different pairs of gap values for various spectra probed on different points on the sample surface. And most importantly, as it can be seen in Fig. 4.B.1(a), such a model can also reproduce a pair of very prominent dip-like features at higher bias

(blue line). However, there are two major reasons why we could not use this model to explain our experimental spectra. First, to reproduce the dip-like feature, the required values of the two gaps need to be widely separated in the energy scale, and that does not agree with our observation [15] as well as the already reported [16] values of two gaps for RuB_2. Second, the simulated spectrum based on such model can never explain a finite state at zero bias, while in all our experimental spectra, $(dI/dV)_{V=0} > 0$. Non zero DOS at zero bias can only be explained if artificial Dynes [17] broadening parameters (Γ_j) are used for each band as was done in our initial basic two-gap model. For comparison, a simulated spectrum (red line) based on that model is also shown in Fig. 4.B.1(a), which can also produce the dip-like feature at higher bias but not as prominent as the modified model.

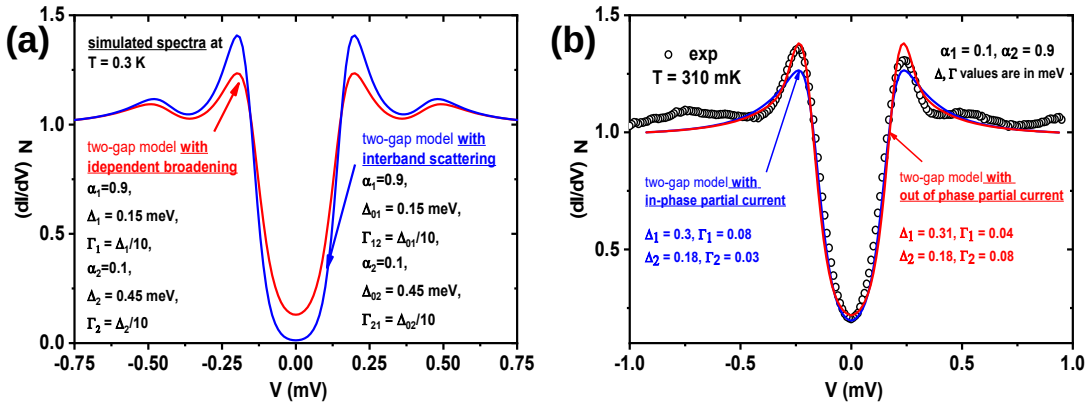

Figure 4.B.1: **(a)** Two simulated spectra at $T = 0.3$ K reproducing dip like features under two different 'two-gap' models, one without and the other with the inter-band scattering.**(b)** Better fitting of the data with a 'two-gap model' incorporating out of phase partial currents compared to the usual 'two-gap model' used previously for the analysis.

4.B.2 Introduction of a Phase-factor

So far we have considered that the total current I (and hence the differential conductance dI/dV) is a simple algebraic sum of the two partial currents I_1 (dI_1/dV) and I_2 (dI_2/dV). In that case, the two components of current, the contributions of which are coming from two different bands, are considered in phase with each

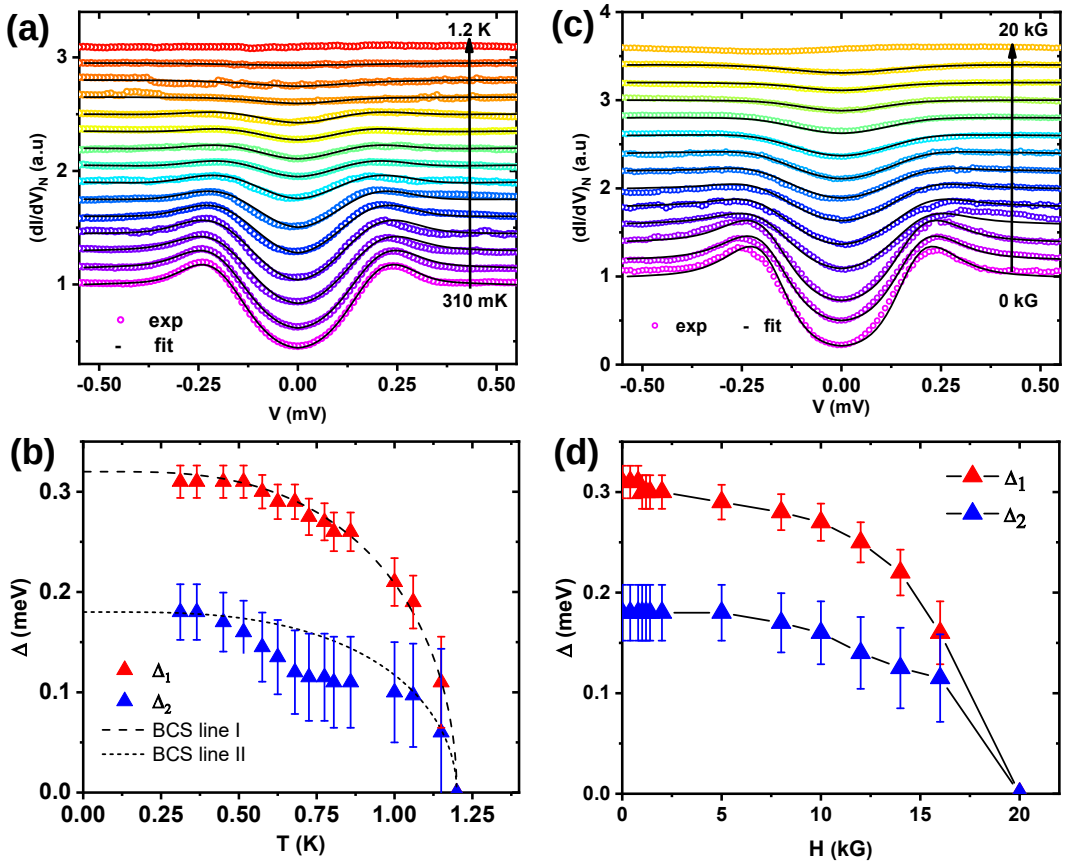

Figure 4.B.2: **(a)** Temperature (T) and **(c)** the field (H) dependence of the spectrum presented in Fig. 4.B.1(b) with the 'two-gap' fitting considering out of phase partial current. **(b)** and **(d)** The corresponding T and H dependence of the two gaps, respectively.

other. In a more generalized situation, and purely on an empirical ground, the total current can be assumed to have the following form:

$$I(V) = \alpha_1 I_1\left(\Delta_1, \Gamma_1, V\right) + \alpha_2 e^{i\phi} I_2\left(\Delta_2, \Gamma_2, V\right) \tag{4.3}$$

where ϕ is the phase difference between the two components. If we use this model to analyze the same spectra we have analyzed before, it gives a better fitting than the previous model. In Fig. 4.B.1(b), the best possible fitting with this new model (considering out-of-phase situation, i.e., $\phi = \pi$) is shown in comparison with

the old 'two-gap' model (in phase situation, i.e. $\phi = 0$) for a spectrum. This is the same spectrum which was used for both T and H dependence in Figs. 4.3.2, 4.3.3, and 4.3.4 of the main chapter, before. In Fig. 4.B.2(a) (and (c)), we revisited the same T dependence (and H dependence) of the spectra we presented in Fig. 4.3.2 (and Fig. 4.3.3 before), in light of this new model. It is clear that the simulated spectra fit perfectly with the experimental one and the deviation between them, particularly at higher bias just above the coherence peaks are significantly reduced. Most importantly, as can be seen in Fig. 4.B.2(b) and (d), both the extracted gaps are well resolved throughout the T and H range. It is interesting to note, Δ_2 still shows a non-BCS 'kink-like' feature in its T dependence, but now we know the reason behind that. Due to moderate interband scattering beyond 0.75 K, Δ_2 changes its path and tends to merge with Δ_1 where the latter one otherwise follows more or less a clean BCS line. The H dependence of both gaps shows a type-II like behavior, which was also our conclusion from previous fittings.

4.C Further Discussion on High $H_{c(l)}$

This discussion is relevant to our experimental observations on superconducting RuB_2 as well as superconducting AuBe. In the third chapter (Section 3.3.7), I mentioned that the local critical field ($H_{c(l)}$) of AuBe, at which the features (like the gap) associated with superconductivity disappear is $\sim$ 17 kG [18]. This value is orders of magnitude higher than the bulk critical field H_c ($\sim$ 300 G) reported earlier for AuBe [19, 20]. In the preceding chapter (Section 4.3.6), we encountered a similar situation where $H_{c(l)} \sim$ 20 kG [15] but the reported $H_c \sim$ 100 G only [16] for RuB_2. In both cases, our spectroscopic measurements indicate that the superconducting energy gaps survive above the bulk H_c and disappear at a much higher critical field. In the respective sections of the main chapters, we already discussed it and mentioned that such enhancement of H_c is not uncommon in the scientific literature. However, the question remains: What is the possible reason behind such surface-bulk difference in superconductivity for these materials? In the following sections, we will try to find answers to this question, within our capacity.

4.C.1 Possibility of a Mixed State

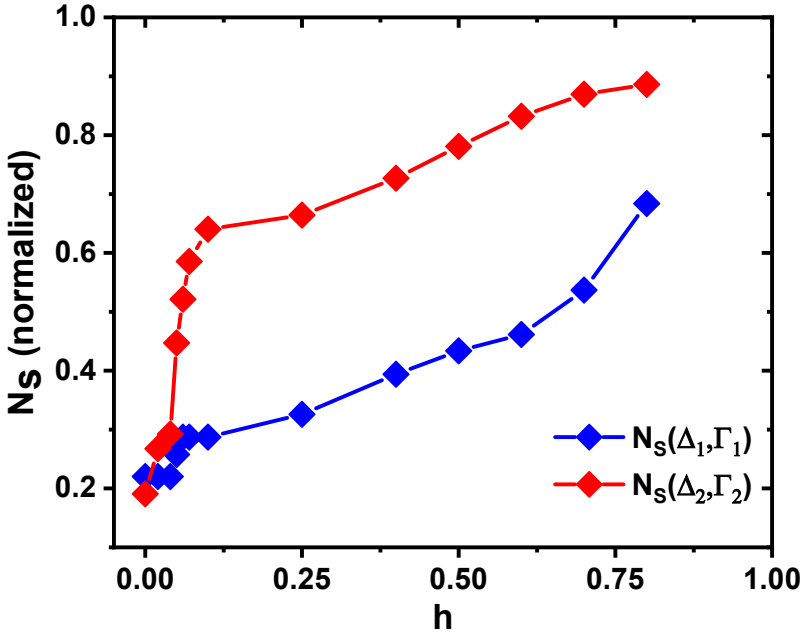

Figure 4.C.1: In arbitrary unit, zero-bias density of states corresponding to two different bands in RuB_2 as a function of reduced magnetic field $h = H/H_{c(l)}$.

We performed STS measurements on another superconducting phase of the Ruthenium-Boron compound, Ru_7B_3, the details of which [21] we will discuss in the next chapter. Interestingly, Ru_7B_3 neither have shown any signature of multiband superconductivity nor any enhanced spectral/local $H_{c(l)}$ compared to bulk H_c. On the other hand, we found evidence of both multiband superconductivity and enhanced spectral/local $H_{c(l)}$ (compared to bulk H_c) in AuBe and RuB_2. The simultaneous evidence of multiband superconductivity and high spectral/local $H_{c(l)}$ encourages us to investigate any specific correlation between them. The multiband mechanism proposed by Koshelev and Golubov [22], as we found, gives an interesting perspective in this context.

A larger vortex core size corresponds to the band forming the smaller gap. This is the general property of a two-band superconductor in its mixed state within the theory developed by Koshelev and Golubov [22]. This yields two different field

scales for the two bands where the gaps are opening. Consequently, one band is expected to attain its normal state density of states at a smaller magnetic field than the other. This difference can be directly correlated with the diffusion constants of the two bands. In order to verify this effect in RuB_2, we have calculated the magnetic field dependence of the density of states for the respective bands using the parameters obtained from the above fitting (in Section 4.B.2 before) and by using the formula for $N_{sj}(E)$ described earlier (Eqn. 3.3 in the third chapter). As shown in Fig. 4.C.1, N_{s1} sharply rises at a smaller field and then saturates, while N_{s2} rises slowly and never saturates. From the visual interpretation, this result can be compared with the experimental results on another multiband superconductor, MgB_2, as reported by Eskildsen *et al.* [23] It can be explained by the ratio of the diffusion constants ~ 0.2 in the proposed model [22]. For AuBe, we also observed a similar result (see Section 3.C in the previous appendix for details), except that there the result can be compared with the situation where the ratio of the diffusion constants is 1 in the proposed model [22]. In both cases, our results support the idea that a mixed state dictates the behaviour of the spectra. Therefore, we surmise that, between the bulk H_c and the local $H_{c(l)}$, superconducting RuB_2 and superconducting AuBe exist in their respective mixed states.

To note, all the theoretical works discussed above were done in the context of MgB_2. The model developed by Koshelev and Golubov [22] had its limitations, too, as it assumed a large Ginzburg-Landau parameter (κ) (which serves the purpose for MgB_2 where the reported $\kappa \geq 10$ [22]). In contrast, the reported κ of AuBe and RuB_2 are way too smaller [16, 20, 24]. Hence, understanding the origin of the mixed state when the bulk of the system behaves like a type-I superconductor demands the development of a two-band theory specific to RuB_2 and AuBe in the magnetic field. In some recent theoretical works [25, 26], an intertype domain between type-I and type-II was proposed, accompanied by its detailed evolution with band parameters. The calculations are particularly interesting for multiband superconductors like borides with low κ.

4.C.2 Possibility of Surface Superconductivity

The mixed state, as we discussed earlier, is usually seen in an applied field close to H_c, but our data and argument speak otherwise. It is also true that in the case of a pure type-I superconductor, the mixed state makes no sense. In such a situation, however, another possibility can explain the high $H_{c(l)}$ beyond bulk H_c. That is 'surface superconductivity' [27, 28], which survives up to a third critical field H_{c3}. We indeed have considered that possibility, and the reason we have eliminated that is the following. First of all, in our present set-up, the magnetic field was maintained perpendicular to the sample surface throughout the experiment. In such a situation, H_{c3} coincides with H_{c2} ($=\sqrt{2}\kappa H_c$), and ideally, there is no surface superconducting state [28–30]. However, one can argue that the gap is probed locally in STM, and we used grainy polycrystalline sample surfaces. Hence, the exact perpendicular orientation of the field with the particular crystallite surface being probed may not be guaranteed. Even considering such a situation, H_{c3} can achieve a maximum of only 1.7 H_{c2} ($=2.4\kappa H_c$) for a field parallel to the crystallite surface [28–30]. As we found our local critical field $H_{c(l)}$ way higher (up to $\sim$ 50 times for AuBe and $\sim$ 200 times for RuB_2) than the reported bulk H_c, we can safely ignore the possibility of surface superconductivity in our present context.

4.C.3 Other Possibilities

In restricted geometry (under surface-sensitive measurements or in nanostructured forms), a superconductor can show 10 to 100 times higher critical field compared to its bulk. The followings are a few examples. Pb is known to be a conventional type-I superconductor with T_c = 7.2 K and $H_c \approx 0.08$ T in bulk [31]. However, from Andreev reflection spectroscopy on Pb substrate by Pb tip, the superconductivity was reported to survive in the field above twice of this bulk H_c [32]. When the superconducting state is trapped under a point contact of Pb and a normal metal, the upper critical field (H_{c2}) was seen to increase up to several Tesla on the surface [33]. Pb nanoparticles (of 6 nm size and $\sim$ 6 K T_c) were found to be extremely insensitive to the applied magnetic field as high as 9 T [34]. It was also reported that, in nanowire form Pb becomes type-II superconductor with H_{c2} exceeding 15 T [35]. To give another example, Pure Nb is a conventional type-II

superconductor with bulk $T_c = 9.26$ K and thermodynamic $H_c \approx 0.2$ T [36]. When mechanically broken Nb tips (sufficiently sharp to produce atomic resolution STM image on Au surface) were used to form SIN or SIS junctions, the T_c and the superconducting gap matched well with the bulk values [37]. But, the enhanced critical field was reported to be as high as 1 T, and such enhancement was attributed to a size effect at the tip apex. In light of the above observations, a possibility can naturally come to our mind in explanation of the high $H_{c(l)}$ we observed in AuBe and RuB_2. In both cases, the materials we used were polycrystalline ones. Hence, the grains on the surface may be decoupled due to insulating grain boundaries and act as nanoparticles. We ensured pristine surfaces by reverse-sputtering the sample surface in situ in a vacuum each time before our STM/S experiments. However, the possibility of such decoupling due to insulating grain boundaries (of vacuum) can not entirely be ignored.

Pure Ta is a conventional type-I superconductor in clean limit [38]. However, introducing impurities (like N) or structural defects (like vacancies or dislocations) can decrease the coherence length ξ, increase the penetration depth λ of the system, and effectively convert Ta to a type-II superconductor in its dirty limit [38–43]. Similar arguments can be drawn in explaining the type-II-like magnetic field dependence observed in AuBe and RuB_2, where the grainy surfaces of polycrystalline materials were studied. Apart from elemental superconductors, the systemic dependences of the critical field on the surface treatments were also reported in alloys like In-Bi [44], In-Tl [45], Ta-Nb [46] etc., where the surface nucleation fields were found to be enhanced with surface imperfections. Such observations can be relevant in our context too.

Bibliography

[1] Yannick DeWilde, Nobuaki Miyakawa, Prasenjit Guptasarma, Maria Iavarone, 1 L Ozyuzer, John F Zasadzinski, Pierom Romano, David G Hinks, C Kendziora, George W Crabtree, et al. Unusual strong-coupling effects in the tunneling spectroscopy of optimally doped and overdoped $Bi_2Sr_2CaCu_2O_{8+\delta}$. *Physical Review Letters*, 80(1):153, 1998.

[2] L Ozyuzer, JF Zasadzinski, and N Miyakawa. Tunneling spectra and superconducting gap in $Bi_2Sr_2CaCu_2O_{8+\delta}$ and $Tl_2Ba_2CuO_{6+\delta}$. *International Journal of Modern Physics B*, 13(29n31):3721–3724, 1999.

[3] A Mourachkine. Origin of dips in tunneling dI/dV characteristics of cuprates. *Physica C: Superconductivity*, 460:956–957, 2007.

[4] JF Zasadzinski, L Coffey, P Romano, and Z Yusof. Tunneling spectroscopy of $Bi_2Sr_2CaCu_2O_{8+\delta}$: Eliashberg analysis of the spectral dip feature. *Physical Review B*, 68(18):180504, 2003.

[5] Anshu Sirohi, Shekhar Das, Prakriti Neha, Karn S Jat, Satyabrata Patnaik, and Goutam Sheet. Low-energy excitations and non-BCS superconductivity in $Nb_x{-}Bi_2Se_3$. *Physical Review B*, 98(9):094523, 2018.

[6] Takehito Yokoyama, Christian Iniotakis, Yukio Tanaka, and Manfred Sigrist. Chirality sensitive effect on surface states in chiral p-wave superconductors. *Physical Review Letters*, 100(17):177002, 2008.

[7] Yasuhiro Asano, Alexander A Golubov, Yakov V Fominov, and Yukio Tanaka. Unconventional surface impedance of a normal-metal film covering a spin-

triplet superconductor due to odd-frequency Cooper pairs. *Physical Review Letters*, 107(8):087001, 2011.

[8] H Suhl, BT Matthias, and LR Walker. Bardeen-cooper-schrieffer theory of superconductivity in the case of overlapping bands. *Physical Review Letters*, 3(12):552, 1959.

[9] VA Moskalenko. Superconductivity in metals with overlapping energy bands. *Fiz. Metal. Metalloved*, 8(503513):2518–2520, 1959.

[10] N Schopohl and K Scharnberg. Tunneling density of states for the two-band model of superconductivity. *Solid State Communications*, 22(6):371–374, 1977.

[11] Annette Bussmann-Holder, Roman Micnas, and Alan R Bishop. Enhancements of the superconducting transition temperature within the two-band model. *The European Physical Journal B-Condensed Matter and Complex Systems*, 37(3):345–348, 2004.

[12] EJ Nicol and JP Carbotte. Properties of the superconducting state in a two-band model. *Physical Review B*, 71(5):054501, 2005.

[13] VG Kogan, C Martin, and R Prozorov. Superfluid density and specific heat within a self-consistent scheme for a two-band superconductor. *Physical Review B*, 80(1):014507, 2009.

[14] Yves Noat, Tristan Cren, François Debontridder, Dimitri Roditchev, W Sacks, Pierre Toulemonde, and Alfonso San Miguel. Signatures of multigap superconductivity in tunneling spectroscopy. *Physical Review B*, 82(1):014531, 2010.

[15] Soumya Datta, Aastha Vasdev, Soumyadip Halder, Jaskaran Singh, Yogesh Singh, and Goutam Sheet. Spectroscopic signature of two superconducting gaps and their unusual field dependence in RuB_2. *Journal of Physics: Condensed Matter*, 32(31):315701, 2020.

[16] Jaskaran Singh, Anooja Jayaraj, D Srivastava, S Gayen, A Thamizhavel, and Yogesh Singh. Possible multigap type-I superconductivity in the layered boride RuB_2. *Physical Review B*, 97(5):054506, 2018.

[17] RC Dynes, V Narayanamurti, and J Pm Garno. Direct measurement of quasiparticle-lifetime broadening in a strong-coupled superconductor. *Physical Review Letters*, 41(21):1509, 1978.

[18] Soumya Datta, Aastha Vasdev, Partha Sarathi Rana, Kapil Motla, Anshu Kataria, Ravi Prakash Singh, Tanmoy Das, and Goutam Sheet. Spectroscopic evidence of multigap superconductivity in noncentrosymmetric AuBe. *Physical Review B*, 105(10):104505, 2022.

[19] Alfred Amon, Eteri Svanidze, R Cardoso-Gil, MN Wilson, H Rosner, Matej Bobnar, Walter Schnelle, Jeffrey W Lynn, R Gumeniuk, C Hennig, et al. Noncentrosymmetric superconductor BeAu. *Physical Review B*, 97(1):014501, 2018.

[20] D Singh, AD Hillier, and RP Singh. Type-I superconductivity in the noncentrosymmetric superconductor BeAu. *Physical Review B*, 99(13):134509, 2019.

[21] Soumya Datta, Aastha Vasdev, Ranjani Ramachandran, Soumyadip Halder, Kapil Motla, Anshu Kataria, Rajeswari Roy Chowdhury, Ravi Prakash Singh, Goutam Sheet, et al. Spectroscopic evidence of mixed angular momentum symmetry in non-centrosymmetric Ru_7B_3. *Scientific Reports*, 11(1):1–7, 2021.

[22] AE Koshelev and Alexandre Avraamovitch Golubov. Mixed state of a dirty two-band superconductor: Application to MgB_2. *Physical Review Letters*, 90(17):177002, 2003.

[23] MR Eskildsen, M Kugler, S Tanaka, J Jun, SM Kazakov, J Karpinski, and Ø Fischer. Vortex imaging in the π band of magnesium diboride. *Physical Review Letters*, 89(18):187003, 2002.

[24] Drew J Rebar, Serena M Birnbaum, John Singleton, Mojammel Khan, JC Ball, PW Adams, Julia Y Chan, DP Young, Dana A Browne, and John F DiTusa. Fermi surface, possible unconventional fermions, and unusually robust resistive critical fields in the chiral-structured superconductor AuBe. *Physical Review B*, 99(9):094517, 2019.

[25] Alexei Vagov, AA Shanenko, MV Milošević, Vollrath M Axt, VM Vinokur, J Albino Aguiar, and FM Peeters. Superconductivity between standard types: Multiband versus single-band materials. *Physical Review B*, 93(17):174503, 2016.

[26] Mihail Silaev and Egor Babaev. Microscopic theory of type-1.5 superconductivity in multiband systems. *Physical Review B*, 84(9):094515, 2011.

[27] VL Ginzburg. On surface superconductivity. *Phys. Letters*, 13, 1964.

[28] AC Rose Innes and EH Rhoderick. *Introduction to superconductivity*. Pergamon Press, 1980.

[29] Daniel Saint-James and PG de Gennes. Onset of superconductivity in decreasing fields. *Physics Letters*, 7(5):306–308, 1963.

[30] Pierre-Gilles De Gennes and Philip A Pincus. *Superconductivity of metals and alloys*. CRC Press, 2018.

[31] HA Boorse, DB Cook, and MW Zemansky. Superconductivity of Lead. *Physical Review*, 78(5):635, 1950.

[32] José Gabriel Rodrigo, V Crespo, H Suderow, S Vieira, and F Guinea. Topological superconducting state of Lead nanowires in an external magnetic field. *Physical Review Letters*, 109(23):237003, 2012.

[33] Anshu Sirohi, Preetha Saha, Sirshendu Gayen, Avtar Singh, and Goutam Sheet. Transport spectroscopy on trapped superconducting nano-islands of Pb: signature of unconventional pairing. *Nanotechnology*, 27(28):285701, 2016.

[34] CC Yang, FC Tsao, SY Wu, W-H Li, and KC Lee. Enhanced critical magnetic field in superconducting Pb nanoparticles. *Journal of Low Temperature Physics*, 131(3):349–352, 2003.

[35] Mingquan He, Chi Ho Wong, Pok Lam Tse, Yuan Zheng, Haijing Zhang, Frank LY Lam, Ping Sheng, Xijun Hu, and Rolf Lortz. Giant enhancement of

the upper critical field and fluctuations above the bulk T_C in superconducting ultrathin Lead nanowire arrays. *ACS Nano*, 7(5):4187–4193, 2013.

[36] DK Finnemore, TF Stromberg, and CA Swenson. Superconducting properties of high-purity Niobium. *Physical Review*, 149(1):231, 1966.

[37] A Kohen, Yves Noat, T Proslier, Emmanuelle Lacaze, M Aprili, W Sacks, and D Roditchev. Fabrication and characterization of scanning tunneling microscopy superconducting nb tips having highly enhanced critical fields. *Physica C: Superconductivity*, 419(1-2):18–24, 2005.

[38] GW Webb, F Marsiglio, and JE Hirsch. Superconductivity in the elements, alloys and simple compounds. *Physica C: Superconductivity and its applications*, 514:17–27, 2015.

[39] RW Shaw, DE Mapother, and DC Hopkins. Critical fields of superconducting Tin, Indium, and Tantalum. *Physical Review*, 120(1):88, 1960.

[40] J Buchanan. The ginzburg-landau parameter of Tantalum. *Journal of Physics and Chemistry of Solids*, 26(7):1183–1184, 1965.

[41] J Auer and H Ullmaier. Magnetic behavior of type-II superconductors with small ginzburg-landau parameters. *Physical Review B*, 7(1):136, 1973.

[42] HW Weber, JF Sporna, and E Seidl. Transition from type-II to type-I superconductivity with magnetic field direction. *Physical Review Letters*, 41(21):1502, 1978.

[43] R Idczak, W Nowak, M Babij, and VH Tran. Type-II superconductivity in cold-rolled tantalum. *Physics Letters A*, 384(28):126750, 2020.

[44] HJ Fink and WCH Joiner. Surface nucleation and boundary conditions in superconductors. *Physical Review Letters*, 23(3):120, 1969.

[45] PR Doidge, Kwan Sik-Hung, and DR Tilley. Anomalous superconducting surface nucleation fields. *Philosophical Magazine*, 13(124):795–803, 1966.

[46] J Lowell. Surface superconductivity in dilute type-II alloys. *Philosophical Magazine*, 16(141):581–591, 1967.

Chapter 5

Mixed Parity Superconductivity in Ru_7B_3

In this chapter, the superconducting nature of non-centrosymmetric Ru_7B_3 is investigated. From the direct measurement of the superconducting gap through tunneling experiments, we report the existence of both s-wave (singlet) and p-wave (triplet) pairing symmetries in non-centrosymmetric Ru_7B_3. The work presented in this chapter is already published in Ref. [1].

5.1 Introduction

The attractive interaction leading to superconductivity is believed to be isotropic in momentum space, according to the BCS theory [2]. As a result, BCS superconductors' energy gaps exhibit s-wave (orbital angular momentum, l=0) symmetry. The energy gap in certain superconducting systems can become anisotropic in momentum space, exhibiting higher angular momentum symmetries such as p-wave (l=1) [3–5], d-wave (l=2) [6–8], and so on. Mixed angular momentum symmetry, where different l are mixed, has also been observed in a variety of systems [9–12]. Within the BCS formalism, the physics of such non-s-wave superconductors can not be explained. Parity is not a good quantum number when a superconductor's crystal structure lacks a centre of inversion. In theory, antisymetric spin-orbit coupling (ASOC) is possible in such a system. Bloch states with the same k

(crystal momentum) but opposite spins can have their spin degeneracy removed by ASOC. The orbital and spin angular momentums are no longer good quantum numbers in the presence of ASOC. The symmetry of the Cooper pairs cannot be restricted to either a fully even-parity singlet or an odd-parity triplet by Pauli's exclusion principle. As a result, in a non-centrosymmetric superconductor, a complex mixed angular momentum state becomes possible [13]. From the introduction as well as the third chapter of this thesis, we are already familiar about such non-centrosymmetric superconductors. I already have discussed that a non-centrosymmetric superconductors (NCS) can display unexpected behavior in their electro-magnetic properties when compared to simply *s*-wave superconductors. This is because of the unconventionality associated with such complicated angular momentum symmetry of the superconducting order parameters. For example, they might have very high Pauli limiting fields [14], helical vortex states [15], or even topologically protected states [16]. As a result of these factors, the research of non-centrosymmetric superconductors received a lot of attention [17–19] in the condensed matter physics community since the discovery of the first non-centrosymmetric superconductor $CePt_3Si$ [14, 20].

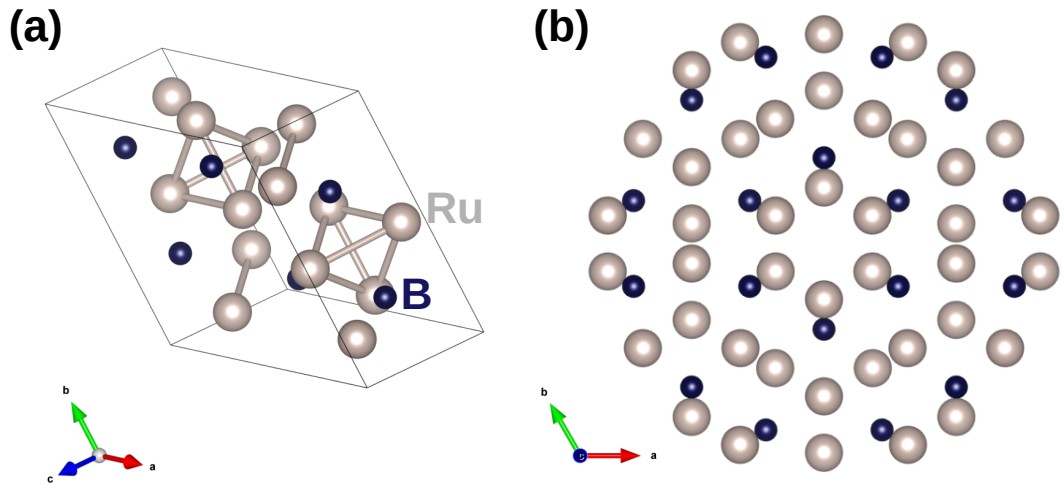

Figure 5.1.1: The crystal structure of Ru_7B_3.**(a)** One unit cell and **(b)** a view parallel to [001] direction along which the inversion symmetry is broken.

T_7B_3 (T: transition metal), which belongs to the space group $P6_3mc$ and the

cyclic crystallographic class C_{6v}, is one such promising group of materials. The link between superconductivity and broken inversion symmetry inside the crystal structure with $4d$ and $5d$ elements of such materials holds promise in our current situation. Aronsson [21] originally reported the crystal structure of Ru_7B_3 in 1959, and it was later confirmed by others [22, 23]. Matthias [22] reported superconductivity in Ru_7B_3 just two years later. Morniroli [24], some three decades later, was the first to notice the absence of inversion symmetry in its crystal structure. In Fig. 5.1.1, the crystal structure of Ru_7B_3 is shown [21, 25]. There is no inversion symmetry in the cyclic crystallographic class C_{6v}. The basal plane is hexagonal from the standpoint of the crystal structure, and the centre of Boron sublattice displaces the centre of Ruthenium sublattice along the c-axis [21]. In Ru_7B_3, anomalous superconductivity caused by Rashba-type ASOC becomes a possibility due to the broken inversion symmetry. The singlet-triplet mixed order parameter can strongly perturb the electronic states surrounding the vortex core [15] in this case, and the superconducting energy gap may have an observable node that would otherwise be barred by symmetry. On the other hand, around Fermi energy, the Ru $4d$ state dominates over the B $2p$ state in the electronic band structure [26]. It was also seen that all bands are doubly degenerate, with ASOC spin splitting up and down bands to lift the degeneracy. As described in the previous chapter of this thesis, our tunneling spectroscopic data revealed the coexistence of two superconducting gaps and their peculiar field dependency in another superconducting phase of the Ruthenium-Boron complex RuB_2 [27]. As a result of that exciting discovery and the potential indicated above, we chose Ru_7B_3 as our next candidate for high-resolution spectroscopic study.

Several independent investigations on Ru_7B_3 have been reported so far in search for detailed superconducting properties in this material. Based on magnetic susceptibility, resistivity, and specific heat measurements, the reported onset transition temperature (T_c^{onset}) for single crystal [28, 29] and polycrystal samples [26] are around 2.6 K and 3.3 K, respectively. The higher temperatures in polycrystals were linked to the vacancies in the crystal caused by the loss of Boron during the growing process [29]. Kase and Akimitsu [28] reported 0.38 meV zero temperature energy gap (Δ_0) for single crystal Ru_7B_3 based on magnetization and specific heat

data. Fang *et al.* [26], on the other hand, reported $\Delta_0 = 0.5$ meV when working on polycrystal. As we will see in a moment, this large discrepancy in order parameter magnitude will be relevant in our spectroscopic measurements too. Kase and Akimitsu [28] estimated two important ratios $\Delta C_e/\gamma_n T_c$ (and $2\Delta_0/k_B T_c$) as 1.4 (and 3.3), respectively, while Fang *et al.* [26] estimated 1.3 (and 3.6) in comparison to weak-coupling BCS limits of 1.43. (and 3.52). Both groups used their independent specific heat data to extract the Sommerfeld parameter $\gamma(H)$ and argued about a dominant fully gapped *s*-wave channel. After conducting their respective experiments on single crystal and/or polycrystal, the authors concluded that they found no indication of the non-centrosymmetric influence on the superconducting characteristics of Ru_7B_3. In contrast, anisotropic gaps were clearly visible from specific heat measurements in other non-centrosymmetric superconductors like Li_2Pt_3B and $CePt_3Si$ [30, 31]. Kase and Akimitsu justified this absence by pointing to the Ru $4d$ electron's weak electron correlation and its minimal contribution to the Fermi surface as two probable reasons [28]. Fang *et al.* made a similar argument, claiming that the mass of Ru isn't heavy enough to generate a strong ASOC [26] in Ru_7B_3. Cameron *et al.* [32] recently carried out small-angle neutron scattering on Ru_7B_3 and found that the orientation of the vortex lattice in this material is highly influenced by the history of the applied magnetic field. As we will see soon, this last report will be incredibly relevant to our investigation. For the time being, I will save this topic for a more in-depth discussion later.

5.2 Experimental Methods

The single crystals used for our measurements showed a bulk superconducting transition at 2.6 K [1]. The scanning tunneling spectroscopy (STS) experiments were performed in the Unisoku system with RHK R9 controller, inside the ultra-high vacuum (UHV) cryostat at $\sim 10^{-10}$ mbar pressure. The lowest temperature down to which the measurements were performed was 300 mK. The STM is equipped with the superconducting solenoid capable of producing a magnetic field up to 11 T. Since the single crystals could not be cleaved using the standard cleaving technique (optimized for layered materials only), we cleaned the surface by reversed sputtering for 30 minutes with Argon (Ar) ion *in-situ* inside an integrated UHV

preparation chamber. Following that, we immediately transferred the sample to the scanning stage at low temperature. The Tungsten (W) tip, which was prepared outside by electrochemical etching, was also cleaned in UHV by bombarding it with a high-energy electron-beam.

5.3 Two Types of Spectra

After finding a relatively clean surface area, we performed local tunneling spectroscopy bringing the tip at several points on that surface, especially at the central parts of different grains. In Fig. 5.3.1, four such representative spectra are shown, which were recorded at the lowest temperature ($\sim$ 310 mK) and different random points on the sample surface. All dI/dV vs V spectra are normalized to the conductance at $\sim$ 2 mV around which the conductance remains flat. A pair of coherence peaks symmetric about $V = 0$ is visible for every spectrum and in the valley between those peaks, dI/dV approaches zero. It is interesting to note that the spectra we have, can be distinctively divided into two categories. The first type (Fig. 5.3.1(a) and (b)) has coherence peaks at lower bias and the spectra are less steep and deep in the in-between valley. The second type (Fig. 5.3.1(c) and (d)) has coherence peaks at relatively higher bias and the spectra have a higher slope and depth within that. To analyse further and have a quantitative estimation of Δ, in the next section, I will compare each spectrum with a numerically generated one, using the expression for tunneling current within a single band s-wave model [2].

5.4 Analysis Under s-wave Model

We analysed the experimental spectra with the usual expressions of tunneling current $I(V)$ and the normalised superconducting DOS $N_s(E)$ [33] (Eqn. 3.1 and Eqn. 3.2, respectively, from the third chapter). In this model, Δ is taken to be a constant isotropic parameter for conventional s-wave superconductor. The theoretical plots thus generated are shown as red lines over the experimental data points (black circles) in Fig. 5.3.1. Two important observations are the following.

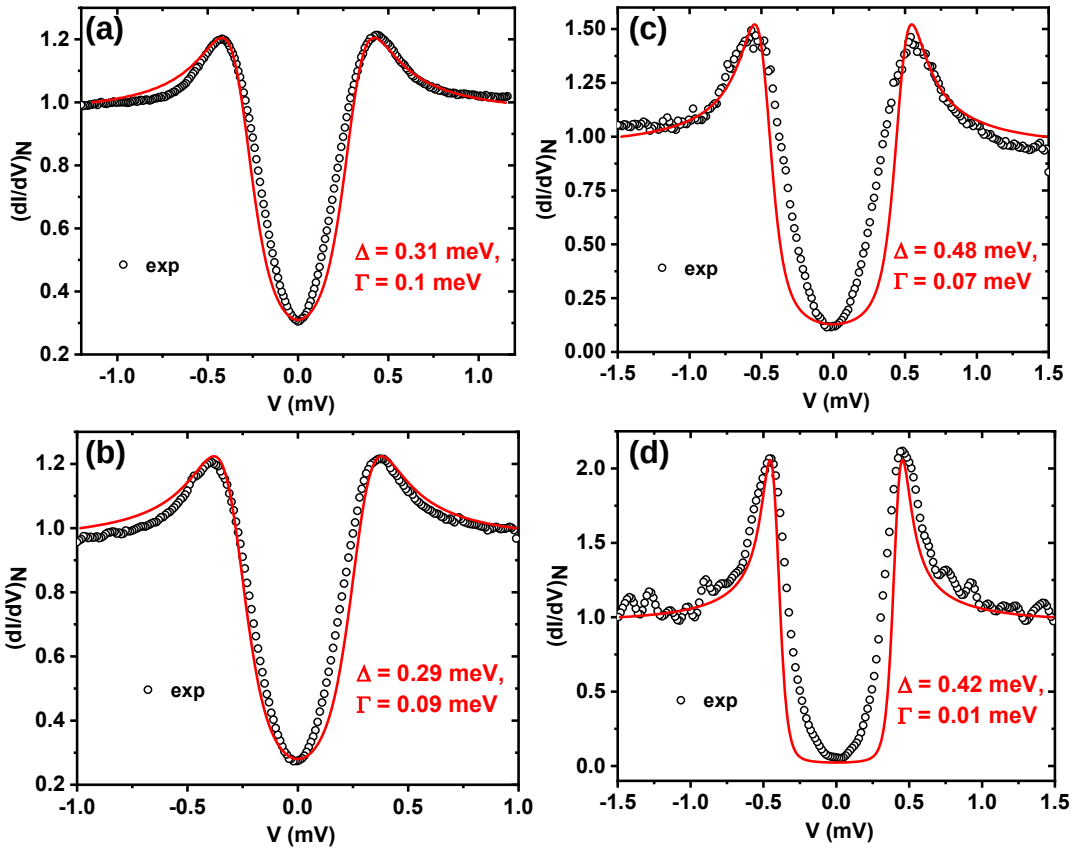

Figure 5.3.1: Two types of tunneling spectra (black circles) probed on different points on the surface of Ru_7B_3 and corresponding best fits under single gap *s*-wave model (red lines). Spectra in **(a), (b)** showing good agreement with the model but spectra in **(c), (d)** showing significant mismatch.

Spectra of the first type (Fig. 5.3.1(a) and (b)) provides $\Delta \sim 0.3$ meV while that of the second type (Fig. 5.3.1(c) and (d)) provides the value ~ 0.45 meV for the same. Moreover, while the first type of spectra shows a reasonably good fitting to the single gap *s*-wave model we used, the second type demonstrates a significant departure from that. Visually, the second type of spectra looks more 'V'-shaped compared to their theoretical 'U'-shaped best fittings, and such 'V'-shaped spectrum is a typical characteristic of a nodal/line superconductor with higher order symmetry in the gap. Therefore, our observation, though does not prove at this stage, provides the first indication of higher order symmetry in the order parame-

ter. I will later discuss more elaborately about this discrepancy while introducing further modifications in the fitting model. For now, as we already have a number of spectra where the conventional s-wave model worked, rather than jumping to any advanced model, I will first explore what information we can obtain within our present analysis. For that purpose, we will begin with the temperature and magnetic field dependence of the symmetrized experimental spectra belonging to both types.

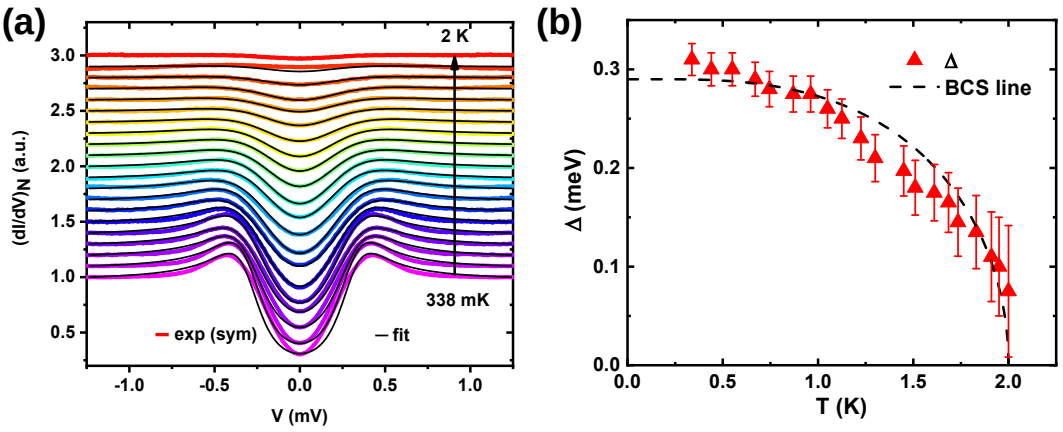

Figure 5.4.1: **(a)** Temperature (T) dependence of a typical spectrum (symmetrized) of the first type (colour lines) with corresponding theoretical fits (black lines) under pure s-wave model. **(b)** Evolution of Δ with T, extracted from the plot (a) along with ideal BCS trend for Δ.

The spectrum represented before in Fig. 5.3.1(a) belongs to the first type and fits reasonably well with a single 's-wave' gap. A closer inspection, however, reveals that there is a small discrepancy between the experimental data and the 's-wave' model spectrum. We investigated the evolution of this spectrum with temperature and represented the result in Fig. 5.4.1(a). Considering the best fit under s-wave model, the temperature dependence of Δ approximately followed the BCS prediction. However, there are two interesting points to note.

- As can be seen from Fig. 5.4.1(a), the departure of the experimental spectrum from the s-wave model rapidly decreased with increasing temperature. we found that at $\sim$ 750 mK the discrepancy almost disappeared.

- According to BCS theory [2], it is expected that the magnitude of the gap should vary negligibly at lower T. However, as can be seen from Fig. 5.4.1(b), Δ decreases almost monotonically with increasing T from the very beginning.

These observations provide the second indication for the possibility of a mixed angular momentum symmetry in the order parameter where the amplitudes corresponding to different l vary differently with temperature. Later in this chapter, we will revisit this same set of temperature-dependent data and analyse it under a model which considers mixed angular momentum symmetry.

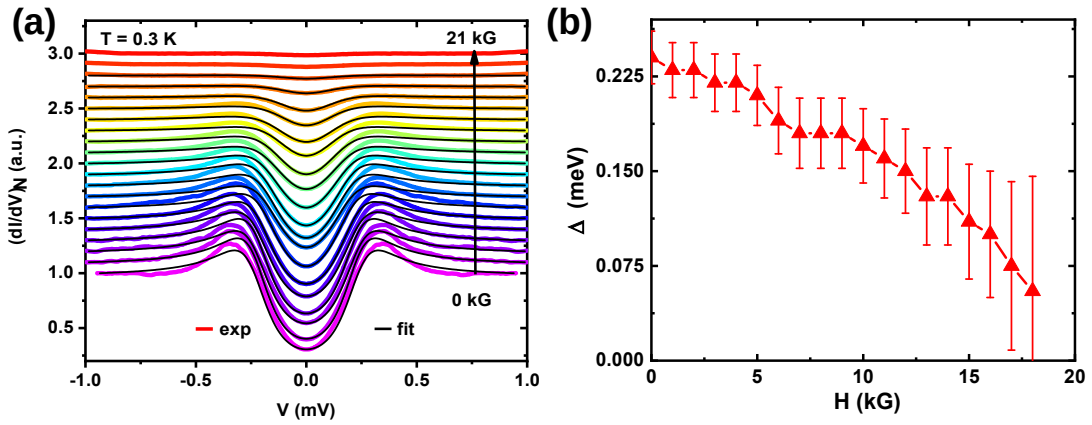

Figure 5.4.2: **(a)** Magnetic field (H) dependence of another spectrum (symmetrized) of the first type (colour lines) with corresponding s-wave theoretical fits (black lines). **(b)** Evolution of Δ with H, extracted from the plot (a). Temperature is kept $\sim$ 310 mK throughout measurements.

Next, we observed the magnetic field dependence of another spectrum of the first type. The results are demonstrated in Fig. 5.4.2. Similar to the results of the previous T dependence, we found that the spectra deviate appreciably from 's-wave' theoretical curves at low fields but match well at higher field ($>$ 10 kG). Thus, it can be concluded that both increasing the temperature and increasing the applied external magnetic field has an analogous effect of bringing Ru_7B_3 from a mixed state to a pure singlet state. Our observation is in good agreement with the reported H_{c2} 17.2 kG for Ru_7B_3 in (001) direction [28] *aka* c-axis in our case.

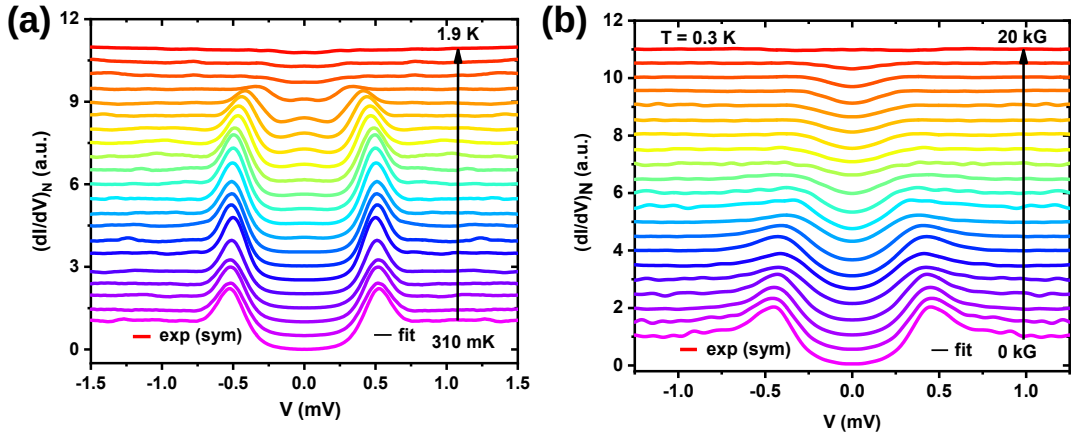

Figure 5.4.3: **(a)** Temperature and **(b)** magnetic field dependence of two spectra (symmetrized) of second type where s-wave fittings do not work.

Up to this point, we only discussed spectra of the first type, i.e., those which are comparatively in better agreement with the conventional s-wave model except at very low temperature. Now we will focus on spectra of the second type, which are way too different for such analyses yet worth mentioning because of some exciting features and consistency with the previous observations. In Fig. 5.4.3(a), the temperature dependence of a typical spectrum of the second type is demonstrated. The initial spectrum at the lowest T is the same one represented in Fig. 5.3.1(d). An interesting observation from this T dependence is that, at T $\sim$ 740 mK, a small zero-bias conductance peak (ZBCP) appeared. It became increasingly pronounced up to $\sim$ 1370 mK and then started fading until it, along with other prominent spectral features, gradually disappeared at 1.9 K. There can be multiple possible reasons for which a tunneling spectrum can show such ZBCP features. In the next section, we will discuss more elaborately about such reasons. As of now, it will be relevant, fair, and consistent to mention that, for a superconductor with higher order symmetry like (p or d-wave) the emergence of such a ZBCP is expected when the interface normal and the lobe-direction of the superconducting gap maintain an acute angle between them [34–37]. Since the surface of Ru_7B_3 had crystallites with random orientations and the tip was engaged randomly at different points, this condition could naturally be satisfied sometimes. This is the third indication behind the possible existence of the higher order symmetry in

the superconducting gap from our spectral investigation. We also observed the magnetic field dependence of a similar spectrum of the second type. As it can be seen in Fig. 5.4.3(b), with increasing field, the coherence peaks come closer and gradually disappear. At around 20 kG, no signature of superconductivity was found.

If we compare Fig. 5.4.3(a) with Fig. 5.4.1(a), and Fig. 5.4.3(b) with Fig. 5.4.2(a), there is an important observation to be noted. Irrespective of the probed spectrum (or the nature of the gap associated with it), the superconductivity at the surface of Ru_7B_3 is always destroying at the same temperature ($T_c^j \sim 2$ K) and magnetic field ($H_{c(l)} \sim 20$ kG). This provides a strong argument to support that the spectral variations we found from our thorough investigation were not coming from some artefacts due to defects and impurities on the surface, rather those are the manifestation of some novel superconducting behaviour itself.

5.5 Discussion on Zero Bias Conductance Peak

ZBCP can occur in tunneling spectra due to multiple reasons. The following are examples of a few such situations.

- An superconductor-insulator-superconductor (SIS) junction created between the tip and the sample when the tip (normal metal), at its bottom, picked up some atoms/molecules from the sample (superconductor) surface.
- Similar SIS junction when locally at the bottom of the tip, superconductivity is induced due to proximity of the superconducting sample below it.
- A vortex (an impurity site) trapped just under the tip.
- An Andreev bound state formed between the tip and a superconductor with higher order symmetry in its order parameter.

From the limitation of our experimental data, it is not possible to pinpoint a particular reason behind the ZBCP we probed. However, to understand the possible mechanism within our capacity, we performed the following analysis.

The simplest explanation about this feature can be that it is associated with an impurity state formed under STM tip. It only revealed itself when the temperature was high enough to allow the scattering to occur. To take this into account, we modified the equation of tunneling current following way.

$$I(V) \propto \int_{-\infty}^{+\infty} N_n(E - eV)[N_s(E) + Ip(E)][f(E) - f(E - eV)]dE \tag{5.1}$$

Where we have introduced the following Gaussian function to take care of the peak feature.

$$Ip(E) = Ae^{-\frac{E^2}{B}} \tag{5.2}$$

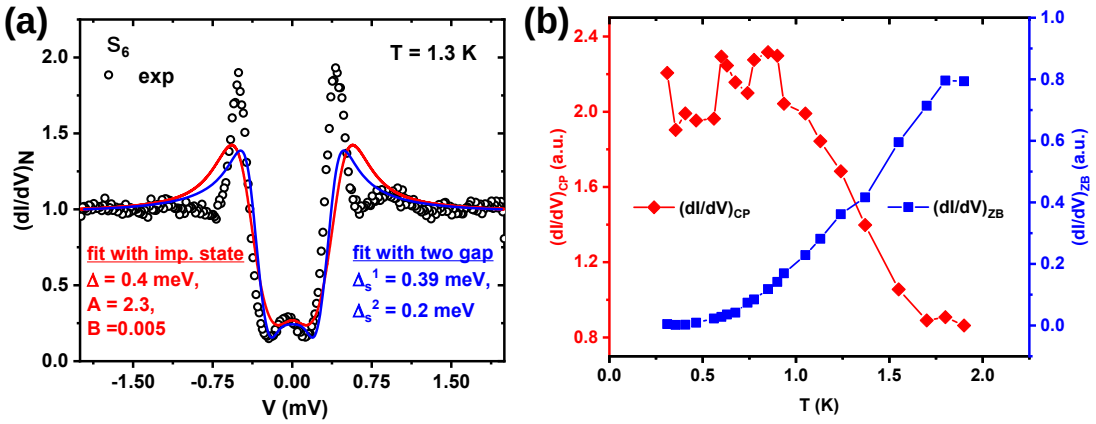

Figure 5.5.1: **(a)** The spectrum at $T = 1.3$ K (where ZBCP is pronounced) along with best fits considering i) an impurity state with BCS model (red line) and ii) 'two s-wave gap' model (blue line) with a π phase difference. **(b)** Evolution of the average coherence peak height ($(dI/dV)_{CP}$) with temperature. In the same panel using right side scale for y-axis, evolution of the zero bias conductance height ($(dI/dV)_{ZB}$) with temperature.

The parameters A and B correspond to the height and spread of such function, respectively. In Fig. 5.5.1(a), the experimental spectrum at $T = 1.3$ K from the previously discussed temperature dependence (Fig. 5.4.3(a)) is represented by black circles. Corresponding numerically generated theoretical spectrum is pre-

sented by the red line. It is needless to say, the theoretical spectrum though can produce a ZBCP, it fails to match the experimental spectrum, especially near the sharp coherence peaks. We also have substituted the Gaussian distribution function by a Lorentzian distribution function, but the fitting model remained unsuccessful.

We also have explored the possibility of two s-wave gap fitting for our spectra according to the model discussed in Section 4.B.2 in the Appendix of the 4th chapter. Interestingly, for out-of-phase scenario, that model can produce a ZBCP under specific parameter windows, and we tried to fit our spectrum with that. The blue line in Fig. 5.5.1(a) represents the best fit with such a model for the experimental spectrum. Although it gives better fitting compared to the previous model mentioned, it still significantly deviates around the sharp coherence peaks, the region where even the pure 's-wave' fit was more successful (see Fig. 5.3.1(d)).

The failure of different fitting models to explain the temperature dependent data (see Fig. 5.4.3(a)) for the spectra of the second type impelled us to concentrate on other details. We noticed that the coherence peaks in these spectra do not match with the theoretical plot because they remain significantly high compared to the later (even when the temperature was increasing). Therefore, we measured the average height of coherence peaks ($(dI/dV)_{CP}$) for each spectrum in Fig. 5.4.3(a) and plotted them against the temperature in Fig. 5.5.1(b). As it can be seen, the height of the coherence peak remains almost the same except some random fluctuations up to $\sim$ 900 mK and from that point it started to fall very sharply with temperature till the last data at 1.9 K. In the same figure, using the right-side y-axis label, we also plotted the height of zero-bias conductance ($(dI/dV)_{V=0}$) w.r.t temperature. A smooth increment with temperature can be seen here. Such a smooth increment may eliminate the possibility of a vortex passing below the tip due to thermal drag.

The above analysis and the consistency in the spectral T_c^j and $H_{c(l)}$ (irrespective of the type of the spectra) encourages us to think, whether such a feature is not from any normal impurity scattering and rather is a manifestation of some novel

superconducting behaviour itself. If the unconventional order parameter changes its sign around the Fermi surface, an Andreev bound state can reveal itself as a zero-bias conductance peak in point contact as well as tunneling spectroscopy [19]. For d-wave symmetry in the order parameter, bulk quasiparticle density of states $N_S(E) \propto |E|$. In such a situation, if the interface normal and the lobe direction of the d-wave order parameter maintain an acute angle between them, then the resulting tunneling conductance shows a zero-bias conductance peak [36, 37]. For a grainy surface like ours, probabilistically this condition is bound to be satisfied sometimes and the peak feature will occur. On the other hand, for p-wave symmetry in the order parameter, its self-consistency as well as the impurity effects play crucial roles. Both order parameter components, the dominant and the subdominant one, can be strongly suppressed near the surface and the tunneling spectra can get sufficiently modified by an increased scattering in the surface layer. As a result, the tunneling conductance spectra show a broad peak similar as d-wave though its height gets significantly reduced for a self-consistent order parameter [34, 35]. From Fig. 5.5.1(a), we can see that the ZBCP we probed look exactly like that. If we now recollect the previous indications of higher-order symmetries in the gap we have noted earlier, we can safely say that we are now in a position to explore that possibility with the required modifications in our fitting model. However, two questions still remain unanswered.

- Among the numerous possible symmetries, which one would be most relevant for the present system?
- If we have found so many indications of unconventional pairing in Ru_7B_3 from our STS investigation, why was the same undetected in the previous four reports [26, 28, 29, 32] on this material?

To search for the answers of the above two questions, we would revisit the previous reports in Ru_7B_3 once more.

5.6 Previous Indications of Unconventional Pairing

All four previously mentioned papers [26, 28, 29, 32] reporting the superconducting properties of Ru_7B_3 agreed about a conventional BCS superconductivity in this material system. However, while going through the details of these reports, we found a few ambiguities and incompleteness which warrant a further thorough investigation.

To support the dominance of isotropic fully open gap, Kase and Akimitsu [28] discussed the H dependence of $\gamma(H)$ and argued it to be linear which otherwise for an anisotropic or nodal gap should be proportional to $H^{1/2}$ according to theory [38]. However, in Fig. 6 of their article representing $\gamma(H)$ vs. H plot (wrongly denoted by T instead of H in the x axis label) the solid fitting line is not linear as demanded. A closer look will reveal that it is instead a line with a small curvature. Certainly, the experimental data can be fitted better by a 'true' linear fitting $\gamma(H) \propto H$ compared to a pure parabolic $\gamma(H) \propto H^{1/2}$ fit. Nevertheless, experimentally extracted points tend to significantly deviate from such a pure linear fit, especially at high field. The best fit would be a combination of $\gamma(H) \propto H$ and $\gamma(H) \propto H^{1/2}$ dependence, where the former has the dominance. This observation provided us the first clue that the gap of Ru_7B_3 must have an anisotropic component, however small it is, mixed with a dominant fully gaped isotropic s-wave one.

Fang *et al.* [26], on the other hand, in their independently reported study around the same time, described something minute yet interesting. In field-dependent resistive transition, they reported the appearance of a kink and the subsequent break-up of the transition curves into two parts. Two parts demonstrated significantly different sensitivity to the magnetic field and convey two entirely different values of higher critical fields (H_{c2}) of 1.1 T and 5 T, depending on the selected criterion of resistivity. For a side note, the $H_{c(l)}$ we have reported from our spectroscopic measurements ($\sim$ 2 T), as well as the H_{c2} previously reported by Kase and Akimitsu [28] (1.72 T and 1.58 T for two different current directions) fall well within this two values. While discussing the different possible reasons behind

these two remarkably different (H_{c2}), the authors [26] mentioned the following explanation as one of those. Suppose both spin singlet and triplet pairing coexist in Ru_7B_3 as expected for a standard non-centrosymmetric superconductor. In such a situation, it is possible that though the former one has a larger ratio in superfluid than the later, the later one has a significantly higher critical field. If so, such a two-step transition is normal from the resistivity data.

Inspired by the previous results from muon spectroscopy measurements performed on single crystal and polycrystalline Ru_7B_3 [39], Cameron *et al.* recently performed small-angle neutron scattering on the single crystal [32]. They probed the magnetic vortex lattice in superconducting Ru_7B_3 and reported that its orientation strongly depends on the history of the applied magnetic field. This is a striking observation because it indicates the presence of a spontaneous magnetization in the system, which in turn indicates the breaking of time-reversal symmetry (besides the broken inversion symmetry already guaranteed by the crystal structure). In such a system, the spin triplet p-wave order parameter becomes a natural possibility. However, while explaining their results from a phenomenological approach, the authors obviously took into account only the singlet component of the superconducting order parameter because the small yet possible triplet component was not confirmed hitherto by any report.

In such a case, a high-resolution energy-resolved spectroscopic study was necessary to either confirm or deny the existence of mixed angular momentum symmetry in the order parameter of Ru_7B_3 and that was exactly what we have done.

5.7 Introduction of p-wave Symmetry

The discrepancy between the experimental spectra of the second type (Fig. 5.3.1(c) and (d)) and the spectra generated theoretically within a single-band 's-wave' model, prompted us to consider other possible symmetries of the order parameter. To perform such an analysis, we modified Dyne's equation by introducing a more general expression [36] of $\Delta(\theta)$ than an isotropic Δ. The modified Dyne's equation reads as following.

$$N_s(E,\theta) \propto Re\left(\frac{(E-i\Gamma)}{\sqrt{(E-i\Gamma)^2-(\Delta' Cos(n\theta))^2}}\right) \tag{5.3}$$

Here, θ is the polar angle (w.r.t. (001) of the sample) and the integer n can be 0, 1 or 2 for s, p and d wave symmetries respectively. The expression for tunneling current is also modified to

$$I(V) \propto \int_{-\infty}^{+\infty}\int_{0}^{2\pi} N_s(E,\theta)N_n(E-eV)[f(E)-f(E-eV)]d\theta dE \tag{5.4}$$

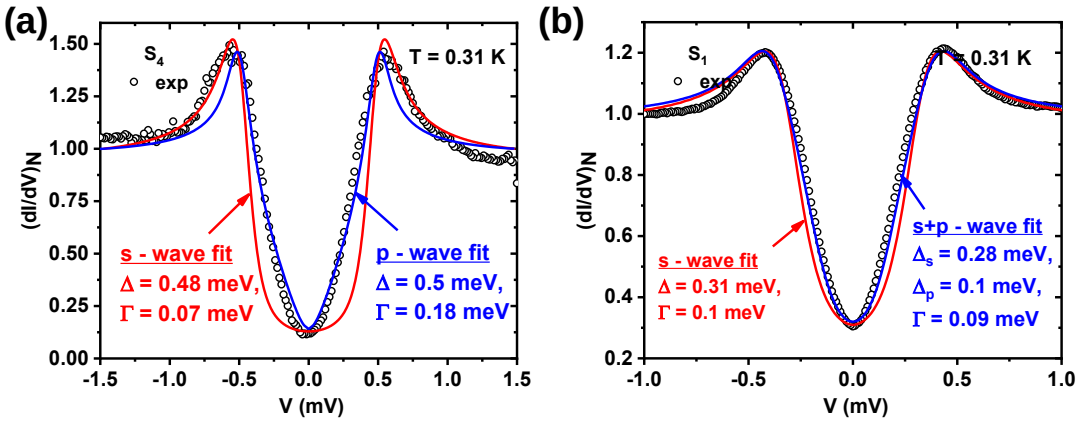

Figure 5.7.1: **(a)** Comparison of best single gap 's-wave' fit (red line) and 'p-wave' fit (blue line) for the spectrum (of second type) presented before in Fig. 5.3.1(c). **(b)** Comparison of best pure 's-wave' fit (red line) and mixed '$s+p$-wave' fit (blue line) for the spectrum (of first type) presented before in Fig. 5.3.1(a).

In Fig. 5.7.1(a), the same experimental spectrum which was shown earlier in Fig. 5.3.1(c) is represented. The theoretical plots considering isotropic 's-wave' Δ (red line) and anisotropic 'p-wave' Δ (blue line) are shown for comparison. It is clear that the spectrum, especially the 'V'-shaped part of that between the coherence peaks, is better described by the 'p-wave' symmetry. It is also interesting to note that the extracted value of Δ (0.47 meV) for such fit does not differ much with the same from the best 's-wave' fit (0.48 meV).

Such 'V'-shaped STS spectra are often seen for superconductors with possible unconventional symmetries and are well described by the Tanaka-Kashiwaya model [36, 40] we used here. For example, considering various possible symmetries under the framework of an 'anisotropic s-wave' model in MgB_2, Seneor *et al.* [41] explained spectroscopic signatures *e.g.*, very high coherence peaks, 'V'-shaped valley and also zero-biased coherence peak (ZBCP). In anisotropic $Bi_2Sr_2CaCu_2O_8$, Ichimura *et al.* [42] reported two types of spectra, one with a 'V'-shape and another with a flat bottom. The authors explained those with a model of mixed '$s + d$-wave' symmetry where the former isotropic component is the dominant one. Millo *et al.* [37] reported both 'V'-shaped spectra and spectra with ZBCP in $SmFeAsO_{0.85}$ and adduced such shapes with the 'd-wave' order parameter. To note, it was also reported there that some of the tunneling spectra could also be fitted well within a pure 's-wave' model but with significantly smaller Δ and relatively higher Γ [37] – a situation exactly similar to our first type of spectra (Fig. 5.3.1(a) and (b)). From our analysis, an order parameter with either 'p-wave' or 'd-wave' symmetry can reproduce a 'V'-shaped spectra we described as of second type. However, as reported by Cameron *et al.* [32], the spontaneous magnetic field present in Ru_7B_3 breaks the time-reversal symmetry in the order parameter and supports the 'p-wave' gap as a more favouable possibility.

The success of the p-wave model for the second type of spectra encourages us to reconsider the analysis of the first type of spectra also. As we have seen earlier in Fig. 5.3.1(a) and (b), although the conventional s-wave model can fairly explain the experimental data, a close inspection would reveal a slight mismatch between the experimental and theoretical spectra. We also have observed from our systematic temperature dependence study (Fig. 5.4.1(a)), that discrepancy vanishes at higher temperature. If Ru_7B_3 has a mixed angular momentum symmetry in its order parameter, then we would expect the unconventional component to be present in the first type of spectra too. To understand this aspect in detail, we used a generalized '$s + p$-wave' model to analyse the spectra. In this model, the effective gap is given by $\Delta_{s+p} = \Delta_s + \Delta_p Cos\theta$. In Fig. 5.7.1(b), the same experimental spectrum which was shown earlier in Fig. 5.3.1(a), is represented. The numerically generated best '$s + p$-wave' fit (blue line) and the previous pure

's-wave' fit (red line), both are shown for comparison. It is clear that the mixed angular momentum symmetry provides a better description of the data.

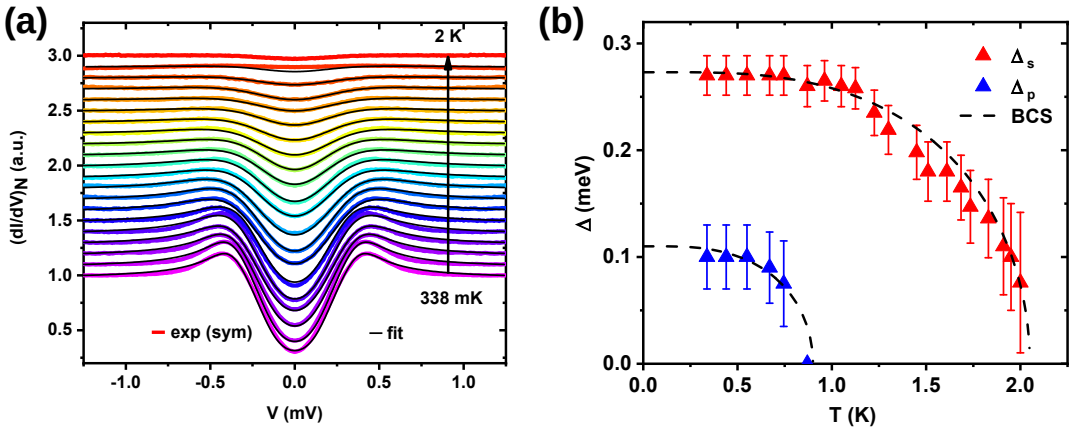

Figure 5.7.2: **(a)** Temperature (T) dependence of the same spectra in Fig. 5.4.1(a) (colour lines) but now with s+p-wave theoretical fits (black lines). **(b)** Evolution of extracted Δ_s and Δ_p with T. Ideal BCS trends of Δ are also shown for comparison.

Equipped with this $s + p$-wave model, now we will revisit the temperature dependence of the spectra previously shown in Fig. 5.4.1(a). The experimental spectra and the corresponding fittings with the $s + p$-wave model are presented in Fig. 5.7.2(a). Unlike before, now the theoretical and experimental spectra match perfectly starting from the lowest temperature. Temperature evolutions for the amplitudes of the two components Δ_s and Δ_p extracted from the fittings are presented in Fig. 5.7.2(b). The conventional Δ_s follows a smooth BCS like dependence up to 2 K. Unlike before, now Δ_s does saturates at low temperature as expected from BCS theory [2] because the excess amount is now compensated by the other smaller component, Δ_p, which sharply drops at 0.9 K. This also explains why Fang *et al.* did not find any signature of unconventionality in their lower critical field (H_{c1}) studies [26] down to 1.2 K, which is well above the temperature window where we could notice the deviation from s-wave behaviour in our data.

5.8 Summary

We used scanning tunneling spectroscopy to record numerous spectra on single-crystal Ru_7B_3 and divided them into two groups. The first type of spectra are shallow and narrow in shape. Except at very low temperatures, where they diverge from such a pure 's-wave' model, they exhibit an overall good agreement with a single gap with 's-wave' symmetry. These spectra have a smaller superconducting gap and a larger broadening parameter. The second type of spectra are broader in shape and show sharper coherence peaks. They differ greatly from the predictions of the 's-wave' model, but a theoretical model with 'p-wave' symmetry produces better agreement. In comparison to the first type, the superconducting gap is larger, and the broadening parameter is smaller for such spectra. The temperature dependences of the spectra in both types, in general, show that the order parameter has a mixed '$s + p$-wave' symmetry, with the two components having independent temperature dependences.

Acknowledgement

The ULT STM/S data were acquired by Aastha Vasdev and Soumyadip Halder with my active participation. Ranjani Ramachandran contributed in data fitting. Kapil Motla, Anshu Kataria, Arushi, Rajeswari Roy Chowdhur and Ravi Prakash Singh from IISER Bhopal synthesized and characterized the single crystal. We thank Dr. Tanmoy Das for his useful comments.

Addendum

The work presented in this chapter was published [1] in *Scientific Reports* in 2021. In 2022, Cameron *et al.* [43] further verified the singlet-triplet mixing in the superconducting order parameter of Ru_7B_3 based on the temperature dependence of vortex lattice form factor at 0.2 T magnetic field. This observation again confirms the mixed symmetry we already have reported for the first time in this material based on our direct measurement of the gap through scanning tunneling spectroscopy.

Bibliography

[1] Soumya Datta, Aastha Vasdev, Ranjani Ramachandran, Soumyadip Halder, Kapil Motla, Anshu Kataria, Rajeswari Roy Chowdhury, Ravi Prakash Singh, Goutam Sheet, et al. Spectroscopic evidence of mixed angular momentum symmetry in non-centrosymmetric Ru_7B_3. *Scientific Reports*, 11(1):1–7, 2021.

[2] John Bardeen, Leon N Cooper, and John Robert Schrieffer. Theory of superconductivity. *Physical Review*, 108(5):1175, 1957.

[3] HR Ott, H Rudigier, TM Rice, K Ueda, Z Fisk, and JL Smith. p-wave superconductivity in UBe_{13}. In *Ten Years of Superconductivity: 1980–1990*, pages 156–159. Springer, 1984.

[4] K Ueda and TM Rice. p-wave superconductivity in cubic metals. *Physical Review B*, 31(11):7114, 1985.

[5] Yoshiteru Maeno, Shunichiro Kittaka, Takuji Nomura, Shingo Yonezawa, and Kenji Ishida. Evaluation of spin-triplet superconductivity in Sr_2RuO_4. *Journal of the Physical Society of Japan*, 81(1):011009, 2011.

[6] DA Wollman, DJ Van Harlingen, WC Lee, DM Ginsberg, and AJ Leggett. Experimental determination of the superconducting pairing state in YBCO from the phase coherence of YBCO-Pb dc squids. *Physical Review Letters*, 71(13):2134, 1993.

[7] CC Tsuei, John R Kirtley, CC Chi, Lock See Yu-Jahnes, A Gupta, T Shaw, JZ Sun, and MB Ketchen. Pairing symmetry and flux quantization in a tricrystal superconducting ring of $YBa_2Cu_3O_{7-\delta}$. *Physical Review Letters*, 73(4):593, 1994.

[8] CC Tsuei and JR Kirtley. Pairing symmetry in cuprate superconductors. *Reviews of Modern Physics*, 72(4):969, 2000.

[9] Frank Steglich, J Aarts, CD Bredl, W Lieke, D Meschede, W Franz, and H Schäfer. Superconductivity in the presence of strong pauli paramagnetism: $CeCu_2Si_2$. *Physical Review Letters*, 43(25):1892, 1979.

[10] TA Tokuyasu, DW Hess, and JA Sauls. Vortex states in an unconventional superconductor and the mixed phases of UPt_3. *Physical Review B*, 41(13):8891, 1990.

[11] KA Kouznetsov, AG Sun, B Chen, AS Katz, SR Bahcall, John Clarke, RC Dynes, DA Gajewski, SH Han, MB Maple, et al. c-axis josephson tunneling between $YBa_2Cu_3O_{7-\delta}$ and Pb: direct evidence for mixed order parameter symmetry in a high-T_C superconductor. *Physical Review Letters*, 79(16):3050, 1997.

[12] James F Annett. Symmetry of the order parameter for high-temperature superconductivity. *Advances in Physics*, 39(2):83–126, 1990.

[13] PA Frigeri, DF Agterberg, A Koga, and M Sigrist. Superconductivity without inversion symmetry: MnSi versus $CePt_3Si$. *Physical Review Letters*, 92(9):097001, 2004.

[14] Ernst Bauer, Gerfried Hilscher, Herwig Michor, Ch Paul, Ernst-Wilhelm Scheidt, A Gribanov, Yu Seropegin, H Noël, M Sigrist, and Peter Rogl. Heavy fermion superconductivity and magnetic order in noncentrosymmetric $CePt_3Si$. *Physical Review Letters*, 92(2):027003, 2004.

[15] RP Kaur, DF Agterberg, and Manfred Sigrist. Helical vortex phase in the noncentrosymmetric $CePt_3Si$. *Physical Review Letters*, 94(13):137002, 2005.

[16] Masatoshi Sato and Satoshi Fujimoto. Topological phases of noncentrosymmetric superconductors: Edge states, Majorana fermions, and non-Abelian statistics. *Physical Review B*, 79(9):094504, 2009.

[17] Manfred Sigrist, DF Agterberg, PA Frigeri, N Hayashi, RP Kaur, A Koga, I Milat, K Wakabayashi, and Y Yanase. Superconductivity in non-centrosymmetric materials. *Journal of magnetism and magnetic materials*, 310(2):536–540, 2007.

[18] Adrian D Hillier, Jorge Quintanilla, and Robert Cywinski. Evidence for time-reversal symmetry breaking in the noncentrosymmetric superconductor $LaNiC_2$. *Physical Review Letters*, 102(11):117007, 2009.

[19] Ernst Bauer and Manfred Sigrist. *Non-centrosymmetric superconductors: introduction and overview*, volume 847. Springer Science & Business Media, 2012.

[20] KV Samokhin, ES Zijlstra, and SK Bose. $CePt_3Si$: An unconventional superconductor without inversion center. *Physical Review B*, 69(9):094514, 2004.

[21] Bertil Aronsson. The crystal structure of Ru_7B_3. *Acta Chem. Scand.*, 13(1), 1959.

[22] BT Matthias, VB Compton, and E Corenzwit. Some new superconducting compounds. *Journal of Physics and Chemistry of Solids*, 19(1-2):130–133, 1961.

[23] JM Vandenberg, BT Matthias, E Corenzwit, and H Barz. Superconductivity of some binary and ternary transition-metal borides. *Materials Research Bulletin*, 10(9):889–894, 1975.

[24] JP Morniroli, H Ayatti, KM Knowles, WM Stobbs, and M Gantois. Transmission electron microscopy of Ru_7B_3 borides. *Journal of the Less Common Metals*, 155(2):215–227, 1989.

[25] Koichi Momma and Fujio Izumi. VESTA 3 for three-dimensional visualization of crystal, volumetric and morphology data. *Journal of Applied Crystallography*, 44(6):1272–1276, 2011.

[26] Lei Fang, Huan Yang, Xiyu Zhu, Gang Mu, Zhao-Sheng Wang, Lei Shan, Cong Ren, and Hai-Hu Wen. Physical properties of the noncentrosymmetric superconductor Ru_7B_3. *Physical Review B*, 79(14):144509, 2009.

[27] Soumya Datta, Aastha Vasdev, Soumyadip Halder, Jaskaran Singh, Yogesh Singh, and Goutam Sheet. Spectroscopic signature of two superconducting gaps and their unusual field dependence in RuB_2. *Journal of Physics: Condensed Matter*, 32(31):315701, 2020.

[28] Naoki Kase and Jun Akimitsu. Superconducting state of the binary boride Ru_7B_3 with the noncentrosymmetric crystal structure. *Journal of the Physical Society of Japan*, 78(4):044710–044710, 2009.

[29] Ravi P Singh, Natalia A Parzyk, Martin R Lees, D McK Paul, and Geetha Balakrishnan. Crystal growth and properties of the non-centrosymmetric superconductor, Ru_7B_3. *Journal of Crystal Growth*, 395:22–25, 2014.

[30] H Takeya, M ElMassalami, S Kasahara, and K Hirata. Specific-heat studies of the spin-orbit interaction in noncentrosymmetric $Li_2(Pd_{1-x}Pt_x)_3B$ (x= 0, 0.5, 1) superconductors. *Physical Review B*, 76(10):104506, 2007.

[31] T Takeuchi, M Tsujino, T Yasuda, S Hashimoto, R Settai, and Y Ōnuki. Specific heat study on the heavy fermion superconductor $CePt_3Si$. *Journal of Magnetism and Magnetic Materials*, 310(2):557–559, 2007.

[32] AS Cameron, YS Yerin, YV Tymoshenko, PY Portnichenko, AS Sukhanov, M Ciomaga Hatnean, D Mc K Paul, G Balakrishnan, R Cubitt, A Heinemann, et al. Rotation of the magnetic vortex lattice in Ru_7B_3 driven by the effects of broken time-reversal and inversion symmetry. *Physical Review B*, 100(2):024518, 2019.

[33] RC Dynes, V Narayanamurti, and J Pm Garno. Direct measurement of quasiparticle-lifetime broadening in a strong-coupled superconductor. *Physical Review Letters*, 41(21):1509, 1978.

[34] Masashi Yamashiro, Yukio Tanaka, Nobukatsu Yoshida, and Satoshi Kashiwaya. Tunneling conductance and spatial dependences of pair potentials in normal metal-triplet superconductor junctions. *Journal of the Physical Society of Japan*, 68(6):2019–2025, 1999.

[35] Frank Laube, Gernot Goll, Matthias Eschrig, Mikael Fogelström, and Ralph Werner. Excess current in superconducting Sr_2RuO_4. *Physical Review B*, 69(1):014516, 2004.

[36] Yukio Tanaka and Satoshi Kashiwaya. Theory of tunneling spectroscopy of d-wave superconductors. *Physical Review Letters*, 74(17):3451, 1995.

[37] Oded Millo, Itay Asulin, Ofer Yuli, Israel Felner, Zhi-An Ren, Xiao-Li Shen, Guang-Can Che, and Zhong-Xian Zhao. Scanning tunneling spectroscopy of $SmFeAsO_{0\cdot 85}$: Possible evidence for d-wave order-parameter symmetry. *Physical Review B*, 78(9):092505, 2008.

[38] GE Volovik. Superconductivity with lines of gap nodes: density of states in the vortex. *Soviet Journal of Experimental and Theoretical Physics Letters*, 58:469, 1993.

[39] Natalia A Parzyk. *Muon and neutron studies of unconventional superconductors*. PhD thesis, University of Warwick, 2014.

[40] Satoshi Kashiwaya, Yukio Tanaka, Masao Koyanagi, and Koji Kajimura. Theory for tunneling spectroscopy of anisotropic superconductors. *Physical Review B*, 53(5):2667, 1996.

[41] P Seneor, C-T Chen, N-C Yeh, RP Vasquez, LD Bell, CU Jung, Min-Seok Park, Heon-Jung Kim, WN Kang, and Sung-Ik Lee. Spectroscopic evidence for anisotropic s-wave pairing symmetry in MgB_2. *Physical Review B*, 65(1):012505, 2001.

[42] Koichi Ichimura and Kazushige Nomura. Stm study of anisotropic superconducting gap of $Bi_2Sr_2CaCu_2O_8$. *Journal of the Physical Society of Japan*, 62(10):3661–3679, 1993.

[43] AS Cameron, YS Yerin, YV Tymoshenko, PY Portnichenko, AS Sukhanov, M Ciomaga Hatnean, D McK Paul, G Balakrishnan, R Cubitt, A Heinemann, et al. Singlet-triplet mixing in the order parameter of the noncentrosymmetric superconductor Ru_7B_3. *Physical Review B*, 105(9):094519, 2022.

Appendix

5.A Why was the Unconventional Pairing Undetected in Previous Reports?

In Section 5.6 of the main chapter, I pointed out numerous clues supporting unconventional pairing in Ru_7B_3 from previous reports [1–3], though all the articles have individually concluded about the conventional BCS superconductivity in this material. Here, I will explain one possible reason why that happened.

Fang *et al.* reported [2] that the lower critical field (H_{c1}) vs. temperature (T) data was consistent with s-wave pairing model considering a single isotropic gap of 0.5 meV. To note, this value we found to be closer to the second type of spectra we have probed (Fig. 5.3.1(c) in the main chapter, for example). However, the authors also specifically pointed out their inability to present data below 1.2 K and safely concluded that from the data they could present, non-centrosymmetric superconductor Ru_7B_3 was found to be dominated by s-wave pairing. Interestingly, the same data reported by the other group [1] on single crystal started from even further higher temperature ~ 1.8 K and estimated the H_{c1} almost half! From our detailed sub-kelvin, energy-resolved spectroscopic study, we found out how important a role temperature plays here and possibly why for most of the previous studies anisotropic/nodal gaps remained illusive. From Fig. 5.4.1(a) in the main chapter, we see that the significant departure of the experimental data with the conventional s-wave model actually happens at sub-kelvin temperature. From Fig. 5.7.2(b) in the main chapter, we can further clearly see that the unconventional p-wave component vanished before reaching ~ 1 K temperature. Therefore, it was

absolutely normal for the two groups [1, 2] to see only conventional superconductivity in Ru_7B_3 as they started their measurements from a higher temperature.

5.B Discussion about Coupling Strength

Another interesting fact we observed is the following. It may seem that the superconducting gap Δ_0 (= 0.3 meV) and the transition temperature T_c (= 2 K) we found are both underestimated compared to the reported values. Nevertheless, the ratio Δ_0/k_BT_c came out to be 3.48, which is perfectly in agreement with the weak-coupling BCS limit of 3.52. On the other hand, within our best knowledge, only Kase and Akimitsu [1] so far reported this ratio for single-crystal Ru_7B_3, based on their specific heat measurements. However, their calculated value 3.3 can be under serious doubt, as that does not even match with their own reported $T_c = 2.8$ K and $\Delta_0 = 0.38$ meV from the same specific heat measurements which they used for their calculation. Fang *et al.* [2] reported the ratio 3.6 from specific heat measurements also but experimenting on a polycrystal instead.

5.C Possibility of Proximity Induced Superconductivity

We probed two types of spectra on the surface of Ru_7B_3 (Fig. 5.3.1). In a different context, a similar variety of transport spectra is possible if some superconducting nanoislands are deposited and separated spatially from each other on an otherwise non-superconducting metal or insulator [4, 5]. Proximity induced superconductivity (PIS) is reported on such non-superconducting substance in the neighbourhood of those superconducting islands, which eventually gets vanished while moving away from the islands. Nevertheless, in our case, the whole surface under the tip is of a pure superconducting Ru_7B_3 single-crystal, unlike such geometry, and we did not find an entirely gapless flat spectrum anywhere on the surface. Moreover, as reported by Cherkez *et al.* [5], spectra probed on the superconducting islands and away from the islands, both could be well fitted with the BCS model with just

different sets of parameter values. However, in our case, a pure BCS model fails to explain the spectra, and an anisotropic component, whether relatively small (for the first type of spectra) or large (for the second type of spectra) is essential. In that way, we can safely exclude the possibility of any proximity effect in our measurements. The T_c^j and the $H_{c(l)}$ that we measure for all our spectra match well irrespective of whether they fall under the first or the second type. Therefore, it can be concluded that all the spectra falling under two distinct types differ from each other based on which component of the order parameter contributes predominantly for a particular crystallite that the measurement is performed on.

Bibliography

[1] Naoki Kase and Jun Akimitsu. Superconducting state of the binary boride Ru_7B_3 with the noncentrosymmetric crystal structure. *Journal of the Physical Society of Japan*, 78(4):044710–044710, 2009.

[2] Lei Fang, Huan Yang, Xiyu Zhu, Gang Mu, Zhao-Sheng Wang, Lei Shan, Cong Ren, and Hai-Hu Wen. Physical properties of the noncentrosymmetric superconductor Ru_7B_3. *Physical Review B*, 79(14):144509, 2009.

[3] Ravi P Singh, Natalia A Parzyk, Martin R Lees, D McK Paul, and Geetha Balakrishnan. Crystal growth and properties of the non-centrosymmetric superconductor, Ru_7B_3. *Journal of Crystal Growth*, 395:22–25, 2014.

[4] L Serrier-Garcia, JC Cuevas, Ten Cren, Christophe Brun, V Cherkez, François Debontridder, D Fokin, FS Bergeret, and D Roditchev. Scanning tunneling spectroscopy study of the proximity effect in a disordered two-dimensional metal. *Physical Review Letters*, 110(15):157003, 2013.

[5] V Cherkez, JC Cuevas, C Brun, T Cren, G Ménard, François Debontridder, VS Stolyarov, and D Roditchev. Proximity effect between two superconductors spatially resolved by scanning tunneling spectroscopy. *Physical Review X*, 4(1):011033, 2014.

Chapter 6

Anisotropic Superconductivity in ZrB_{12}

In this chapter, the superconducting properties of ZrB_{12} are investigated. Based on directional point-contact Andreev reflection spectroscopy and field-angle dependent ac magnetic susceptibility measurements, we show that ZrB_{12} is an anisotropic superconductor, and it exhibits field-direction dependent type-I and type-II behavior. The work presented in this chapter is already published in Ref. [1].

6.1 Introduction

6.1.1 Anisotropy and Intertype Domain

According to the phenomenological Ginzburg-Landau (G-L) theory [2, 3], conventional superconductors are classified into two categories based on their magnetic properties. Type-I superconductors are perfectly diamagnetic, whereas type-II superconductors allow an external magnetic field to penetrate as single-quantum vortices. If the density of the vortices is high enough, they create an Abrikosov lattice [4, 5] in the latter situation. The G-L parameter κ, which is the ratio between magnetic penetration depth λ and superconducting coherence length ξ of a superconductor, is used to define and identify these two types [6]. If $\kappa < 1/\sqrt{2}$, a superconductor behaves like a type-I, and if $\kappa > 1/\sqrt{2}$, it behaves like a type-II. However, if the superconductor has $\kappa \sim 1/\sqrt{2}$ [7–12], this classification fails. Also,

the G-L formalism is strictly valid near the superconducting critical temperature ($T \sim T_c$). As a result, only at or near its T_c a superconductor can be classified as type-I or type-II. This critical point ($1/\sqrt{2}$, T_c) is referred to as the Bogomolnyi point (B-point) [13, 14] in the hypothetical phase space (κ, T).

The vortex-vortex interaction is attractive in type-I superconductors but repulsive in type-II superconductors [14]. The interaction between the vortices, however, totally vanishes at the B-point, and an infinite degeneracy of arbitrary flux configurations arises [13, 14]. When $T < T_c$, the B-point spreads over a finite interval of κ values [15–18], and the traditional definition of type-I and type-II superconductivity breaks down [10–12]. Intertype (IT) superconductors are the superconductors that fall within this category. The interaction between the vortices becomes non-monotonic at this point. As a result, both attractive long-range interactions and repulsive short-range interactions become possible. As a temperature-dependent range of κ (over which the B-point spreads) is expected in such systems, so a temperature-dependent transition between the usual type-I to a type-II superconducting phase can also be expected. Aside from that, because the B-point is infinitely degenerate, the superconductor becomes susceptible to other internal and external factors such as system geometry, impurities, applied current, and external magnetic field. In the first chapter (introduction) of this thesis, we already have discussed about such temperature and magnetic field sensitivity of an IT superconductor. According to some recent experimental findings [19–22], ZrB_{12} is thought to be one example of such IT superconductors.

It is worth noting that all of the physics discussed above applies to isotropic superconductors. Saraiva *et al.* [23] recently theoretically demonstrated that the same concept of intertype superconductors can also be applied to anisotropic superconductors. An suitable scaling transformation [24, 25] just have to be added into the formalism in order for this formalism to function. The direction of the applied magnetic field influences this transition. As a result, the type of superconductivity for magnetic fields applied in different directions may differ. In this chapter, based on a variety of experimental studies and analysis, we will see that ZrB_{12} is such an anisotropic superconductor, where the superconducting type varies on the

direction of the magnetic field with respect to the crystal axes.

6.1.2 Why is ZrB_{12} so Widely Studied?

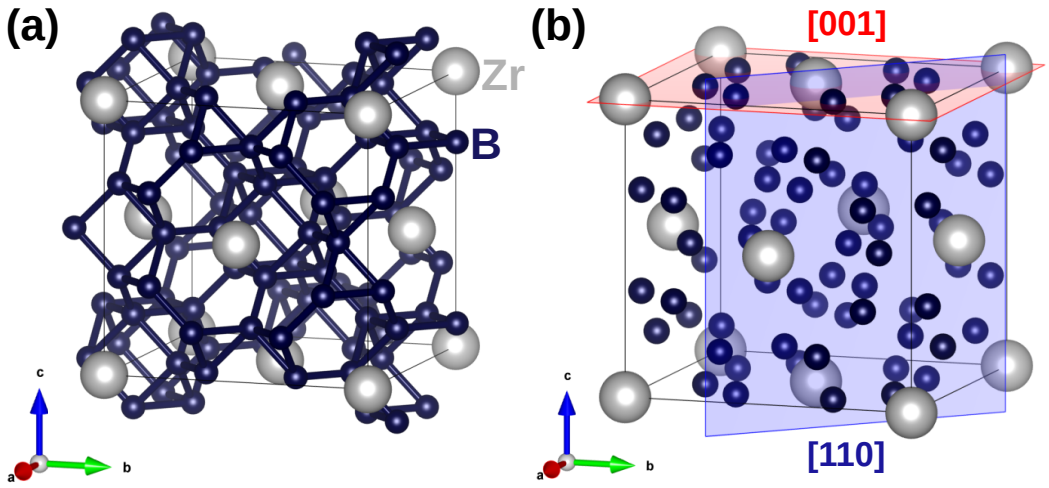

Figure 6.1.1: **(a)** The crystal structure of ZrB_{12} (a single unit cell). **(b)** One [001] plane (red surface) and another [110] plane (blue surface) latter to be associated with z and x axes PCS, respectively.

The crystal structure of ZrB_{12} is represented in Fig. 6.1.1 [26, 27]. It has an fcc structure of space group $Fm\bar{3}m$ [26, 28, 29], and it has $T_c \sim 5.85$ K [19, 30–36]. The superconductivity in this material is due to the optical phonon modes, which are connected with the internal motion of the Zr atoms inside the boron cage [37]. According to the band structure calculation, the Fermi level of ZrB_{12} is placed at an extended flat plateau in its electronic density of states (DOS), which makes the superconducting phase exceptionally stable against any perturbations like chemical impurities or crystal defects [38]. As we will see later, this particular property of ZrB_{12} would be especially useful for our point contact Andreev reflection investigation. The Fermi surface of ZrB_{12} is made up of an open sheet with hole characters and a quasi-spherical sheet with electron characters [38]. Optical [39] and de Haas-van Alphen experiments [40] were used to confirm these structures. To note, compared to the highly anisotropic Fermi surface of MgB_2 [41, 42], the Fermi surface of ZrB_{12} is less anisotropic. This validates the prototype ellipsoidal

Fermi surface model for anisotropic superconductor used by Saraiva *et al* [23]. For MgB_2, in contrast, such a model would not be much useful as some Fermi surface sheets are almost cylindrical in shape.

Despite extensive theoretical and experimental research on ZrB_{12}, there are considerable discrepancies in the literature about this system's superconducting properties. The unexpected behaviors of ZrB_{12} can be roughly classified under three points, when compared to an ideal BCS superconductor. We will attempt to shed light on each of these in this chapter. The electron-phonon coupling of superconducting ZrB_{12} is the property that has received the highest attention. ZrB_{12} was assumed to be in the weak coupling domain based on multiple independent bulk sensitive experimental studies such as temperature-dependent resistivity, critical field, specific-heat, thermal-expansion experiments, etc [32, 33, 43]. However, a number of investigations, including point contact spectroscopy, tunnelling spectroscopy, and de Haas-van Alphen effect have shown the opposite and pointed to a strong coupling superconductivity [31, 32, 39, 40, 43, 44]. It also has been proposed, to explain the disparities in bulk and surface superconducting qualities, that this material has enhanced surface characteristics [34, 43].

The description of the superconducting order parameter is the second outstanding issue about ZrB_{12}. An evidence of *d*-wave pairing symmetry was reported in ZrB_{12} based on the temperature dependence of the penetration depth study [35]. A few reports also discussed the possibility of two-gap superconductivity in this material [36, 45, 46]. But, the experiments on specific heat, resistivity, magnetic susceptibility, and thermal expansion supported the concept of single gap BCS superconductivity in ZrB_{12} [19, 33]. Furthermore, all previous energy-resolved spectroscopic studies on ZrB12 have only supported single gap *s*-wave symmetry [32, 43].

The magnetic behavior is the third unusual property of superconducting ZrB_{12}, and it is also the most important in our current analysis. Lortz *et al.* [33]. and Wang *et al.* [19] revealed that ZrB_{12} demonstrates a shift from type-I superconductivity near T_c to type-II behavior below $\sim$ 4.6 K based on several bulk-sensitive

measurements. This was the first indication that ZrB_{12} might be classed as a type-II/I superconductor. The argument was also supported by the reported G-L parameter (κ) ~ 0.65 [19], which is clearly near to the border value $1/\sqrt{2}$. A vortex pattern transition was seen in ZrB_{12} throughout the type-II and type-II/I phases, according to a scanning Hall probe microscopy study [20]. According to the paramagnetic Meissner effect study [21], vortex clusters mediate the flux expulsion and penetration at low temperatures in this material. Interestingly, muon spin rotation studies on ZrB_{12} recently revealed that the type-I and type-II behaviors coexist simultaneously within a finite temperature range [22]. This new discovery contradicts the earlier theory of a temperature-dependent transition from type-I to type-II superconductivity. The authors argued about the controversial type-1.5 regime [47], where material's coherence length might be larger or smaller than the magnetic penetration depth. In addition, a notable anisotropy in the upper critical field has recently been reported [46] in ZrB_{12}, which seemingly depend on the magnetic field vector's orientation. The authors associated their findings to 'two-gap superconductivity'. However, such evidence of anisotropy urges us to put the IT model proposed by Saraiva *et al.* [23] in ZrB_{12} to the test. Furthermore, as previously stated, the real order parameter symmetry of the superconducting gap for ZrB_{12} is still a topic of debate. In that context, an energy-resolved spectroscopic measurement like PCARS will be relevant and useful.

6.2 Experimental Methods

Both the surface-sensitive point contact Andreev reflection spectroscopy (PCARS) [48, 49] and bulk-sensitive ac susceptibility (χ) measurements were performed using two different home-built probes inside the same liquid helium cryostat. For temperature-dependent experiments, a variable temperature insert (VTI) was used, the base temperature of which varies from 1.6 K to 2 K depending on the different probes inside, and the helium level in the cryostat. For magnetic field dependent studies, a superconducting vector magnet is used, which can produce a maximum 6 T along the vertical direction parallel to the axis of the cryostat and 1 T each in two mutually perpendicular directions in the horizontal plane. The χ measurements were performed by sandwiching the sample between two coaxial

copper coils connected to a lock-in amplifier. One coil was fed with the ac signal at 17.33 kHz frequency, and the other one was used as the pick-up coil. Magnetization and susceptibility (both ac and dc) measurements on ZrB_{12} were reported multiple times in the past [19–21, 32–34, 43, 50, 51] to characterize the material. Here, our objective of χ measurements was to verify the crystal quality and identify the transitions. As the exact value of χ is not of interest, χ is not volume corrected, and an arbitrary unit is used throughout. For the same reason, the imaginary and real components of χ are also not separated. For temperature and magnetic field dependence, the overall magnitude of χ is presented after a subtraction of the normal state saturation value. The point-contact probe works based on a differential screw mechanism and uses the standard needle-anvil method for contact formation. The surface of the crystal was properly cleaned before the spectroscopy experiments and the point contacts were formed *in situ* at low temperatures with a Silver (Ag) tip. To have proper statistics, we probed different crystallographic facets of a single crystal of ZrB_{12}, and recorded spectra on different points on the same facet.

ZrB_{12} has a cubic crystal structure [26, 28, 29] (see Fig. 6.1.1(a) in the previous section). Hence, a, b, and c axes of the crystal are equivalent and indistinguishable. To eliminate any confusion between the axes of the crystal and the axes of the vector magnet, the following terminology is used throughout this chapter. For PCARS experiments, we have used two unique facets of the single crystal. The semi-arc-shaped sample we used for our studies was cut from a rod-shaped single crystal grown by the floating-zone technique. The approximate dimension of the sample is 6 mm $\times$ 2.5 mm $\times$ 1.5 mm. One facet of that sample was a plane perpendicular to the crystal growth axis (say c-axis or [001] by convention) and of area $\sim$ 6 $\times$ 2.5 sq. mm. The spectra probed on that surface are described as 'z-axis PCS'. Another facet was a plane perpendicular to the previous one but with a $\sim 45^\circ$ slant angle with the other two primary axes (say [100] and [010]) of the crystal. This apparently [110] plane has an area of $\sim$ 6 $\times$ 1.5 sq. mm and the spectra probed on this surface are described as 'x-axis PCS'. One [001] and one [110] plane are shown in Fig. 6.1.1(b) in the crystal structure of ZrB_{12}. For the magnetic field-dependent study of the spectra, the field was always applied

perpendicular to the surface being probed. To describe the direction of the applied magnetic field in the susceptibility measurements, we used the similar convention where the z-axis is the crystal growth (c) axis and x and y axes are two mutually perpendicular axes in the ab-plane of the crystal.

6.3 Limitations of Previous PCARS Reports

According to the best of our knowledge, there are so far two reports [32, 44] of PCARS on ZrB_{12}. Daghero *et al.* [32] have used soft point contact and could reach a minimum $T = 4.2$ K which was merely 30 % below the $T_c = 5.85$ K for ZrB_{12}. Like us, the authors also have reported a pure s-wave gap symmetry from the BTK model fit [52, 53]. However, the spectra they have reported also had critical current dominated artefacts [54] at higher bias. We also have recorded such spectra typical of the intermediate regime of transport, which slightly overestimates the superconducting gap Δ. Nevertheless, we only have used spectra in pure spectroscopic (ballistic or diffusive) regime for analysis and further temperature and magnetic field dependent studies. The second report was by Girovský *et al.* [44], where the authors were primarily interested in the second derivative d^2I/dV^2 vs V to reveal the electron–phonon coupling mechanism. The spectra we probed, especially the one in Fig. 6.4.1(c), and the corresponding fitting parameters match with the same reported by this second group. Daghero *et al.* [32] only have presented the temperature dependence of the spectra but not the magnetic field dependence. Girovský *et al.* [44] have shown neither temperature nor magnetic field dependence of the spectra. None of these two groups has inspected any anisotropy in superconducting ZrB_{12}. For that purpose, we would start our fresh investigation with directional point contact Andreev reflection spectroscopy (PCARS) in the next section.

6.4 Directional PCARS

In the first chapter (introduction) of this thesis, a brief overview of directional PCARS was provided. This method was applied on single crystal ZrB_{12} to study

two mutually perpendicular facets as already been described. As we already know, Andreev reflection [48] is a quantum process that dominates the electronic transport through a ballistic point-contact between a normal metal and a superconductor. The process involves the reflection of a spin-up (down) electron as a spin-down (up) hole from the interface and the *vice versa*. This leads to a typical nonlinearity in the $I - V$ spectrum, which can be directly probed in a dI/dV vs V spectrum recorded across the point contact [49]. We employed a lock-in based modulation technique to probe such spectra and the modified Blonder-Tinkham-Klapwijk (BTK) model [53] to analyse the same. It may be noted that all the PCAR data presented here clearly show the hall-mark double-peak (symmetric about $V = 0$) signature of Andreev reflection [48] and no other features like anomalous conductance dips [54]. This confirms that our measurements are performed in the spectroscopic (ballistic or diffusive) regime of transport. Compared to other superconductors we have studied earlier, it was surprisingly easy to find a contact in such a spectroscopic regime for ZrB_{12}. The possible reasons can be the large coherence length(s) [22, 46], an unusually high T_c compared to other dodecaborides, and the high purity of the single crystal we have used of ZrB_{12}. As mentioned earlier, the extended flat DOS neighbourhood of the Fermi level [38] for this material can be another possible reason behind such stability. The traditional BTK model [52] assumes a δ-function potential barrier whose strength is characterized by a dimensionless parameter Z. Apart from Z, the inelastic broadening parameter Γ is used to take care of the finite quasi-particle lifetime in modified BTK theory [53]. The parameters Z, Γ along with the superconducting energy gap Δ are used to fit a spectrum at a particular temperature T.

6.4.1 Anisotropy in Gap

Fig. 6.4.1 represents PCAR spectra probed at $T \sim 2$ K on two distinct open facets of ZrB_{12}. Three typical spectra probed under the 'x-axis PCS' configuration are shown with 'red circles' in Fig. 6.4.1(a), (b), and (c). The corresponding theoretical fits to the spectra using the modified BTK theory [53] are represented with 'black lines'. The extracted fitting parameters Δ, Γ and Z are also mentioned for each spectrum. Similarly, in Fig. 6.4.1(d), (e), and (f), three typical spectra

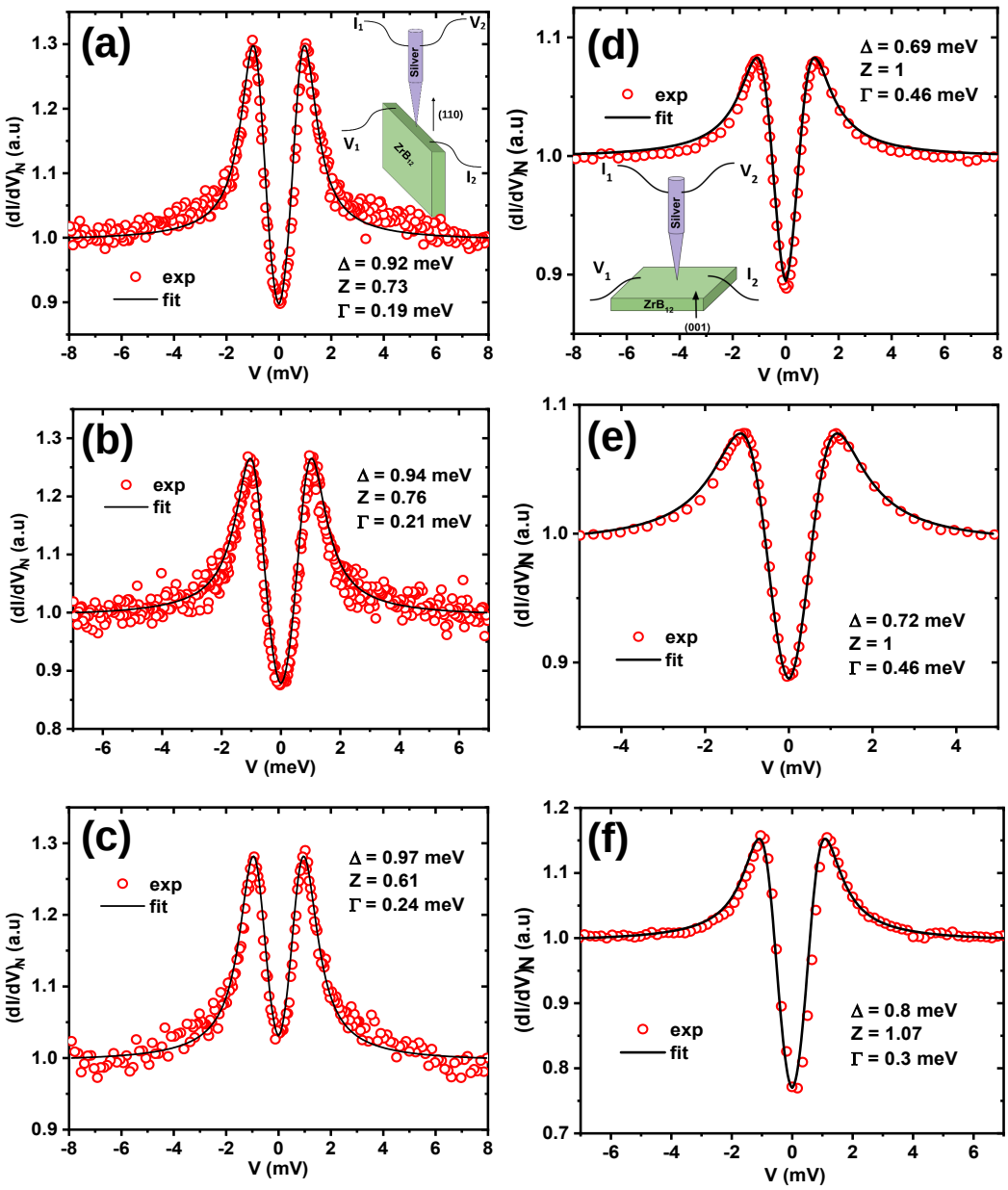

Figure 6.4.1: Representative conductance spectra (red circles) of ZrB_{12} for point contacts formed along x-axis (**(a)-(c)**) and along z-axis (**(d)-(e)**). All spectra are recorded at temperature (T) $\sim$ 2 K and in absence of any applied magnetic field.

under 'z-axis PCS' configuration are presented along with their corresponding theoretical fits and extracted parameters. Some crucial observations are as follows. For all spectra that we have analyzed, the normal state contact resistance varied between $\sim$ 0.9 to 4.5 Ω. Using Wexler's formula [55] with these values, we found that the estimated contact diameter varied within a range from $\sim$ 12 to 27 nm. We did not find a direct correlation between the contact resistance R_c and the measured order parameter Δ. Furthermore, the spectra probed along the z-axis are visually more narrow and deep than those probed along the x-axis. Such spectra correspond to smaller values of the gap (Δ). The median values of Δ are 0.87 meV and 0.72 meV for x-axis and z-axis contacts, respectively. From our spectroscopic investigation, we confirm an anisotropy in the superconducting gap of ZrB_{12} but can not show any evidence of d-wave pairing symmetry or multigap superconductivity as a reason behind such anisotropy as predicted in a few reports [35, 36, 45, 46] earlier.

6.4.2 Temperature Dependence of Spectra

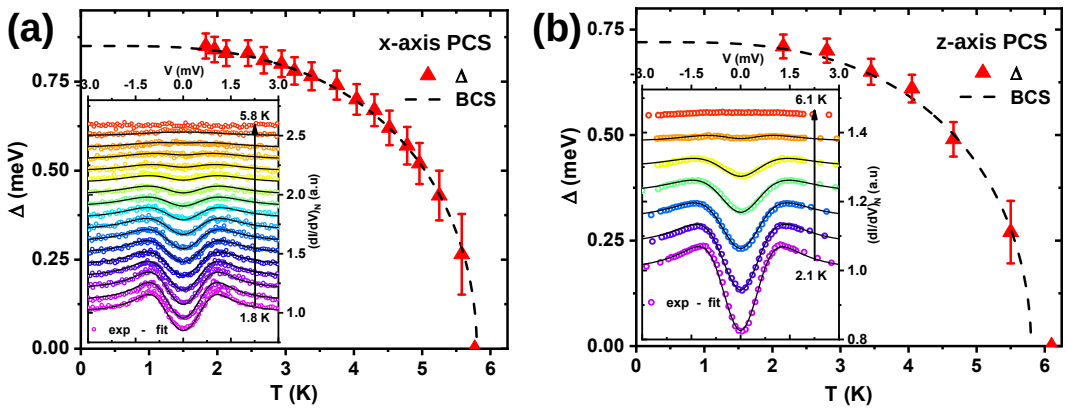

Figure 6.4.2: Evolution of the superconducting gap (Δ) with temperature (T). *Inset*: The T dependence of the conductance spectra and corresponding modified BTK fits. **(a)** For x-axis PCS and **(b)** for z-axis PCS.

In Fig. 6.4.2(a), the T dependence of Δ for x-axis PCS is represented. These data are extracted from the spectral data presented in the inset. Similar T dependence of the spectra for a z-axis PCS and the corresponding T dependence of

the extracted Δ are presented in Fig. 6.4.2(b). Modified BTK fit (black line) [53] for each spectrum is presented over the experimental data (colour circles). The expected temperature dependence for a conventional BCS superconductor [56] is presented as a dashed line along with each experimental Δ vs T plot. The extrapolated zero temperature gap amplitude $\Delta(0)$ and the junction critical temperature T_c^j are 0.85 meV (0.72 meV) and 5.8 K (5.9 K) for x-axis PCS (z-axis PCS), respectively. To note, although the superconducting gaps measured along the two different axes have differences in their spectral features and the extracted Δ values, they close nearly at the same temperature (T_c^j). Most importantly, in both cases, throughout the temperature range, the variations of Δs match extremely well with the corresponding BCS fits [56]. This further supports the conventional s-wave BCS superconductivity in ZrB_{12} in contrast to some previous claims of d-wave symmetry [35, 36] and pseudo-gap [57] above T_c. Our observation of conventional superconductivity in ZrB_{12} is also consistent with the previous PCARS measurements reported [32, 44] in this material.

6.4.3 Anisotropy in Critical Field

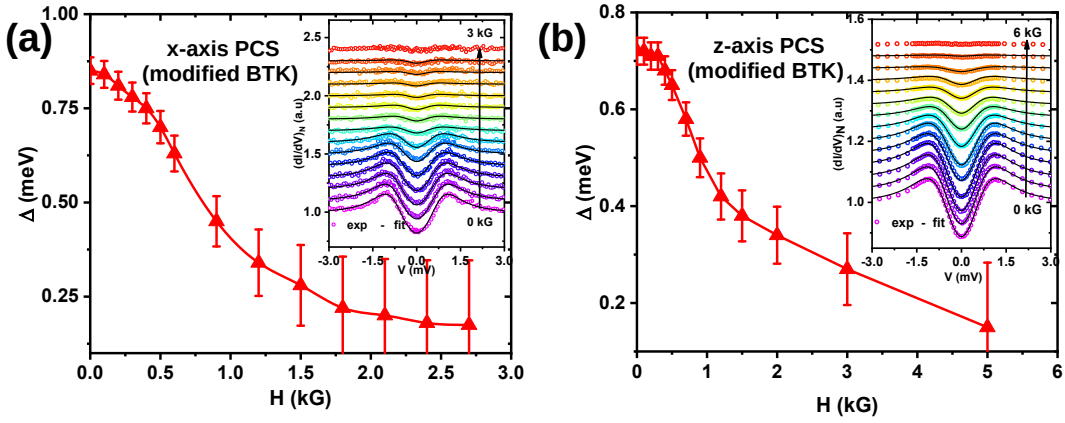

Figure 6.4.3: Evolution of Δ with magnetic field (H). *Inset*: The H dependence of the experimental dI/dV and corresponding modified BTK fits. **(a)** For x-axis PCS and **(b)** for z-axis PCS.

So far, we have seen that the visual features and the corresponding gap values for spectra belonging to x-axis and z-axis PCS are different, but their T_c^js are

almost identical. This is not a surprise because T_c is a global parameter [56] and, a unique superconductor ideally should have a unique T_c unaffected by any anisotropy. However, as already discussed, the same restriction does not apply to H_c, and to investigate further, we let the spectra probed on both surfaces evolve with an external magnetic field (H). In the inset of Fig. 6.4.3(a), we show the H dependence of the same x-axis PCS spectrum which was evolved with T in Fig. 6.4.2(a). With increasing H, the spectral features like the Andreev peaks and the in-between gap smoothly disappear. A modified BTK fit [53] (black line) is also presented over the experimental data (colour circles). The H dependence of Δ extracted from those fittings is shown in Fig. 6.4.3(a). Similar H dependence of the spectra for z-axis PCS (initial spectrum is same of Fig. 6.4.2(b), T dependence) and the corresponding H dependence of the extracted Δ are presented in Fig. 6.4.3(b). Interestingly, unlike T dependence, we found a clear anisotropy from the H dependence of the spectra. Although the field dependences of Δs visually look similar, the junction critical field $H_c^j \sim 3$ kG for x-axis PCS but ~ 6 kG for z-axis.

6.4.4 Anomalous Field Dependence of Barrier Potential

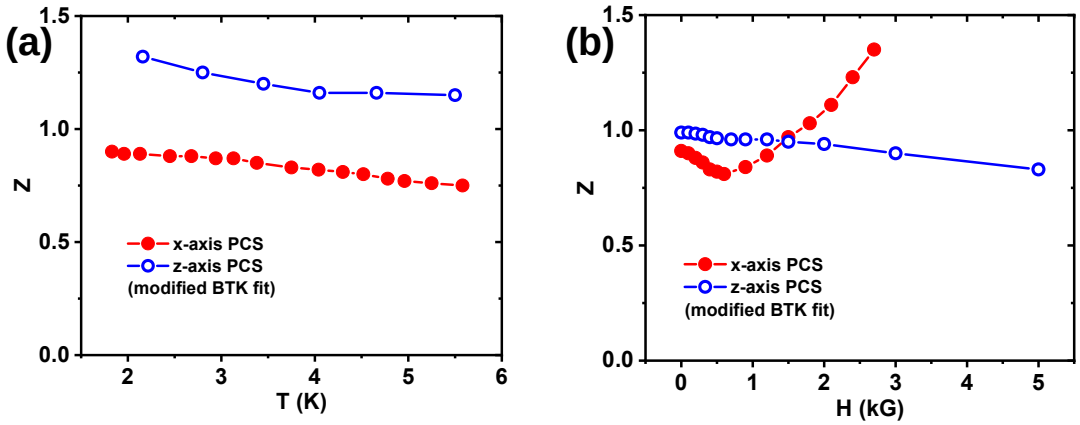

Figure 6.4.4: **(a)** Evolution of barrier potential Z with T as extracted from the modified BTK fits for x-axis (red solid circles) and z axis (blue open circles) experimental dI/dV (presented in Fig. 6.4.2 before). **(b)** Similar evolution of Z with H (from Fig. 6.4.3 before).

However, something interesting can be noticed from T and H dependence of

another parameter Z based on the same analysis. The results are represented in Fig. 6.4.4. As mentioned earlier, the parameter Z represents the barrier potential strength at the point contact. That means once a contact is formed and there is no relative motion between the tip and the sample to disturb that afterwards, changing T and H should not affect Z. As can be seen in Fig. 6.4.4(a), indeed increasing T does not have any significant effect on Z for both x and z axes PCS. As represented in Fig. 6.4.4(b), increasing H also does not have any significant effect in Z for z-axis PCS. But, for x-axis PCS, Z increases almost twofold from 1 kG field to 3 kG! In the next section we will try to understand the possible mechanism behind such unusual field dependence of Z.

6.4.5 Vortex Core Model

Apparently, the field-dependent divergence of Z seems unphysical considering the fitting model [53] we have used so far. But, in past, such field-dependent divergence of Z was reported in point contact even with an elemental superconductor. Miyoshi *et al.* reported [58] such observation in Nb-Cu point contacts. It was shown that the divergence of Z could be understood if the fitting model was modified to explicitly include the contribution of vortex cores in the experimentally measured conductance at finite magnetic field. Formation of vortex core at higher magnetic fields is indeed a likely scenario if the superconducting state is type-II in nature. We followed a similar treatment [58] and separated the contribution of the superconducting channel $(dI/dV)_{sc}$ from the experimental spectra (dI/dV) using the following relationship:

$$dI/dV = h(dI/dV)_{vor} + (1-h)(dI/dV)_{sc} \tag{6.1}$$

Here, $(dI/dV)_{vor}$ is the contribution of the normal channel due to the formation of vortex cores and $h = H/H_c^j$ with H_c^j is 3 kG for x-axis PCS. The results of the fittings [53] on such extracted $(dI/dV)_{sc}$ are presented in Fig. 6.4.5(a) (Δ vs. H) and Fig. 6.4.6(a) (Z vs. H). Although for z-axis PCS no enhancement of Z with magnetic field can be seen (previously in Fig 6.4.4(b)), for the sake of completeness, we also applied the 'vortex core model' [58] with $H_c^j = 6$ kG for z-axis PCS. The results of such analysis are presented in Fig. 6.4.5(b) (Δ vs. H) and Fig.

6.4.6(b) (Z vs. H). In both cases, no meaningful fittings seem to be possible due to high noise in the extracted $(dI/dV)_{sc}$ Beyond $\sim$ 2 kG. This is normal because at the higher field the relative contribution of the superconducting channel becomes increasingly negligible. As can be seen from Fig. 6.4.6(a), within the vortex core model, now Z remains almost constant with increasing field strength for x-axis PCS, thereby removing the rather unphysical situation of diverging Z. But, no noticeable change in the results can be seen in Fig. 6.4.6(b) after applying the vortex core-based model for the z-axis PCS.

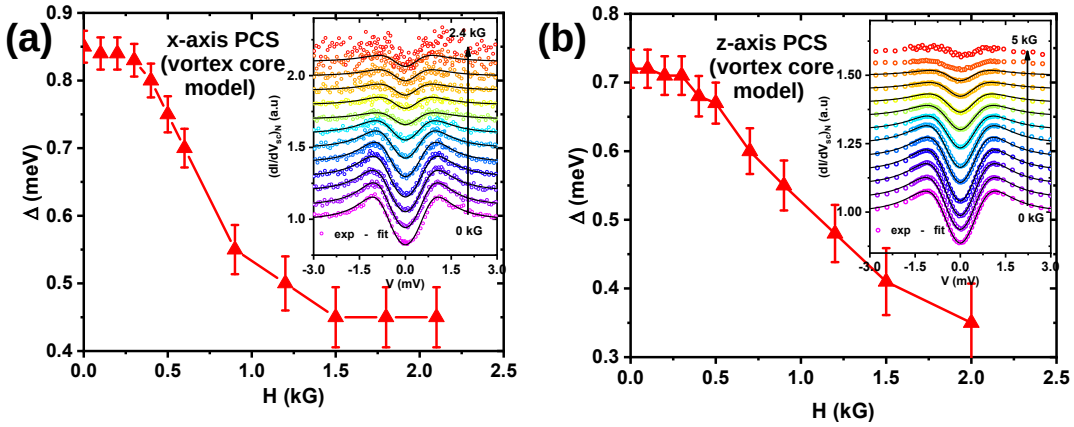

Figure 6.4.5: Evolution of Δ with H under 'vortex core model'. *Inset*: The H dependence of the extracted $(dI/dV)_{sc}$ after subtracting the contribution of vortex core from the experimental dI/dV. **(a)** For x-axis PCS and **(b)** for z-axis PCS.

From this analysis, we draw two important conclusions. First, we could understand the enhancement of Z with H for the x-axis spectra within a vortex core model [58]. Such enhancement was not seen for the z-axis spectra and hence a 'vortex core model' is not relevant in that case. When we still applied the model by brute force for z-axis spectra, as expected, no significant change in the H dependence of Z was seen. This observation hints to the possibility of the formation of vortex cores when the field is applied along x-axis, while the existence of vortices is not guaranteed (within the limit of our results) for the field applied along z-axis. This observation will be relevant for the discussion in the upcoming section. Second, the spectral gap Δ sharply falls within a field range of 0.5 to 1.5 kG for both

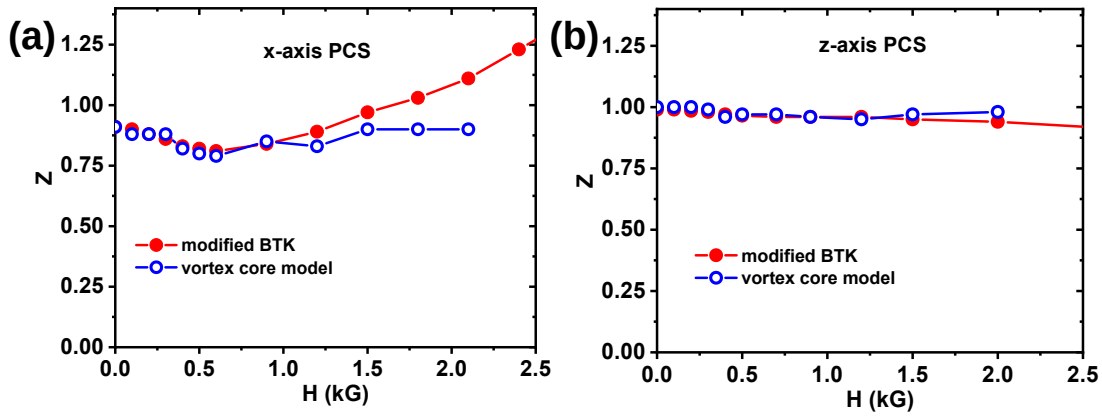

Figure 6.4.6: A comparison between the H dependences of parameter Z under modified BTK analysis of i) the experimental dI/dV (red solid circles) and ii) the extracted $(dI/dV)_{sc}$ under vortex core model (blue open circles). **(a)** For x-axis PCS and **(b)** for z-axis PCS.

x (Fig. 6.4.5(a)) and z axis (Fig. 6.4.5(b)) PCS which match extremely well to the reported values of the upper critical field $H_{c2}(0)$ (550 G - 1.5 kG) [19, 32, 35] for bulk ZrB_{12}. However, we also note that PCARS, which reveals the superconducting properties at a mesoscopic scale, is not an ideal technique to determine the critical field of a superconductor. To confirm the magnetic anisotropy in ZrB_{12}, we need to verify the same from a bulk sensitive measurement. For that purpose, we investigated the anisotropy of the screening properties with magnetic field angle.

6.5 AC Magnetic Susceptibility Measurements

Temperature-dependent χ measured by two-coils setup shows a sharp superconducting transition at $T = 5.9$ K. This transition temperature (T_c) is consistent with the previous reports [19, 30–36], and such a sharp transition supports the high purity of the single crystal we are using. In Fig. 6.5.1(a), the magnetic field dependence of such transition is shown. The static magnetic field was applied along the z-axis and was increased with 50 Gauss steps. With the increasing magnetic field, a clear shift of T_c towards lower temperature is visible. Each transition was recorded during zero-field cooled heating condition. Interestingly, at higher

field, a kink structure appears at the onset part of the transition, which seemingly breaks the transition curves in two parts. The possible reason behind such a kink is two independent transitions in the real (in phase) and imaginary (out of phase) parts of χ [32].

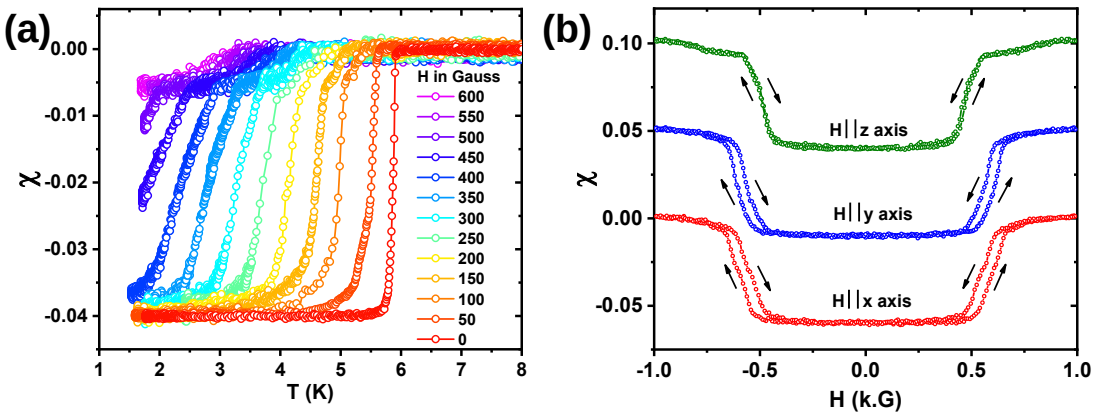

Figure 6.5.1: **(a)** External magnetic field (H) dependence of the bulk T_c from two-coil mutual inductance measurements.**(b)** Anisotropy in the H dependence of χ (at $T = 1.6$ K) showing hysteresis when $H \parallel$ x-axis or $H \parallel$ y-axis but no hysteresis when $H \parallel$ z-axis.

6.5.1 Type-I vs Type-II

In Fig. 6.5.1(b), the magnetic field dependence of χ is shown with temperature kept fixed at $T = 1.6$ K. When the magnetic field is applied along the z-axis, the superconducting transition starts at $H \sim 450$ G and completes at $H \sim 560$ G. No hysteresis can be observed in this case. An entirely different result is found when the magnetic field is applied along the x or y direction. For a clearer view in Fig. 6.5.1(b), plots for the $H \parallel$ y-axis and $H \parallel$ z-axis are vertically shifted, keeping the same scaling. Transition starts at $H \sim 485 \pm 25$ G and completes at $H \sim 645 \pm 25$ G for both x and y directions. The higher values are for increasing field, and the lower values are for decreasing fields, respectively. A clear hysteresis can be observed in both cases. As we have already mentioned, the reported thermodynamic critical field $H_c(0)$ of ZrB_{12} varies widely within a range of 300 - 415 G in literature [19, 33, 43]. In addition, the determination of exact $H_c(0)$

based on an ac technique is difficult because the transition curve highly depends on both the amplitude and frequency of the signal [43, 51]. Nevertheless, that dependence should not affect our observation of anisotropy because we kept the ac signal constant in the primary coil and changed only the temperature and the externally applied field as tuning parameters.

Hysteretic behavior in ZrB_{12} was seen in different contexts before too. For example, Tsindlekht *et al.* [43] mentioned about a tiny hysteresis loop they found near the critical field in their dc magnetization measurements but did not present that in their data. Based on their observation, the authors also concluded that the bulk ZrB_{12} could be either a type-I or a type-II superconductor as it has a marginal value of $\kappa \sim 0.71$. Wang *et al.* [19] also reported hysteresis both in field dependent specific heat and magnetization measurements within type-II/I temperature region. To note, intermediate state in type-I superconductor can also trap magnetic field in the similar way. But, the intermediate regions are macroscopic and will trap field applied from any direction. The observed hysteresis for $H \parallel$ x and $H \parallel$ y-axis can be attributed to formation of vortices and trapping-de-trapping phenomena of the same. The absence of hysteresis for $H \parallel$ z-axis, on the other hand, indicate that such vortex physics is absent for the given field direction. Therefore, we found indication of the possibility of a mixed state of type-II superconductivity for $H \parallel$ x and $H \parallel$ y-axis, and type-I superconductivity for $H \parallel$ z-axis in this material. Here we also note that, from our PCARS measurements, we found an anomalous, diverging magnetic field dependence of parameter Z for x-axis point contact which could be ultimately resolved when the contribution of the vortex channel to the conductance was excluded before analysis. Such diverging Z with magnetic field was not seen for z-axis PCS. This is also consistent with the idea of type-II superconductivity for $H \parallel$ x and y-axis but type-I superconductivity for $H \parallel z$-axis in ZrB_{12}. Recently Saraiva *et al.* [23] have theoretically shown that the idea of intertype superconductor (as I discussed in the introduction chapter) can also be applied for anisotropic superconductors. To make this work, an appropriate scaling transformation [24, 25] have to be introduced in the formalism describing the anisotropic superconductor. Such a transformation depends on the direction of the applied magnetic field. Consequently, the type of superconductivity may be

different for the magnetic field applied along different directions. This is precisely what we observed experimentally in ZrB_{12}.

6.5.2 Further Confirmation of Magnetic anisotropy

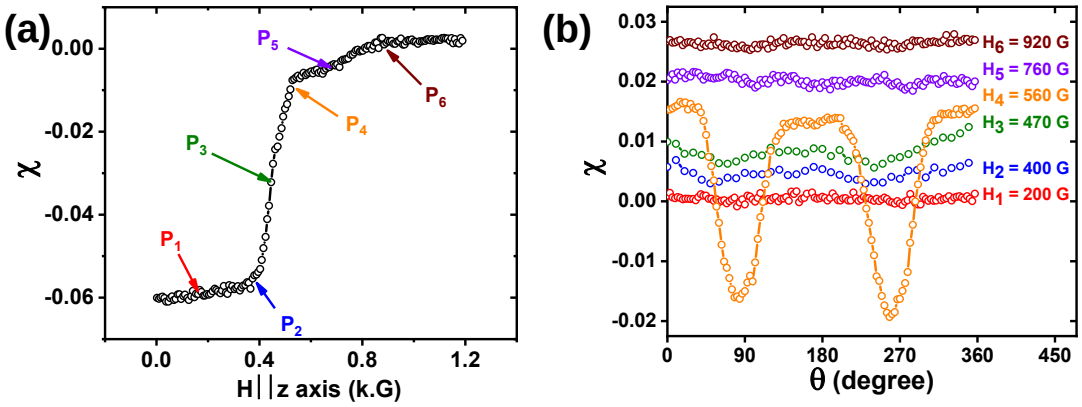

Figure 6.5.2: **(a)** Six points (P_1 - P_6) chosen on the $H \parallel$ z-axis plot in Fig. 6.5.1(b). **(b)** Angular dependence of χ (at $T = 1.6$ K) with six different values of magnetic fields (H_1 - H_6) corresponding to the six points (P_1 - P_6) chosen in (a).

To investigate the anisotropic behavior further, we performed field angle dependence of χ. We chose six unique points (P_1 - P_6) from the χ vs H plot for $H \parallel$ z-axis in Fig. 6.5.1(b). As described in Fig. 6.5.2(a), six such points correspond to six different magnetic field values (H_1 - H_6). For each point, we kept the magnitude of the magnetic field fixed but rotated the direction of the field in the $x-z$ plane. The temperature was kept fixed throughout the experiment at 1.6 K. In Fig. 6.5.2(b), we show the angular dependence of χ corresponding to these six field values H_1 to H_6. Angle θ is measured $w.r.t$ z-axis in the $z-x$ plane. Plots for higher fields are given vertical shifts for an uncluttered view. At $H_1 = 200$ G, the material is deep inside the superconducting domain and a flat angular dependence of χ is visible. Similar flat dependence is visible at $H_6 = 920$ G when the sample is in the normal state. From $H_2 = 400$ G to $H_5 = 760$ G, when the material passes through the superconducting transition, a clear two-fold symmetry appears and then disappears with increasing H. The maximum anisotropy was found at $H_4 = 560$ G. At this field $H \parallel z$-axis, the normal state is just critically reached

(see point P_4 in Fig. 6.5.2(a)). However, the material is still superconducting at the same field value when $H \parallel x$-axis (or y-axis), as shown in Fig. 6.5.2(b). In Section 6.E of the appendix, different aspects of the anisotropy we probed will be discussed in detail. In summary, the directional PCARS and field-angle dependent χ measurements collectively confirm that the observed anisotropic behavior in ZrB_{12} does not originate from extrinsic geometry-driven effects, but is indeed an intrinsic property of the material system itself.

6.6 Summary

Through point contact Andreev reflection spectroscopy and ac susceptibility measurements, we investigated the anisotropy in the superconducting properties of ZrB_{12}. Based on our PCARS experiments, we found $2\Delta/k_BT_c \sim 2.8$ and $H_{cl} \sim 6$ kG along a primary axis (001) of a single crystal and $2\Delta/k_BT_c \sim 3.4$ and $H_{cl} \sim 3$ kG in a perpendicular direction. The spectra fit well with a single-gap s-wave BTK model [52, 53], and the extracted gaps in both cases obey ideal BCS temperature dependence [56] with high fidelity. From our extensive investigation of magnetic field-dependent spectra, we also found evidence of vortex cores along the (001) direction but not in the perpendicular direction in this material. Further, based on our ac susceptibility measurements, We found a non-hysteretic type-I like transition for the field applied in the (001) direction, but a hysteretic type-II like transition for the field applied in perpendicular directions. From the same experiment, an angular two-fold symmetry in the magnetic susceptibility is also reported. Based on these findings, we surmise that the superconducting ZrB_{12} possesses a magnetic anisotropy that can be utilised to modify its superconducting state and superconducting type just by changing the applied field's direction. This is the central concept of the formalism for an anisotropic intertype superconductor developed by Saraiva *et al.* [23]. Here, we have provided the experimental evidence of the same utilising ZrB_{12} as a model system. Our findings will be further useful in investigating the controlled magnetic behavior of other superconductors with a marginal Ginzburg-Landau parameter.

Acknowledgements

Arushi and Dr. Ravi Prakash Singh from IISER Bhopal synthesized the single crystal. Sandeep Howlader and Ranjani Ramachandran are duly acknowledged for their help during the low temperature experiments. We thank Dr. Shirshendu Gayen for his contribution in the instrument interfacing and data fitting programmes. We are grateful to the anonymous reviewer of journal *Physical Review B* who helped us understand the field-dependent PCS data better.

Addendum

The work presented in this chapter was published [1] in *Physical Review B* in March 2022. In April 2022, Krasikov *et al.* [59] reported a comparison of the Fermi surface topologies between ZrB_{12} and its isostructural LuB_{12}, based on magnetoresistance measurements. The authors pointed out the lower anisotropy in the former compared to the latter. We already mentioned the lower anisotropy of ZrB_{12} Fermi surface in comparison with MgB_2 based on previous reports (see the first paragraph, Section 6.1.2). We also argued that such Fermi surface topology of ZrB_{12} validates the prototype ellipsoidal Fermi surface model by Saraiva *et al.* [23] to be used on this material. In July 2022, Zhang *et al.* [60] reported a detailed vortex matter study on ZrB_{12}. The authors concluded that their findings could not be described within a framework of classical type-II superconductivity, and they argued about type-1.5 superconductivity in this material. Our results already pointed out that the superconductivity in ZrB_{12} can neither be described as a purely type-I nor a type-II, but rather an intertype one.

Bibliography

[1] Soumya Datta, Sandeep Howlader, Ravi Prakash Singh, Goutam Sheet, et al. Anisotropic superconductivity in ZrB_{12} near the critical Bogomolnyi point. *Physical Review B*, 105(9):094504, 2022.

[2] Lev Davidovich Landau and Vitaly Lazarevich Ginzburg. On the theory of superconductivity. *Zh. Eksp. Teor. Fiz.*, 20:1064, 1950.

[3] Vitaly L Ginzburg and Lev D Landau. On the theory of superconductivity. In *On Superconductivity and Superfluidity*, pages 113–137. Springer, 2009.

[4] Alexei A Abrikosov. On the magnetic properties of superconductors of the second group. *Sov. Phys. JETP*, 5:1174–1182, 1957.

[5] Aleksej A Abrikosov. Nobel lecture: Type-II superconductors and the vortex lattice. *Reviews of Modern Physics*, 76(3):975, 2004.

[6] Michael Tinkham. *Introduction to superconductivity*. Courier Corporation, 2004.

[7] U Krägeloh. Flux line lattices in the intermediate state of superconductors with Ginzburg Landau parameters near $1/\sqrt{2}$. *Physics Letters A*, 28(9):657–658, 1969.

[8] U Essmann. Observation of the mixed state. *Physica*, 55:83–93, 1971.

[9] DR Aston, LW Dubeck, and F Rothwarf. Intermediate mixed state of type-II superconductors. *Physical Review B*, 3(7):2231, 1971.

[10] AE Jacobs. Interaction of vortices in type-II superconductors near T = T_C. *Physical Review B*, 4(9):3029, 1971.

[11] J Auer and H Ullmaier. Magnetic behavior of type-II superconductors with small Ginzburg-Landau parameters. *Physical Review B*, 7(1):136, 1973.

[12] I Luk'yanchuk. Theory of superconductors with κ close to $1/\sqrt{2}$. *Physical Review B*, 63(17):174504, 2001.

[13] EB Bogomol'Nyi. The stability of classical solutions. *Sov. J. Nucl. Phys.(Engl. Transl.);(United States)*, 24(4), 1976.

[14] Laurence Jacobs and Claudio Rebbi. Interaction energy of superconducting vortices. *Physical Review B*, 19(9):4486, 1979.

[15] Alexei Vagov, AA Shanenko, MV Milošević, Vollrath M Axt, VM Vinokur, J Albino Aguiar, and FM Peeters. Superconductivity between standard types: Multiband versus single-band materials. *Physical Review B*, 93(17):174503, 2016.

[16] WY Córdoba-Camacho, RM da Silva, A Vagov, AA Shanenko, and J Albino Aguiar. Between types I and II: Intertype flux exotic states in thin superconductors. *Physical Review B*, 94(5):054511, 2016.

[17] Sebastian Wolf, Alexei Vagov, AA Shanenko, Vollrath M Axt, A Perali, and J Albino Aguiar. BCS-BEC crossover induced by a shallow band: Pushing standard superconductivity types apart. *Physical Review B*, 95(9):094521, 2017.

[18] Sebastian Wolf, Alexei Vagov, AA Shanenko, Vollrath M Axt, and J Albino Aguiar. Vortex matter stabilized by many-body interactions. *Physical Review B*, 96(14):144515, 2017.

[19] Yuxing Wang, Rolf Lortz, Yuriy Paderno, Vladimir Filippov, Satoko Abe, Ulrich Tutsch, and Alain Junod. Specific heat and magnetization of a ZrB_{12} single crystal: Characterization of a type-II/1 superconductor. *Physical Review B*, 72(2):024548, 2005.

[20] Jun-Yi Ge, Joffre Gutierrez, A Lyashchenko, V Filipov, Jun Li, and Victor V Moshchalkov. Direct visualization of vortex pattern transition in ZrB_{12} with Ginzburg-Landau parameter close to the dual point. *Physical Review B*, 90(18):184511, 2014.

[21] Jun-Yi Ge, Vladimir N Gladilin, Nikolay E Sluchanko, A Lyashenko, Volodimir B Filipov, Joseph O Indekeu, and Victor V Moshchalkov. Paramagnetic meissner effect in ZrB_{12} single crystal with non-monotonic vortex–vortex interactions. *New Journal of Physics*, 19(9):093020, 2017.

[22] PK Biswas, Filipp N Rybakov, RP Singh, Saumya Mukherjee, N Parzyk, G Balakrishnan, MR Lees, CD Dewhurst, Egor Babaev, AD Hillier, et al. Coexistence of type-I and type-II superconductivity signatures in ZrB_{12} probed by muon spin rotation measurements. *Physical Review B*, 102(14):144523, 2020.

[23] Tiago T Saraiva, Alexei Vagov, Vollrath Martin Axt, J Albino Aguiar, and AA Shanenko. Anisotropic superconductors between types I and II. *Physical Review B*, 99(2):024515, 2019.

[24] Richard A Klemm and John R Clem. Lower critical field of an anisotropic type-II superconductor. *Physical Review B*, 21(5):1868, 1980.

[25] Gianni Blatter, Vadim B Geshkenbein, and AI Larkin. From isotropic to anisotropic superconductors: a scaling approach. *Physical Review Letters*, 68(6):875, 1992.

[26] A Leithe-Jasper, A Sato, and T Tanaka. Refinement of the crystal structure of Zirconium dodecaboride, ZrB_{12}, at 140 K and 293 K. *Zeitschrift für Kristallographie-New Crystal Structures*, 217(1):319–320, 2002.

[27] Koichi Momma and Fujio Izumi. VESTA 3 for three-dimensional visualization of crystal, volumetric and morphology data. *Journal of Applied Crystallography*, 44(6):1272–1276, 2011.

[28] Benjamin Post and Frank W Glaser. Crystal structure of ZrB_{12}. *JOM*, 4(6):631–632, 1952.

[29] Colin HL Kennard and Lindsay Davis. Zirconium dodecarborides ZrB_{12}. confirmation of the B_{12} cubooctahedral unit. *Journal of Solid State Chemistry*, 47(1):103–106, 1983.

[30] BT Matthias, TH Geballe, K Andres, E Corenzwit, GW Hull, and JP Maita. Superconductivity and antiferromagnetism in Boron-rich lattices. *Science*, 159(3814):530–530, 1968.

[31] Vitalii Agasievich Gasparov, MP Kulakov, NS Sidorov, II Zver'kova, VB Filipov, AB Lyashenko, and Yu B Paderno. On electron transport in ZrB_{12}, ZrB_2, and MgB_2 in normal state. *Journal of Experimental and Theoretical Physics Letters*, 80(5):330–334, 2004.

[32] D Daghero, RS Gonnelli, GA Ummarino, A Calzolari, Valeria Dellarocca, VA Stepanov, VB Filippov, and Yu B Paderno. Andreev-reflection spectroscopy in ZrB_{12} single crystals. *Superconductor Science and Technology*, 17(5):S250, 2004.

[33] R Lortz, Y Wang, S Abe, C Meingast, Yu B Paderno, V Filippov, and A Junod. Specific heat, magnetic susceptibility, resistivity and thermal expansion of the superconductor ZrB_{12}. *Physical Review B*, 72(2):024547, 2005.

[34] Rustem Khasanov, Daniele Di Castro, M Belogolovskii, Yu Paderno, V Filippov, Rudolf Brütsch, and Hugo Keller. Anomalous electron-phonon coupling probed on the surface of superconductor ZrB_{12}. *Physical Review B*, 72(22):224509, 2005.

[35] VA Gasparov, NS Sidorov, II Zver'kova, SS Khassanov, and MP Kulakov. Electron transport, penetration depth, and the upper critical magnetic field in ZrB_{12} and MgB_2. *Journal of Experimental and Theoretical Physics*, 101(1):98–106, 2005.

[36] VA Gasparov, NS Sidorov, and II Zver'Kova. Two-gap superconductivity in ZrB_{12}: temperature dependence of critical magnetic fields in single crystals. *Physical Review B*, 73(9):094510, 2006.

[37] Z Fisk, AC Lawsom, BT Matthias, and E Corenzwit. Superconducting isotope effect in ZrB_{12}. *Physics Letters A*, 37(3):251–252, 1971.

[38] IR Shein and AL Ivanovskii. Band structure of superconducting dodecaborides YB_{12} and ZrB_{12}. *Physics of the Solid State*, 45(8):1429–1434, 2003.

[39] Jérémie Teyssier, AB Kuzmenko, Dirk Van Der Marel, Frank Marsiglio, AB Liashchenko, N Shitsevalova, and V Filippov. Optical study of electronic structure and electron-phonon coupling in ZrB_{12}. *Physical Review B*, 75(13):134503, 2007.

[40] VA Gasparov, I Sheikin, F Levy, J Teyssier, and G Santi. Study of the fermi surface of ZrB_{12} using the de Haas-van Alphen effect. *Physical Review Letters*, 101(9):097006, 2008.

[41] Jens Kortus, II Mazin, Kirill D Belashchenko, Vladimir P Antropov, and LL Boyer. Superconductivity of metallic Boron in MgB_2. *Physical Review Letters*, 86(20):4656, 2001.

[42] Thomas Dahm and N Schopohl. Fermi surface topology and the upper critical field in two-band superconductors: Application to MgB_2. *Physical Review Letters*, 91(1):017001, 2003.

[43] MI Tsindlekht, GI Leviev, I Asulin, A Sharoni, O Millo, I Felner, Yu B Paderno, VB Filippov, and MA Belogolovskii. Tunneling and magnetic characteristics of superconducting ZrB_{12} single crystals. *Physical Review B*, 69(21):212508, 2004.

[44] J Girovskỳ, P Szabo, T Mori, and P Samuely. Strong-coupling features in YB_6 and ZrB_{12} studied by point-contact spectroscopy. *Acta Physica Polonica-Series A General Physics*, 118(5):1042, 2010.

[45] Nikolai Efimovich Sluchanko, AN Azarevich, Aleksei Viktorovich Bogach, S Yu Gavrilkin, Vladimir Vital'evich Glushkov, Sergei Vasil'evich Demishev, AV Dukhnenko, AB Lyashchenko, Kirill Vladimirovich Mitsen, and VB Filipov. ^{10}B-^{11}B isotope substitution and superconductivity in ZrB_{12}. *JETP letters*, 94(8):642–646, 2011.

[46] NB Bolotina, ON Khrykina, AN Azarevich, N Yu Shitsevalova, VB Filipov, S Yu Gavrilkin, KV Mitsen, VV Voronov, and NE Sluchanko. Checkerboard patterns of charge stripes in the two-gap superconductor ZrB_{12}. *Physical Review B*, 105(5):054511, 2022.

[47] Mihail Silaev and Egor Babaev. Microscopic theory of type-1.5 superconductivity in multiband systems. *Physical Review B*, 84(9):094515, 2011.

[48] AF Andreev. The thermal conductivity of the intermediate state in superconductors. *Soviet Physics-JETP*, 19(5):1228–1231, 1964.

[49] Yu G Naidyuk, Jurij G Najdjuk, and IK Yanson. *Point-contact spectroscopy*, volume 145. Springer Science & Business Media, 2005.

[50] Grigory I Leviev, Valery M Genkin, Menachem I Tsindlekht, Israel Felner, Yurii B Paderno, and Vladimir B Filippov. Low-frequency response in the surface superconducting state of single-crystal ZrB_{12}. *Physical Review B*, 71(6):064506, 2005.

[51] Menachem I Tsindlekht, Grigory I Leviev, Valery M Genkin, Israel Felner, Yurii B Paderno, and Vladimir B Filippov. Glasslike low-frequency ac response of ZrB_{12} and Nb single crystals in the surface superconducting state. *Physical Review B*, 73(10):104507, 2006.

[52] GE Blonder, m M Tinkham, and k TM Klapwijk. Transition from metallic to tunneling regimes in superconducting microconstrictions: Excess current, charge imbalance, and supercurrent conversion. *Physical Review B*, 25(7):4515, 1982.

[53] A Plecenik, M Grajcar, S Benacka, and P Seidel. Finite-quasiparticle-lifetime effects in the differential conductance of $Bi_2Sr_2CaCu_2O_y$/Au junctions. *Physical Review B*, 49:10016, 1994.

[54] Goutam Sheet, S Mukhopadhyay, and Pratap Raychaudhuri. Role of critical current on the point-contact andreev reflection spectra between a normal metal and a superconductor. *Physical Review B*, 69(13):134507, 2004.

[55] G Wexler. The size effect and the non-local boltzmann transport equation in orifice and disk geometry. *Proceedings of the Physical Society (1958-1967)*, 89(4):927, 1966.

[56] John Bardeen, Leon N Cooper, and John Robert Schrieffer. Theory of superconductivity. *Physical Review*, 108(5):1175, 1957.

[57] Sangeeta Thakur, Deepnarayan Biswas, Nishaina Sahadev, PK Biswas, G Balakrishnan, and Kalobaran Maiti. Complex spectral evolution in a BCS superconductor, ZrB_{12}. *Scientific reports*, 3(1):1–6, 2013.

[58] Y Miyoshi, Y Bugoslavsky, and LF Cohen. Andreev reflection spectroscopy of niobium point contacts in a magnetic field. *Physical Review B*, 72(1):012502, 2005.

[59] KM Krasikov, MA Makrushin, SV Demishev, VB Filippov, N Yu Shitsevalova, and NE Sluchanko. Influence of the fermi surface shape on magnetoresistance anisotropy in ZrB_{12}. In *Doklady Physics*, volume 67, pages 11–14. Springer, 2022.

[60] An-Lei Zhang, Li-Xin Gao, Jing-Yu He, Volodimir B Filipov, Shixun Cao, Qi-Ling Xiao, and Jun-Yi Ge. Experimental evidence for type-1.5 superconductivity in ZrB_{12} single crystal. *Science China Physics, Mechanics & Astronomy*, 65(9):1–9, 2022.

Appendix

6.A Possibility of Multiband Superconductivity

Recently, two unique checkerboard charge stripe patterns were reported in ZrB_{12} [1]. Static Jahn-Teller distortions in the crystal structure and a consequent anisotropic charge transfer that depends on different bond directions were argued as a possible mechanism behind that. Interestingly, in the same paper [1], the authors compared two different directions [100] and [110] and reported a signature of two-gap superconductivity (the ratios $2\Delta_1/k_BT_c = 6$ and $2\Delta_2/k_BT_c = 2.5$ respectively) based on their heat capacity study. This observation is compelling because we also found similar anisotropy based on our directional PCARS measurements. However, the anisotropy we observed is not that high ($2\Delta/k_BT_c \sim 3.4$ for x-axis PCS and 2.8 for z-axis PCS). The superconducting gap is an energy-resolved quantity, and heat capacity measurement (unlike PCARS or STS) is not a direct energy-resolved technique to confirm the existence of multiple gaps in a material. A pair of gaps, if they are such widely separated in the energy scale (as reported by [1]), is expected to be resolved spectroscopically, particularly when the measurements are performed down to a temperature that is $\sim 33\%$ of T_c. In our data, no typical multigap features [2] were visible. In our case, all spectra, irrespective of the surface they were probed on, can be described well within the single gap s-wave BTK formalism [3, 4]. Therefore, our measurements do not confirm the possibility of multigap superconductivity in ZrB_{12}. Nevertheless, as usual, the possibility of multiple gaps existing very close to each other in the energy scale cannot be strictly ruled out within the limits of the PCAR experiments.

6.B Discussion about Coupling Strength

As we already have mentioned, the superconducting coupling strength of ZrB_{12} varies widely among previous reports [5–12]. This is still an unresolved issue, and new insights are still being proposed regarding that. From our spectral analysis, we found $2\Delta/k_BT_c \sim 3.4$ for x-axis PCS and 2.8 for z-axis PCS, which indicates a weak coupling behavior. The larger value matches with the previous reports by Lortz *et al.* [9], Wang *et al.* [13] and Teyssier *et al* [10]. The smaller value agrees with the recent report by Bolotina *et al.* [1] corresponding to the smaller band in the two-band picture proposed by the authors. None of these two values matches with any previous report (including the previous PCARS studies [5, 12]) arguing a strong coupling behaviour [5–7, 10–12]. It is surprising because PCARS is a surface sensitive technique [14], and ZrB_{12} is considered to have a surface enhancement of superconductivity [6, 8]. While it is not possible to precisely explain the origin of the difference, we may make some speculative comments in this context.

One of the distinguishing features of our investigation is that we have performed much more extensive studies (compared to Ref. [5, 12]) and have been able to record clean spectroscopic data, free from the prominent effects of the Maxwell's resistance. The conductance dips appearing in Fig. 5 of Ref. [5] are known to originate from the contribution of the critical current when the contacts are not strictly in the spectroscopic regime [15, 16]. As a consequence, the Andreev reflection features appearing at lower bias are also less prominent. In such cases, a BTK fitting of the spectra may give an overestimated gap [15]. In Fig. 1(b) of Ref. [12], only two PCAR spectra of ZrB_{12} have been presented. A visual inspection of the data *vis-a-vis* the BTK fits reveal that while the fitting for the low-bias parts were good, the fits deviate noticeably at the higher bias. This discrepancy might also lead to an overestimated gap. However, these are purely speculative comments on the data reported by other groups and we believe that the extensive studies made by us complement the existing PCAR literature on ZrB_{12}.

6.C Discussion about Critical Field

In the main chapter, we have seen that the spectral gap Δ sharply falls within a field range of 0.5 to 1.5 kG for both x and z axis (Fig. 6.4.5 (a) and (b) in the main chapter) PCS. This field scale is similar to the reported values of the upper critical field $H_{c2}(0)$ (550 G - 1.5 kG) [5, 13, 17] for bulk ZrB_{12}. However, we also note that the local critical field $H_{c(l)}$ measured from the PCARS experiments, defined as the field where the gap feature completely vanishes, is much larger than 1.5 kG irrespective of the direction of the applied magnetic field. In fact, the critical fields thus measured are an order of magnitude larger than the the bulk critical field (as reported by other groups [6, 9, 13] and also from our χ measurements discussed in Section 6.5 of the main chapter) of ZrB_{12}. According to previous reports, $H_{c2}(0)$ varies widely based on different measurement techniques employed. This aspect of critical field variation was addressed by different authors with different proposed mechanisms. Bolotina *et al.* [1], based on their heat capacity measurements, attributed this variation to a two-gap scenario. To resolve the puzzle regarding the electron-phonon coupling strength in this material, some authors also have proposed a third dramatically enhanced $H_{c3}(0)$ within a framework of surface enhancement of superconductivity [6, 13]. Under such circumstances, PCAR experiments are expected to be influenced by the enhanced surface critical field. Also the factors like the confined dimension of the point contact geometry and the enhanced local disorder under a point contact can contribute to the difference between $H_{c(l)}$ and H_c. In the experiments, either all or some of these factors lead to the measurement of an enhanced critical field $H_{c(l)}$ on superconducting point contacts.

6.D Absence of a type-I Like Transition in PCARS

In case of type-I superconductors, it is often expected that the superconducting gap would show a sharp first-order disappearance with increasing magnetic field. Such an effect was earlier seen in the type-I phase of a number of superconductors [18–20]. On the other hand, the observation of the first-order destruction of superconductivity is often limited in PCAR experiments because the presence of

the non-superconducting tip may cause an enhanced local disorder, especially for the fact that a point contact is effectively a mesoscopic entity with confinement. Enhancement of local disorder decreases the local mean free path, which in turn reduces the local coherence length of the superconducting fraction of the point contact, thereby driving the superconductor locally to the type-II regime (large G-L parameter κ). Consequently, even a strictly type-I superconductor like Pb often loses its type-I behavior in mesoscopic dimensions [21–24]. For ZrB_{12}, as κ is very close to the critical value $1/\sqrt{2}$ [13], a small disorder introduced by the tip is enough to drive the system to the type-II regime locally. We believe that this is why we did not observe the sudden destruction of the superconducting gap in ZrB_{12} with field, from our z-axis PCARS studies.

6.E Further Discussion on Anisotropy

To summarize the previous chapter, we used two experimental tools, (a) directional PCARS and (b) field-angle dependent ac χ measurements on ZrB_{12}, and as a result, we found anisotropies in (a) superconducting gap, (b) critical field, and (c) superconducting type in this material. Regarding these findings, a few questions can normally come to mind. First, as ZrB_{12} has a cubic (fcc of space group $Fm\bar{3}m$) structure [25–27], how can it host anisotropy between two different lattice directions? The answer to this question is that the two directions we are talking about, though mutually perpendicular, are not two analogous cubic axes. One of them is indeed [001], but the other one is apparently [110], which is slanted between [100] and [010]. Such preparation of sample faces (perpendicular to the two directions) was intentional because, otherwise, performing experiments on [100], [010] and [001] on a cubic crystal should not make any difference. Interestingly, Bolotina *et al.* [1] recently also reported the anisotropy in H_{c2} (between [110] and [100] directions) in ZrB_{12} based on heat capacity measurements. It should be noted that in the same paper the authors also reported static Jahn-Teller distortions in the crystal structure of ZrB_{12}, which can drive the otherwise cubic structure effectively to an anisotropic non-cubic one. Our observed anisotropy might be associated with that effect also.

Second, can the anisotropy we are observing be due to the shape/geometry of the sample? This question is particularly relevant to the two-fold angular symmetry we have observed in χ (Fig. 6.5.2(b) in the main chapter). If the field is rotated from a direction of large demagnetization to a direction of small demagnetization for a sample with high shape anisotropy (not true for our sample, though), such two-fold anisotropy can be detected. Still, due to primarily two reasons, we can safely ignore such a possibility. First of all, anisotropic demagnetization, if exists, would modify the magnitude of the susceptibility (i.e. change the signal height in Fig. 6.5.1 (b), main chapter) but not change the critical field (i.e. no change in the signal width in Fig. 6.5.1 (b)). As we can see from Fig. 6.5.1 (b), there is clear anisotropy in the critical field; the same must be reflected in the angular dependence in Fig. 6.5.2. The two-fold symmetry in Fig. 6.5.2 (b) provides the same information in a continuous manner which Fig. 6.5.1 (b) indicates in a discrete way. In addition, if the anisotropy found from these bulk measurements was due to the sample shape, the same reason can not explain the anisotropy we also found from point contact measurements which is a mesoscopic technique free from the overall sample shape.

Third, can the anisotropy be due to the differences in surface quality between the two facets of the sample? This question is relevant to the directional PCARS we have used. It is true that the shape of spectra and the local critical field probed by point contact measurement indeed get affected by surface cleanliness. To reduce such possibility, we cleaned the sample surfaces (and the freshly cut tip) with 1500 - 2000 Grit fine sandpaper, sonicated those in isopropyl alcohol, created the point contact in situ at low temperature, and constructed the contact at various points on the surfaces. Our quality of the spectra (high signal-to-noise ratio), their high reproducibility within the ballistic regime and consistent spectral T_c with bulk T_c both for x and z axes PCS ensures pristine surface in both cases. Also, if the anisotropy found from directional point-contact measurements was solely due to the surface inhomogeneity, the same reason can not explain the anisotropy we also found from χ measurements which is a bulk-sensitive technique free from surface artefacts.

The surface-sensitive directional PCARS and the bulk-sensitive field-angle dependent χ measurements collectively confirm that the observed anisotropic behaviour in ZrB_{12} can not originate from extrinsic geometry-driven effects and must be an intrinsic property of the material system itself.

Bibliography

[1] NB Bolotina, ON Khrykina, AN Azarevich, N Yu Shitsevalova, VB Filipov, S Yu Gavrilkin, KV Mitsen, VV Voronov, and NE Sluchanko. Checkerboard patterns of charge stripes in the two-gap superconductor ZrB_{12}. *Physical Review B*, 105(5):054511, 2022.

[2] D Daghero and RS Gonnelli. Probing multiband superconductivity by point-contact spectroscopy. *Superconductor Science and Technology*, 23(4):043001, 2010.

[3] GE Blonder, m M Tinkham, and k TM Klapwijk. Transition from metallic to tunneling regimes in superconducting microconstrictions: Excess current, charge imbalance, and supercurrent conversion. *Physical Review B*, 25(7):4515, 1982.

[4] A Plecenik, M Grajcar, S Benacka, and P Seidel. Finite-quasiparticle-lifetime effects in the differential conductance of $Bi_2Sr_2CaCu_2O_y$/Au junctions. *Physical Review B*, 49:10016, 1994.

[5] D Daghero, RS Gonnelli, GA Ummarino, A Calzolari, Valeria Dellarocca, VA Stepanov, VB Filippov, and Yu B Paderno. Andreev-reflection spectroscopy in ZrB_{12} single crystals. *Superconductor Science and Technology*, 17(5):S250, 2004.

[6] MI Tsindlekht, GI Leviev, I Asulin, A Sharoni, O Millo, I Felner, Yu B Paderno, VB Filippov, and MA Belogolovskii. Tunneling and magnetic characteristics of superconducting ZrB_{12} single crystals. *Physical Review B*, 69(21):212508, 2004.

[7] Vitalii Agasievich Gasparov, MP Kulakov, NS Sidorov, II Zver'kova, VB Filipov, AB Lyashenko, and Yu B Paderno. On electron transport in ZrB_{12}, ZrB_2, and MgB_2 in normal state. *Journal of Experimental and Theoretical Physics Letters*, 80(5):330–334, 2004.

[8] Rustem Khasanov, Daniele Di Castro, M Belogolovskii, Yu Paderno, V Filippov, Rudolf Brütsch, and Hugo Keller. Anomalous electron-phonon coupling probed on the surface of superconductor ZrB_{12}. *Physical Review B*, 72(22):224509, 2005.

[9] R Lortz, Y Wang, S Abe, C Meingast, Yu B Paderno, V Filippov, and A Junod. Specific heat, magnetic susceptibility, resistivity and thermal expansion of the superconductor ZrB_{12}. *Physical Review B*, 72(2):024547, 2005.

[10] Jérémie Teyssier, AB Kuzmenko, Dirk Van Der Marel, Frank Marsiglio, AB Liashchenko, N Shitsevalova, and V Filippov. Optical study of electronic structure and electron-phonon coupling in ZrB_{12}. *Physical Review B*, 75(13):134503, 2007.

[11] VA Gasparov, I Sheikin, F Levy, J Teyssier, and G Santi. Study of the fermi surface of ZrB_{12} using the de Haas-van Alphen effect. *Physical Review Letters*, 101(9):097006, 2008.

[12] J Girovskỳ, P Szabo, T Mori, and P Samuely. Strong-coupling features in YB_6 and ZrB_{12} studied by point-contact spectroscopy. *Acta Physica Polonica-Series A General Physics*, 118(5):1042, 2010.

[13] Yuxing Wang, Rolf Lortz, Yuriy Paderno, Vladimir Filippov, Satoko Abe, Ulrich Tutsch, and Alain Junod. Specific heat and magnetization of a ZrB_{12} single crystal: Characterization of a type-II/1 superconductor. *Physical Review B*, 72(2):024548, 2005.

[14] Yu G Naidyuk, Jurij G Najdjuk, and IK Yanson. *Point-contact spectroscopy*, volume 145. Springer Science & Business Media, 2005.

[15] Goutam Sheet, S Mukhopadhyay, and Pratap Raychaudhuri. Role of critical current on the point-contact andreev reflection spectra between a normal metal and a superconductor. *Physical Review B*, 69(13):134507, 2004.

[16] Ritesh Kumar and Goutam Sheet. Nonballistic transport characteristics of superconducting point contacts. *Physical Review B*, 104(9):094525, 2021.

[17] VA Gasparov, NS Sidorov, II Zver'kova, SS Khassanov, and MP Kulakov. Electron transport, penetration depth, and the upper critical magnetic field in ZrB_{12} and MgB_2. *Journal of Experimental and Theoretical Physics*, 101(1):98–106, 2005.

[18] Yu G Naidyuk, H v Löhneysen, and IK Yanson. Temperature and magnetic-field dependence of the superconducting order parameter in Zn studied by point-contact spectroscopy. *Physical Review B*, 54(22):16077, 1996.

[19] Yu G Naidyuk, R Häussler, and HV Löhneysen. Magnetic field dependence of the andreev reflection structure in the conductivity of SN point contacts. *Physica B: Condensed Matter*, 218(1-4):122–125, 1996.

[20] Tian Le, Lichang Yin, Zili Feng, Qi Huang, Liqiang Che, Jie Li, Youguo Shi, and Xin Lu. Single full gap with mixed type-I and type-II superconductivity on surface of the type-II dirac semimetal $PdTe_2$ by point-contact spectroscopy. *Physical Review B*, 99(18):180504, 2019.

[21] CC Yang, FC Tsao, SY Wu, W-H Li, and KC Lee. Enhanced critical magnetic field in superconducting Pb nanoparticles. *Journal of Low Temperature Physics*, 131(3):349–352, 2003.

[22] Mingquan He, Chi Ho Wong, Pok Lam Tse, Yuan Zheng, Haijing Zhang, Frank LY Lam, Ping Sheng, Xijun Hu, and Rolf Lortz. "giant" enhancement of the upper critical field and fluctuations above the bulk T_C in superconducting ultrathin Lead nanowire arrays. *ACS nano*, 7(5):4187–4193, 2013.

[23] José Gabriel Rodrigo, V Crespo, H Suderow, S Vieira, and F Guinea. Topological superconducting state of Lead nanowires in an external magnetic field. *Physical Review Letters*, 109(23):237003, 2012.

[24] Anshu Sirohi, Preetha Saha, Sirshendu Gayen, Avtar Singh, and Goutam Sheet. Transport spectroscopy on trapped superconducting nano-islands of Pb: signature of unconventional pairing. *Nanotechnology*, 27(28):285701, 2016.

[25] Benjamin Post and Frank W Glaser. Crystal structure of ZrB_{12}. *JOM*, 4(6):631–632, 1952.

[26] Colin HL Kennard and Lindsay Davis. Zirconium dodecarborides ZrB_{12}. confirmation of the B_{12} cubooctahedral unit. *Journal of Solid State Chemistry*, 47(1):103–106, 1983.

[27] A Leithe-Jasper, A Sato, and T Tanaka. Refinement of the crystal structure of Zirconium dodecaboride, ZrB_{12}, at 140 K and 293 K. *Zeitschrift für Kristallographie-New Crystal Structures*, 217(1):319–320, 2002.

Chapter 7

Conclusion

I have investigated the superconducting properties of four materials; AuBe, RuB_2, Ru_7B_3, and ZrB_{12}. In summary, in all these material systems, it was found that the superconducting energy gap could not be understood within the conventional single-band isotropic BCS framework. In my analysis, I pointed out the deviations, and I also tried to explain those deviations using further modifications in the models, wherever necessary. This thesis is the summary of my investigations.

Depending on the experimental tools used, the thesis can be broadly divided into two parts. The first part involves tunnelling spectroscopic measurements on the first three materials mentioned above down to ultra-low temperature (ULT) that were performed under an ultra-high vacuum (UHV) scanning tunnelling microscope (STM). In AuBe and RuB_2, we found that two *s*-wave gaps are necessary to describe the quasiparticle excitation spectra at ULT. For AuBe, a simple two-gap model [1] incorporating interband tunnelling of quasiparticles seems sufficient [2]. On the other hand, RuB_2 warrants a more advanced model [3] with additional factors like interband scattering. Our study also reveals an unusual magnetic field dependence of the spectral features in RuB_2 [4]. In Ru_7B_3, which is a non-centrosymmetric superconducting phase, unlike RuB_2, we found that a small '*p*-wave' component is necessary with the otherwise dominant '*s*-wave' one in the description of the superconducting order parameter [5]. Our observation of mixed symmetry in Ru_7B_3 was recently verified based on the temperature dependence of

vortex lattice by another group [6].

The second part of my thesis is based on directional point-contact Andreev reflection spectroscopy (PCARS) and field-angle dependent ac magnetic susceptibility measurements on superconducting ZrB_{12} [7]. Based on directional PCARS, it was found that the superconducting gap and its local critical field are anisotropic in this material. Further, two-coils mutual inductance measurements revealed that ZrB_{12} behaves like a type-I as well as a type-II superconductor depending on the direction of the applied magnetic field. This was further supported by the detailed analysis of magnetic field dependent spectra which indicated the presence of vortex cores along the (001) direction but not in the perpendicular direction. These observations match remarkably well with the theoretical expectations [8] for an anisotropic superconductor near critical Bogomolny-point, which was proposed recently. Also, our results project ZrB_{12} as a model anisotropic superconductor where the physics of inter-type superconductivity can be further explored experimentally.

Bibliography

[1] H Suhl, BT Matthias, and LR Walker. Bardeen-Cooper-Schrieffer theory of superconductivity in the case of overlapping bands. *Physical Review Letters*, 3(12):552, 1959.

[2] Soumya Datta, Aastha Vasdev, Partha Sarathi Rana, Kapil Motla, Anshu Kataria, Ravi Prakash Singh, Tanmoy Das, and Goutam Sheet. Spectroscopic evidence of multigap superconductivity in noncentrosymmetric AuBe. *Physical Review B*, 105(10):104505, 2022.

[3] Yves Noat, Tristan Cren, François Debontridder, Dimitri Roditchev, W Sacks, Pierre Toulemonde, and Alfonso San Miguel. Signatures of multigap superconductivity in tunneling spectroscopy. *Physical Review B*, 82(1):014531, 2010.

[4] Soumya Datta, Aastha Vasdev, Soumyadip Halder, Jaskaran Singh, Yogesh Singh, and Goutam Sheet. Spectroscopic signature of two superconducting gaps and their unusual field dependence in RuB_2. *Journal of Physics: Condensed Matter*, 32(31):315701, 2020.

[5] Soumya Datta, Aastha Vasdev, Ranjani Ramachandran, Soumyadip Halder, Kapil Motla, Anshu Kataria, Rajeswari Roy Chowdhury, Ravi Prakash Singh, and Goutam Sheet. Spectroscopic evidence of mixed angular momentum symmetry in non-centrosymmetric Ru_7B_3. *Scientific Reports*, 11(1):21030, 2021.

[6] AS Cameron, YS Yerin, YV Tymoshenko, PY Portnichenko, AS Sukhanov, M Ciomaga Hatnean, D McK Paul, G Balakrishnan, R Cubitt, A Heinemann, et al. Singlet-triplet mixing in the order parameter of the noncentrosymmetric superconductor Ru_7B_3. *Physical Review B*, 105(9):094519, 2022.

[7] Soumya Datta, Sandeep Howlader, Ravi Prakash Singh, Goutam Sheet, et al. Anisotropic superconductivity in ZrB_{12} near the critical Bogomolnyi point. *Physical Review B*, 105(9):094504, 2022.

[8] Tiago T Saraiva, Alexei Vagov, Vollrath Martin Axt, J Albino Aguiar, and AA Shanenko. Anisotropic superconductors between types I and II. *Physical Review B*, 99(2):024515, 2019.